UCGE Reports

Number 20279

Department of Geomatics Engineering

Human Lower Limb Kinematics Using GPS/INS
(URL: http://www.geomatics.ucalgary.ca/links/GradTheses.html)

by

Sidney Pascal Kwakkel

December 2008

SCHULICH
School of Engineering   UNIVERSITY OF CALGARY

UNIVERSITY OF CALGARY

Human Lower Limb Kinematics Using GPS/INS

by

Sidney Pascal Kwakkel

A THESIS

SUBMITTED TO THE FACULTY OF GRADUATE STUDIES

IN PARTIAL FULFILLMENT OF THE REQUIREMENTS FOR THE

DEGREE OF MASTER OF SCIENCE

DEPARTMENT OF GEOMATICS ENGINEERING

CALGARY, ALBERTA

January, 2009

UNIVERSITY OF CALGARY

FACULTY OF GRADUATE STUDIES

The undersigned certify that they have read, and recommend to the Faculty of Graduate Studies for acceptance, a thesis entitled "Human Lower Limb Kinematics Using GPS/INS" submitted by Sidney Pascal Kwakkel in partial fulfilment of the requirements for the degree of Master of Science.

Abstract

The use of inertial-based sensors has seen an incredible growth in human motion analysis and pedestrian navigation in the past few years. The allure of kinematic measurements outside of the laboratory and position information during satellite outages have fueled an explosion of research aimed at improving the measurement quality and decreasing the cost and size of these inertial devices. Of late, micro-electro-mechanical systems (MEMS) based inertial devices have become popular because they cost a fraction and weigh much less than their expensive, bulky, non-MEMS counterparts.

The Crista inertial measurement unit (IMU) from CloudCap Technologies integrates MEMS accelerometers and gyroscopes to give acceleration and rotation rate data that can be transformed into position, velocity and attitude information. The concern, however, is the long-term accuracy of these measurements. Sensor errors accumulate rapidly in MEMS inertial units, and much work has been done to mitigate and control these errors. Of late, GPS/INS Kalman filters have been used with great success. Not only is the short-term accuracy of the MEMS devices exploited in satellite outages, but the long term stability of satellite-based position information is a natural complement to the error-prone inertial devices.

Recently, exploitation of repeatable gait dynamics has improved the performance of GPS/INS pedestrian navigation results by applying zero velocity updates (ZUPTs) during the stance phase of the walking cycle. By controlling the velocity errors, it has been shown that the attitude information measured by GPS/INS is much improved. These two quantities, velocity and attitude, are crucial to the measurement of kinematic metrics such as knee and ankle rotations, as well as foot position and trajectory.

The accuracy of the GPS/INS system is assessed for its use in human lower limb kinematics, though the systematic development of step detection, ZUPT application and

comparison with traditional motion capture modalities. The system is validated by excellent results in position and rotational accuracy. Rotation angles measured for walking and running gaits using the proposed inertial methodology were 1-2° different than what was measured using traditional optoelectric technology, while positional differences were approximately 1 cm (3D RMS). The estimation of step length using integrated velocities shows approximately 1% difference from the optoelectric values. For the walker and runner observed in this case, the step length was observed with 4 mm and 9 mm error (3D RMS), respectively.

Finally, the versatility of the inertial measurement methodology is shown. In one of the most trying arenas of sport, the marathon, kinematic and navigational measurements are extracted and compared. The effects of running over 42 km are shown, as step length, step frequency and joint flexion are noticeably decreased.

Acknowledgements

It is my pleasure to extend with my most heartfelt thanks acknowledgement to Drs. Gérard Lachapelle and Elizabeth Cannon for their tutelage, direction and support, without whose guidance this research would not be possible. Also a sincerely thanks to Drs. Cillian O' Driscoll and Mark Petovello who shared with me their immense knowledge of their subject matter and made this experience as rich as it has been.

The assistance of Dr. Gerald Cole, Adjunct Professor in the Faculty Kinesiology, Professor Janet Ronsky, CRC Chair in Biomedical Engineering in the Schulich School of Engineering and Adjunct Professor in Kinesiology, and Mr. Stephen Andrews, doctoral candidate under Professor Ronsky's supervision, in arranging and assisting with the system validation in Chaper 6, is acknowledged.

Mr. Aiden Morrison, PhD candidate in the PLAN Group, is acknowledged for the design and assembly of the NavBox^{TM}. The GPS/INS software used in this thesis was initially written by Mr. Saurabh Godha, MSc candidate in the PLAN Group in 2004-06, and in collaboration with Mr. Jared Bancroft, PhD candidate in the PLAN Group, modified for pedestrian and kinematic applications.

I would be remiss without extending my most sincere thanks to my family; mom and pap; Claudia, Tom, Bodhi, Nyah and Ayers Cull. They are my motivation in most things that I do. This thesis is once again a product of the love and dedication that they've shown me throughout my years.

Finally, I send my heart out to my favourite person in the world, Nikki Kirkpatrick. She is the part of me that I treasure most in this world, and I honour her with this work.

Table of Contents

List of Tables

List of Figures

For Nikki

"In dreams and in love, there are no impossibilities"

Chapter 1

Introduction

Locomotion, or the act of moving from one place to another under one's own power, is a beautiful achievement that sets animals apart from the rest of the natural world. It involves starting, stopping, as well as changes in direction and speed, all while responding to varying environmental conditions. The different patterns of locomotion between species, namely crawling, walking, swimming, flying and running, are amazingly diverse. Within a species a basic pattern of locomotion exists, however individuals move with a unique peculiarity depending on their anatomy, muscle composition and fitness.

Understanding this basic pattern of human motion and the peculiarities between individuals has challenged minds throughout history. The study of human movement has evolved greatly from Classical treatments[1] through the Renaissance[2] into pre[3] and post-WWII[4] eras. A complete review is beyond the scope of this thesis, but is explored fully in Klette & Tee (2007). By understanding these commonalities between individual variations on this pattern can be evaluated to detect clinical pathology or inefficiencies.

Current state of the art technology for motion capture involves optoelectric measurements. This technology is hindered by expensive equipment set-up, a need for dedicated lab space and limited measurement volumes.

An emerging technology involving Inertial Navigation Systems (INS) is becoming

---

[1]Classical approaches include works from the *Edwin Smith Surgical Papyrus* from Ancient Egypt (Breasted translated to English 1930) or works by Hippocrates (translated to English 2007) or Aristotle (translated to English 2004) in Ancient Greece.

[2]da Vinci (translated to English 2005) being the most notable contributor to the field of human motion studies during the Renaissance. However, also notable are Galileo Galilei and Borelli (1680).

[3]Considered by many to be the Age of Enlightenment for human motion analysis. Major contributions were made by Weber et al (1836), Marey (1878), Muybridge (1955, 1957), Trendelenberg (1895), as well as Braüne & Fischer for their anatomical contributions and Morton for his work on forefoot dysfunction.

[4]Inman (1966), Inman et al (1981), Saunders et al (1953) for their work on post-war prosthetics, Ducroquet et al (1968)

increasingly popular for the study of motion capture (Kavanagh et al 2006). Inertial sensors overcome many of the limitations of optoelectric equipment. These sensors are low cost, lightweight and small. They can record measurements outside of the lab and large amounts of data can be collected. Locomotion can therefore be studied while a subject performs everyday activities in a non-laboratory setting.

The use of INS sensors is, however, limited by one troubling complication, namely measurement accuracy. Sensor errors are variable over time and can change from one use to another, a complication not shared by their bulky expensive optoelectric counterparts.

Limitations, however, are only challenges to overcome and great potential exists in developing algorithms that improve sensor performance. Either by characterizing the sensor errors on-the-fly or limiting the effects of these errors on the measurement, the opportunity to refine this technology so that it can lead in the area of motion capture is real.

The answer to this problem may involve the combined use of Global Navigation Satellite Systems (GNSS) and INS. This combination has become increasingly popular given certain complimentary characteristics. While the navigation capability of GNSS is stable over long periods of time, it can suffer from short-term outages due to satellite obfuscation and occlusion. Conversely, INS is reliable over short time periods, but lacks long-term stability due to the accumulation of sensor errors. By combining these two technologies, accuracy is better than if either technology is used in isolation. GNSS/INS allows for characterization of the error in the INS sensors while they are in use. By applying the just-in-time sensor errors to the sensor output, better measurements can be obtained.

The challenge now is to prove that the combination of GNSS/INS improves the measurement accuracy to a degree where inertial sensors can rival the current mode of motion capture.

1.1 Kinematics

There are many definitions of what kinematics is depending on the discipline or field of study. In one field, kinematics may refer to the linear dynamics (velocity and acceleration) of the subject, while in others the rotation rate and angular acceleration may be of interest. In order to avoid such ambiguity, it is important to define what the word *kinematics* will mean throughout the discussion in this document. For this purpose, kinematics is defined as,

> *"describing the motion of a segment of the human body without consideration of the circumstances that led to the movement."*

Characterizing a human's gait includes descriptions of knee flexion, ankle rotation, and the positions of the feet, knees and hips to name a few (see Figure 1.1). However, in the realm of kinematics there is no regard to the muscles that are involved in lifting the leg off of the ground, or the nervous systems that are used to make the movement happen. These are reserved for an entirely separate branch of biomechanics called *kinetics*, and will not be discussed here.

1.2 The Lower Limb

The human lower limb is a complex structure. There are 30 bones in the human leg, which comprises one quarter of all the bones in the body (Figure 1.2). Moreover, these bones move relative to each other and form 33 joints in combination with over 100 muscles and ligaments. To further complicate the anatomy, a network of vasculature, nerves and soft tissue are intertwined seamlessly into an amazingly efficient assembly (Netter 1997).

As a functional unit, the foot and ankle may be considered one of the most complex structures in the body. In providing support and propulsion, the various ligaments that form the joints in the foot and ankle have differing amounts of tension and thus vary
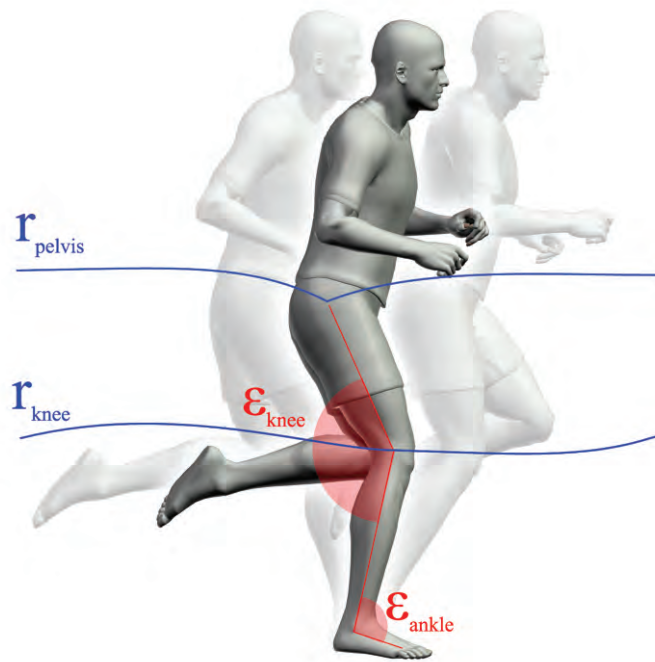
Figure 1.1: Rotations (red) and displacement (blue) are common kinematic metrics.

the amount of mobility each joint can provide. Due to this variable mobility, different models of the lower limb have been proposed which simplify the structural units of the limb. The exact model depends on the application in which the limb is to be used.

In this section, a brief description of the lower limb's anatomy is given, as well as some of the kinematic terminology that will be used in later sections. Before such a discussion can take place, a description of the models used to represent the human lower limb will be given in the context of the current research.

1.2.1 Models of the Lower Limb

The lower limb has been modelled many ways, ranging from a simplistic, single rigid body model to a full 3D model representing all of the features in the foot and ankle. While simpler models are useful for coarse movements, such as kicking a ball, they are insufficient for most kinematic applications. More sophisticated models that segment the limb into multiple rigid segments offer valuable insight into the kinematics between
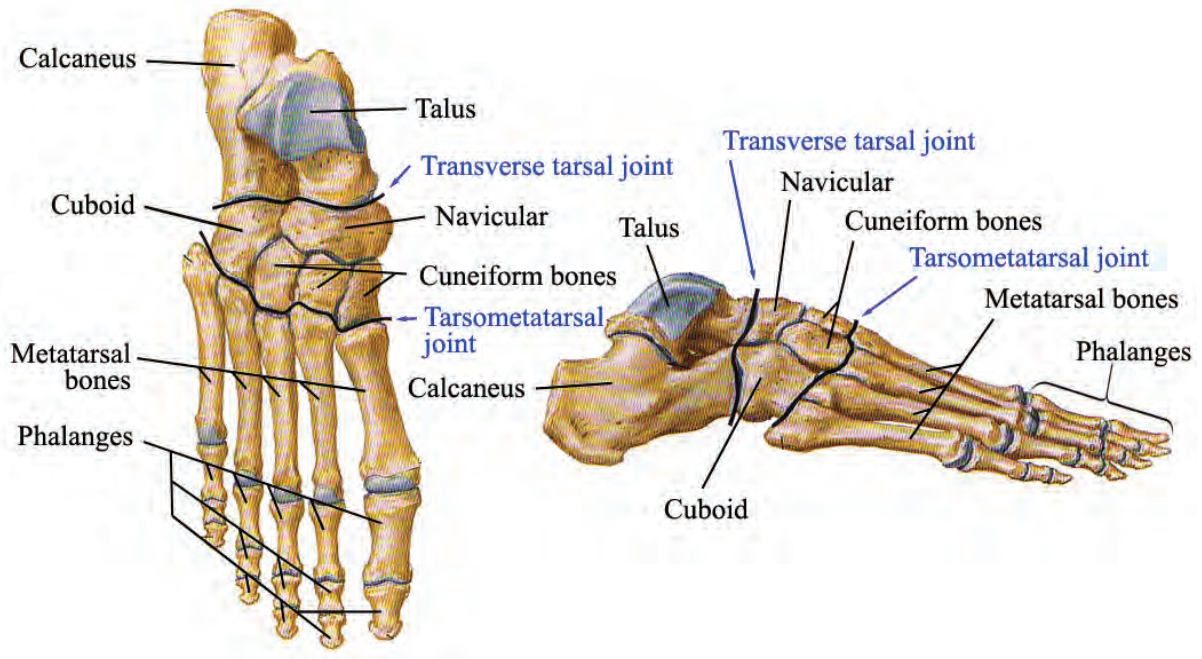
Figure 1.2: The bones of the foot with major joints labelled (blue): dorsal view (left) and lateral view (right). Modified from Netter (1997)

those segments. However, if every bone were represented the number of measurements required would be obtrusive, and such granularity is often not needed. A trade-off is needed: model the foot with sufficient granularity to offer meaningful kinematics, but restrict the number of measurements to allow for reproducible methodologies.

At its simplest, the foot can be modelled as a single rigid member from the knee to the toes (Figure 1.3a). In this case, the joints in the foot and ankle are fixed and the internal rotations within the lower limb are ignored. In effect, the limb appears much like many post WWII prosthetics, with no flexibility or manoeuvrability. In these cases, the limb is often restricted to a single plane of rotation (Kepple et al 1990, Siegel et al 1995). Such kinematic limitations are unable to track multi-axis joint rotations (Scott & Winter 1991, Bharatkumar et al 1994, Siegel et al 1995, Kidder et al 1996, Leardini et al 1999).

The two-segment model is a degree more complex than the single segment model in that it divides the lower limb into two rigid members, namely the shank and the foot (see

(a) One segment

(b) Two segments

(c) Three segments

(d) Four segments
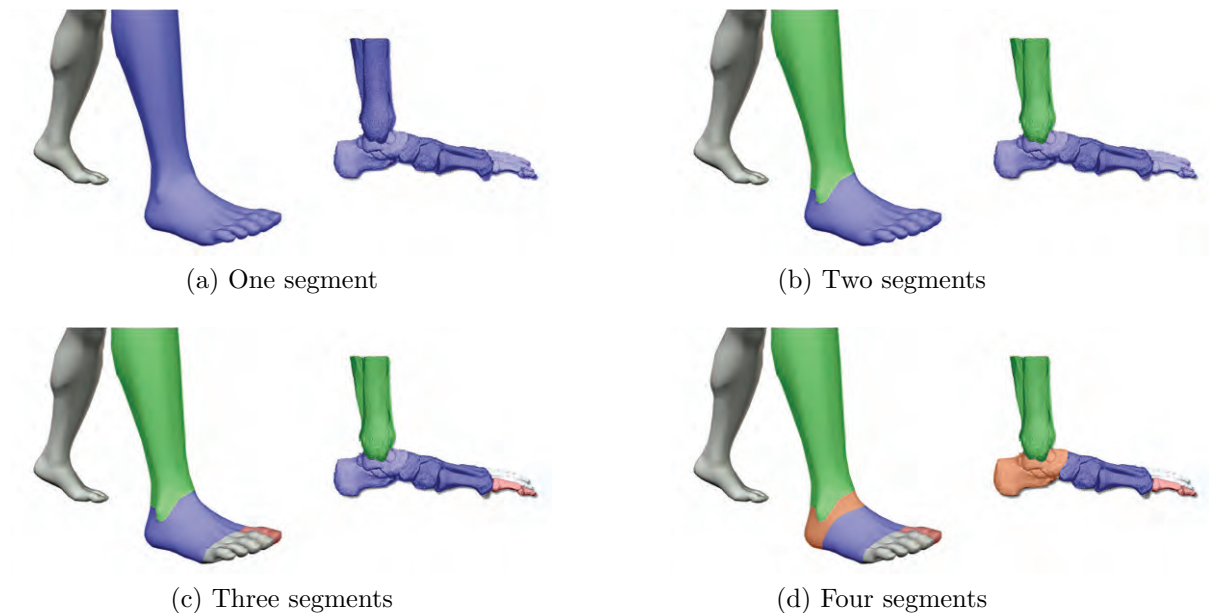
Figure 1.3: The foot and ankle are often simplified and represented as a series of rigid members. (a) a single segment from knee to toes. (b) the two-segment model separates the tibia and fibula from the foot. (c) the three-segment model segments the toes from the rest of the foot. (d) the four-segment model segments the rearfoot from the forefoot and the toes.

Figure 1.3b). The shank is an aggregation of the tibia and fibula and the foot represents all of the bones including the talus and all bones distal to it. When the two-segment model is used, a single degree of rotation between the segments allows for ankle flexion and extension to be observed, however rotations in the coronal and transverse planes are typically ignored (see Figure 1.4).

Although the single and two-segment models are very seldomly used in research arenas, they are commonly employed in video gaming worlds and animations because they are computationally simple and, in the case of the two-segment model, offer a reasonable organic representation that is aesthetically appealing.

Within the sphere of academic and clinical motion analysis, the three and four-segment models are most common (Carson et al 2001). In the three-segment model, the toes (and specifically the hallux) are considered a single rigid member apart from the

rest of the foot (see Figure 1.3c). With this model, it is easy to represent toe flexion, and since the joints between the phalanges and the metatarsals are highly mobile, the relative movement between these segments is often of interest.

The four-segment model is very similar to the three-segment model, however the foot is further segmented into a rearfoot and forefoot (see Figure 1.3d). Proposed initially by Kidder et al (1996), the four segments include the shank (tibia and fibula), rearfoot (calcaneus, talus and navicular), forefoot (cuboid, cuniforms and metatarsals) and hallux (first proximal and distal phalanges). This model is attractive in shoe studies that often measure torsion; the small but meaningful rotations in the coronal plane between the forefoot and the rearfoot.

Moving to the other end of the spectrum towards more complex and comprehensive models, Udupa et al (1998) has shown individual bone movements using magnetic resonance imaging (MRI). While this modality offers a wealth of information, it suffers from limited practicality since the subject must perform actions inside the bore of the imaging equipment. Despite this limitation, an important contribution of Udupa et al (1998) was to validate assumptions about joint mobility (or non-mobility) in other limb models.

1.2.2   Movements of the Lower Limb

The joints in the foot and ankle are able to rotate around various axes. In human kinematics, the terminology that describes these rotations can depend on the direction of the rotation as well as the plane in which it occurs. Figure 1.4 is a depiction of the various rotations that are possible and shows the various planes of rotation. For the remainder of this thesis, whenever possible, blue will denote rotations in the coronal plane, green will denote rotations in the saggital plane and orange will represent measurements in the transverse plane.

Rotations in the Sagittal Plane

Coronal Plane

Ankle (upper):	Eversion	Inversion
Ankle (lower):	Valgus	Varus
Toe:	Pronation	Supination

Sagittal Plane

| All: | Dorsiflexion | Plantarflexion |

Transverse Plane

| All: | Internal | External |
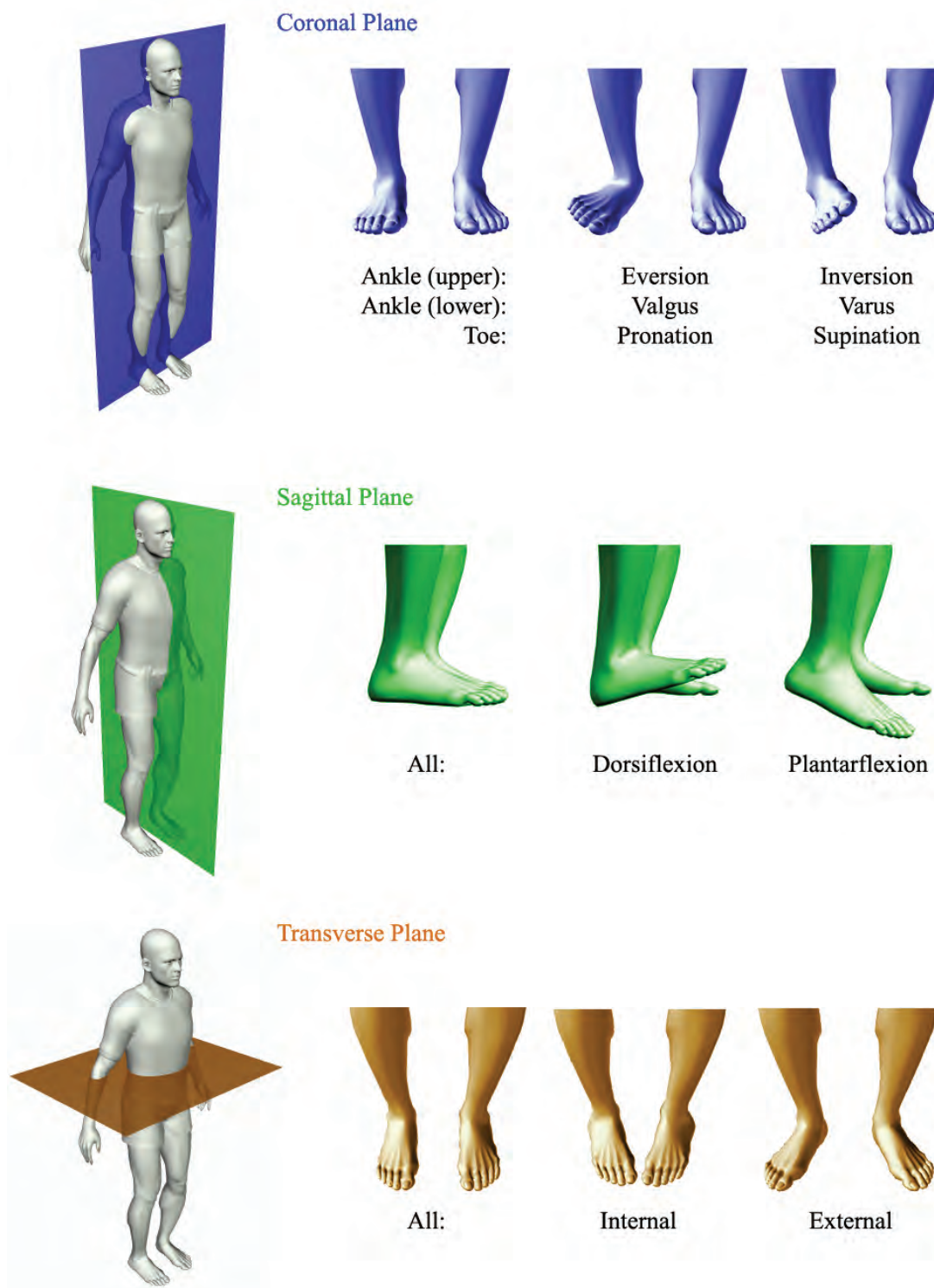
Figure 1.4: Rotations in the lower limb have specific terminology that depend on the direction of the rotation and the plane in which they occur. The rotations in each plane have been colour-coded in the figure above (blue) coronal plane; (green) sagittal plane; and (orange) transverse plane.

Rotations in the sagittal plane are commonly referred to as *pitch*. The classifications for rotations in the sagittal plane are simpler than those in the coronal plane in that there is no distinction between which segments the rotations occur. Instead, there are only two terms that describe all rotations in the sagittal plane:

- *Dorsiflexion* describes a rotation in the sagittal plane which results in the toe moving towards the knee. The counter rotation, *plantarflexion*, thus describes the toe moving away from the knee.

Rotations in the Transverse Plane

Rotations in the transverse plane are commonly referred to as *yaw*. Much like the sagittal plane, rotations in the transverse plane are simple in that two terms define all:

- *External* rotations occur in the transverse plane and describe the action of the toe moving away from the medial line, whereas the counter, *internal* rotations describe the toe moving towards the medial line.

Rotations in the Coronal Plane

Rotations in the coronal plane are commonly referred to as *roll* in the language of navigation. The exact term describing the rotation depends on the joint that is being observed:

- *Eversion* describes the rotation between the shank and the rearfoot (upper ankle) that causes the centre of balance to fall medially, or towards the body's centre line. The opposite rotation, or counter rotation, to eversion is called *inversion*.

- *Valgus* similarly describes a rotation between the rearfoot and the forefoot (lower ankle) that causes the centre of balance to fall medially. The counter rotation in this case is called *varus*.

- *Pronation* occurs when the medial rotation occurs between the forefoot and the hallux. Conversely, the counter rotation is called *supination*.

During walking or running, multiple rotations can take place at the same time. The foot can be inverted, pronated and dorsiflexed at some portions of the gait and everted, pronated and plantarflexed at others. The challenge, is to separate these rotations and measure them as distinct quantities.

Anatomical Description of Rotation

The planar rotations described above are commonly used in some literature. However, these are not the only jargon that is encountered in the literature. Another convention more commonly describes the rotation of a segment in relation to da Vinci's *Vitruvian Man* (da Vinci translated to English 2005). To give any work the broadest application possible rotations are often qualified as flexions, extensions, adductions and abductions. Whenever possible it is important to offer these measures to make the discussion accessible to all. While not all of the terms are relevant to this work, there are some that will be used during the course of discussion:

- *Flexion* refers to rotation in the joint in the direction of the flexor muscles and ligaments, whereas the counter, *extension*, refers to the rotation of the joint in the direction of the extendor muscle and ligaments.

In the case of the knee, the hamstring muscles are considered the flexor muscles

and the quadriceps are considered the extendor muscles. Hence, straightening the leg is referred to as extension and curling the leg is referred to as flexion.

- *Adduction* refers to the movement of one part of the body toward another or toward the median axis of the body, and the converse movement, *abduction* is the movement of one part of the body away from another or away from the median axis of the body

Qualifying rotations as extensions or flexions and adductions and abductions are common tongue by kinesiologists and sports physiologists. Therefore, it is important, whenever possible, to offer measures of these qualities to maximize their usefulness and extend the application of these measurement technologies to as wide an audience as possible.

Other Gait Related Terminology

While much of the terminology related to gait movements relates to the rotations involved, there are other movements that have been described in the literature:

- *Walk Ratio* refers to the ratio of *stride length* over *stride frequency.* This quantity has been shown to be consistent for individuals over a wide range of walking speeds (Nagasaki et al 1996).

- *Lateralization* pertains to differences between the right and left sides of the body during gait.

1.3   Limitations of Previous Research

1.3.1   Optical Approach to Human Kinematics

As mentioned in previous sections, human lower limb kinematics have traditionally been performed in laboratory spaces with elaborate camera setups (Kepple et al 1990, Kidder et al 1996, Carson et al 2001). While these studies provide excellent results for lower limb joint positions and rotations, their shortcomings are common amongst all optical human motion analysis; namely, the limited measurement volume, the cost of the equipment used, errors introduced by differentiating position and velocity data, and the inability to observe real-world factors that may affect the movements (Murray et al 1985, Nigg et al 1995).

The current generation of optical sensors (e.g. PEAK, Vicon, Qualisys, etc) offer rotational measurement accuracies of $\pm 1°$ (Carson et al 2001), and come with proprietary software processing tools that simplify the measurement overhead. However, with this convenience comes cost. Black box solutions are of limited use in academic settings where systems must be characterized by error analysis and algorithm implementation. By using an out-of-the-box solution, this characterization is forfeit and researchers are left to accept manufacturers' estimates of measurement errors, if any are given at all.

1.3.2   Inertial Pedestrian Navigation

In the arena of pedestrian navigation, satellite-based methodologies have become a popular discipline. The use of stand-alone inertial units to augment navigation solutions in times of satellite outage is a common topic, and many algorithms have been shown to improve the position and velocity solutions (Ladetto et al 2001, Stirling et al 2005, Godha et al 2006). The use of high-sensitivity GPS receivers as in the case of Mezentsev (2005) is also of interest. However, while the navigational component of these studies is considerable, their kinematic contribution is limited.

Recent studies have shown that there is significant information to be gathered through the combination of navigation and kinematic data (Kwakkel et al 2007, Kwakkel 2007, Kwakkel et al 2008). In fact, it has also been shown that integrating information from the two domains can be mutually beneficial (Bancroft et al 2008). Perhaps by learning more about gait dynamics, the relationship between pedestrian navigation and kinematics can further exploited.

1.3.3 Inertial Kinematics

In the past two decades, inertial sensors (specifically accelerometers) have been used to measure a variety of kinematic information (see Table 1.1). The introduction of several classes of lightweight accelerometers (e.g. strain gauge, piezoelectric, piezoresistive and capacitive) has made it possible to use these sensors for human motion analysis. Moreover, the trend toward combined accelerometer-gyroscope inertial sensors is opening new avenues of study. Table 1.1 provides an overview of the studies that have been completed using accelerometers and/or gyroscopes.

While many methodologies have been proposed to measure various kinematic metrics using inertial devices, few have published results that verify the accuracy of the inertial measurements. Instead, most studies validate the inertial measurements through repeatability. While this gives a sense of the overall robustness and precision of the system, its actual accuracies remain unknown. Mayagoitia et al (2002) and Pfau et al (2005) have conducted experiments that have compared to the traditional optoelectrical results against inertial measurements and found high degrees of correlation between the data sets. In the latter case, the study was conducted on horses and provided only correlative values of positional data.

There have been some studies that have sought to address gait mechanics with the use of inertial and satellite-based technologies (Terrier et al 2000, Ladetto 2000). Some have used differential GPS measurements to determine step lengths, stride frequency and trunk

Table 1.1: Examples of gait investigations using accelerometry

Focus of study	Measurements	Study
Upper body motion	3D hip and shoulder accelerations	Breniere & Dietrich (1992)
Physical strain during prosthetic gait	2D upper trunk, 1D thigh	Bussmann et al (2004)
Body segment inclination	3D lower trunk, angular velocity	Giansanti (2006)
	2D trunk and thigh	Lyons et al (2005)
Heel contact and toe-off events	3D foot and shank	Jasiewicz et al (2006)
	2D shank	Selles et al (2005)
	2D lower trunk	Mansfield & Lyons (2003)
Postural control and stability	3D upper body and shank	Kavanagh et al (2006)
	3D upper body	Menz et al (2003)
	3D lower trunk	Moe-Nilssen (1998)
Posture and limb movement	3D upper trunk, 1D thigh and shank	Prill & Fahrenberg (2006)
Ambulatory dyskinesia	3D shoulder	Manson et al (2000)
Segmental motion	2D upper and lower body	Petrofsky et al (2005)
Walking patterns	3D lower trunk	Sekine et al (2000)
Mobility monitor, segmental motion	3D upper and lower body, ang. vel.	Simcox et al (2005)
Mobility monitor, segmental motion, gait velocity	3D upper and lower body, ang. vel.	Tanaka et al (2004)
Swing and stance phase detection	1D shank	Willemsen & Bloemhof (1990)
Gait velocity	1D lower trunk	Perrin et al (2000), Schutz et al (2002)
	2D foot	Stirling et al (2005)
	2D foot	Fyfe (1999)
Gait velocity, trunk lift	3D lower trunk	Terrier et al (2000)
Gait velocity, stride, step length	3D foot	Godha et al (2006)
	3D lower trunk	Zijlstra (2004)
	3D foot	Morris & Paradiso (2002)
Knee flexion	1D thigh and shank	Willemsen et al (1990)
	1D thigh and shank, ang. vel.	Mayagoitia et al (2002)
Knee, ankle angle	3D shank, rearfoot, forefoot	Kwakkel et al (2007), Kwakkel (2007), Kwakkel et al (2008)

lift. Not until recently, however, were satellite-based and inertial devices combined to explore joint kinematics, such as knee and ankle rotations (Kwakkel et al 2007, Kwakkel 2007, Kwakkel et al 2008). While these studies have elucidated the methodology that is used for satellite-based, inertial kinematics, there remains a need to quantify the precision and accuracy of such measurements.

1.4   Low-cost Inertial Sensors

For inertial sensors to become a viable alternative to the current state-of-the-art in motion capture, the sensors must be low-cost, highly precise and not affect the movements which they are intended to measure. These and similar requirements in other industries have driven the development of Micro-ElectroMechanical Systems (MEMS) based inertial devices. MEMS-based sensors combine the benefits of high-volume manufacturing techniques with flexible and rugged packaging options resulting in small, robust inertial sensors that have increased the breadth of their applicability.

MEMS-based inertial units are currently the lowest cost inertial sensors in the marketplace. While their larger counterparts cost on the order of tens-of-thousands of dollars, MEMS units often only cost tens of dollars, making them vastly more attractive for innovative technologies.

The MEMS IMU used in this study is the Crista IMU from Cloud Cap Technologies Inc. This unit is considered automotive grade since it (or sensors with similar specifications) are used widely in the automotive industry. However, the Crista is more generally referred to as a MEMS IMU since is incorporates MEMS accelerometers and gyroscopes.

In this section, a brief discussion is given of the performance characteristics of MEMS-based inertial sensors. Particular attention is given to aspects of the sensors that affect their use in the pursuit of motion capture when compared to more expensive inertial units.

1.4.1 MEMS Inertial Sensors

The basic mechanism underlying acceleration measurement is often described in terms of a mass-spring system, which operates according to the principles of Hooke's law ($F = kx$), and Newton's 2nd law of motion ($F = ma$), where F is the experienced force, x represents a displacement, k is a constant defining the physical characteristic of the spring, m represents mass, and a denotes the acceleration of the mass. When a mass-spring system is submitted to compression or stretching force due to movement, the spring exerts a restoring force proportional to the amount of compression or stretch. Given that the stiffness of the spring can be controlled, the resultant acceleration of the mass element can be determined as follows:

$$a = \frac{kx}{m}.$$ (1.1)

In practice, acceleration is quantified using a number of techniques depending on the class of the accelerometer. For example, in a capacitive accelerometer, a silicon mass element is surrounded by an array of paired capacitors on opposite sides of the accelerometer housing. As the mass is displaced an imbalance between the opposing capacitors is created, and an output voltage is created proportional to the applied acceleration.

Regardless of the accelerometer class, the relationship between the electrical output and the applied acceleration must be determined by calibration under specific conditions. In high-end (expensive) sensors, these relationships are very stable and can thus be established through a calibration process and used for subsequent measurements. However, low-cost MEMS sensors suffer from variable error characteristics that can change even while the accelerometer is being used (El-Sheimy 2007). This last point is often neglected. Of the studies listed in Table 1.1, only Godha et al (2006), Kwakkel et al (2007), Kwakkel (2007), Kwakkel et al (2008) account for these changes. In most cases, errors are characterized through an initial calibration but neglect fluctuations while the sensor

is in use.

1.4.2   Performance of MEMS Inertial Sensors

Since the quality of an IMU is often determined by the quality of the gyroscopes (El-Sheimy 2007), the Crista IMU is known to perform less well than inertial units that incorporate high-quality, ring-laser gyroscopes such as the CIMU and the HG1700 (see Table 1.2). In particular, the turn-on bias of the Crista (5400 °/h) is considerable when compared to the other two IMUs. Moreover, the bias drift of the Crista IMU (1000 °/h) is many orders of magnitude higher than that of the high-end IMUs. The turn-on bias and scale factor were derived by calibration or taken from manufacturer's documentation and can vary markedly between individual units and change often during use. As such, actions need to be taken to ensure that the sensor errors are characterized appropriately for each use.

Table 1.2: Technical specifications of different IMU grades (Cloud Cap Technology Inc. 2007)

IMU	CIMU	HG1700	Crista
Grade	Navigation	Tactical	Automotive
Accelerometers			
In-run bias $[mg]$	0.025	1	2.5
Turn-on bias $[mg]$	-	-	30
Scale factor $[ppm]$	100	300	10000
Velocity random walk $[g/\sqrt{Hz}]$	-	2.16e-6	370e-6
Gyroscopes			
In-run bias $[°/h]$	0.0022	1	≤ 1040
Turn-on bias $[°/h]$	-	-	5400
Scale factor $[ppm]$	5	150	10000
Angle random walk $[°/h/\sqrt{Hz}]$	6.92	7.5	226.8

- denotes negligible value

1.5 Objectives

Before a discussion of the methodologies and techniques, it is important to define the goals of the research and explicitly state the objectives. In proposing a new inertial protocol for human motion analysis the following objectives need to be addressed:

1. *Quantify the precision and accuracy of the proposed inertial motion analysis methodology*: as the use of camera-based measurements is the current gold standard for human motion analysis, they will be compared side-by-side with the proposed inertial measurements in order to quantify the precision and accuracy of the new technology.

2. *Use gait dynamics in aiding INS error estimation*: using the highly repeatable characteristics of human gait to aid in the measurement accuracy both for navigation and kinematic analysis.

3. *Combining navigation and kinematic measures*: to demonstrate the inherent advantage over traditional kinematics of the combination of navigation and kinematic solutions that are aligned in time.

4. *Overcome the mathematical complexity of navigation and kinematics*: deriving a navigation solution and gait kinematics from satellite and inertial systems is a complex procedure involving hundreds of mathematical operations. Computations must be automated in order to provide timely and accurate solutions.

5. *Field tests and scenario testing*: An inherent advantage to the proposed methodology is its portability to various scenarios and conditions. The measurement of human gait is performed during walking and running, as well as other extra-laboratory settings. The intent here is to show the versatility and robustness (and limitations) of the proposed system.

1.6   Research Methodology

The following methodology was adopted in this thesis to achieve the objectives discussed in the previous section:

1. *Side-by-side comparison of the traditional optical and the proposed inertial methodologies*: In order to compare the proposed technology to the traditional system of kinematic analysis, a subject will be measured using both systems simultaneously. The results of each will be compared and analyzed for similarities and differences.

2. *Using stance phase dynamics to establish sensor errors*: The use of zero-velocity updates (ZUPTs) in inertial navigation has been shown to dramatically improve the navigation solution of low-cost inertial sensors by improving the estimation of sensor errors. As such, applying ZUPTs during the stance phase of the gait cycle should improve the overall accuracy of the kinematic measurements.

3. *Controlling for velocity and terrain*: In a given trajectory, over a length of time, a pedestrian will walk over various terrain and move faster or slower depending on the conditions in which they find themselves. Combining the navigation solution (i.e. the pedestrian's position, velocity and trajectory) with the gait kinematics measures will allow for the control various parameters in the analysis of gait over time.

4. *Software Development*: The proposed navigation and kinematic methodology is a mathematical transformation of GPS and INS measurements into established human locomotion parameters. As such, computer software was developed to perform the mathematical operations to quantify the results herein.

5. *Comparison to established modalities*: In order to establish the system accuracy of any new motion capture technology, the accuracy of the system must be estab-

lished. In this thesis, this was accomplished by comparing the inertial measure-ments against traditional optoelectrical measurements.

1.7   Outline

Chapter 2 provides an overview of relevant coordinate systems, GPS, INS and photogram-metry. The various errors associated with each technology are briefly discussed as they pertain to the research being conducted.

Chapter 3 provides an overview of estimation methods, discusses the estimation method known as Kalman filtering and provides a brief overview of blunder detection as it pertains to this study.

Chapter 4 outlines different GPS/INS integration strategies, and the implementation of those strategies in a Kalman filter, focusing on the structure of the mathematics that are important in such implementations. An algorithm for estimating INS errors is presented, emphasizing its implementation in the Kalman filtering algorithm.

Chapter 5 demonstrates how the outputs of a tightly coupled GPS/INS system can be used to separate steps and detect the different phases of the gait cycle. The rotational and positional kinematics are shown and correlated to navigational information, allowing for an analysis of gait metrics on flat ground, downhill and uphill terrains. This section also highlights the differences of the algorithms in walking verses running gaits, allowing for a thorough examination of both modes of pedestrian locomotion.

Chapter 6 compares the inertial algorithm to traditional optoelectric measurements. A side-by-side experiment was conducted using inertial sensors and optical markers. The correlation between these two sets of data demonstrates the accuracy and precision of the proposed kinematic algorithm.

Chapter 7 highlights the potential versatility of the inertial kinematic approach in providing an analysis of a runner's gait throughout the course of marathon. Metrics such

as joint rotations and step kinematics are analyzed to demonstrate the effects of fatigue on the runner. This section provides an analysis of human motions characteristics that were not previously obtainable with traditional motion analysis modalities.

Chapter 8 summarizes the major findings of the thesis and offers possible avenues for further research that will establish inertial measurements as a plausible alternative for human motion analysis.

Chapter 2

Measurement Systems Overview - GPS, INS and Photogrammetry

This chapter gives an overview of the GPS, INS and photogrammetric systems as they pertain to this study. A discussion of GPS is provided first, with particular attention paid to the error sources that are inherent to the system. Later, inertial systems are discussed with a focus given to the mechanization equations, inertial sensor errors and alignment procedures. Finally, a treatment of the processes involved in ascertaining rotation angles using a photogrammetric algorithm is presented. Specific detail are given regarding the propagation of measurement errors that are relevant to this study.

2.1   Coordinate Frames and Transformations

When describing locations of points on or near the Earth's surface, it is natural to turn to coordinate systems. For navigation, a fixed coordinate system enables the extension of positional information into calculations of distances, areas, volumes and direction. On the other hand, relational coordinate systems are often used to describe movements of objects relative to one another. There are several coordinate systems from which to chose. Each has its own unique utility depending on the particular application.

In this thesis, there are two applications of coordinate frames. The first, *navigation*, focuses on the science of measurement, determination, and mapping of points along the Earth's surface. Each point is referenced to the same coordinate system, and thus it is possible to observe trajectories, which include other information such as velocity, acceleration and attitude. The second application of coordinate frames involves *relative*

motion. In human motion capture, or kinematics, the relative movements of the segments of the body are of interest. While these movements could be described in a fixed system of coordinates, it is the relative relationship that is important. In this case, the reference coordinate system can be constantly moving, and therefore at any given time the coordinate frame can be in any arbitrary position.

2.1.1 Inertial Frame (i-frame)

The most fundamental coordinate system in navigation is the *inertial frame*, defined classically as the system in which Isaac Newton's laws of motion hold. Empirically, an inertial frame is non-rotating and non-accelerating with respect to an assembly of celestial references. In such system, a body at rest (or, in uniform rectilinear motion) will remain at rest (respectively, in uniform rectilinear motion) in the absence of applied forces. This is Newton's *First Law of Motion.*

In the context of Earth, an inertial frame is at best an abstraction, since any frame in the vicinity of the solar system is permeated by a gravitational field that possesses spatially varying gradients. For example, for a frame attached to the centre of the solar system and assumed to be non-rotating, a body at rest or in uniform rectilinear motion will accelerate under the gravitational influence of the sun and planets, (thus violating Newton's First Law); and thus the frame is not inertial. With this in mind, any formulation of an inertial frame, within the confines of our solar system, is inherently flawed.

For the purposes of this study, an inertial system can be defined as follows:

Origin   : Earth's centre of mass,

$Z^i - axis$: Parallel to the mean spin axis of the Earth,

$X^i - axis$: Points to the mean vernal equinox, and

$Y^i - axis$: Orthogonal to the X and Z axes to form a right-handed system.

In defining the i-frame in this way, there is a departure from standardized inertial frames such as the International Celestial Reference System (ICRS) which defines its origin at the centre of the solar system, and its Z and X axes on the North Celestial Pole and on the celestial equator, respectively. This departure is a means to simplify calculations with the understanding that the inherent errors incurred by defining the inertial frame in this way are negligible when compared to the other errors that will be discussed later in this thesis. This departure is noted here and will not be discussed further.

2.1.2 Earth Centred Earth Fixed Frame (ECEF or e-frame)

Here, a frame that is fixed to the Earth is discussed. Its origin coincides with the Earth's centre of mass, as it does in the i-frame. The difference is in the definition of the coordinate axes. In the case of the e-frame, the axes are allowed to move along with the rotation of the Earth. The coordinate axes are defined as follows:

Origin   : Earth's centre of mass,

$Z^e - axis$: Parallel to the mean spin axis of the Earth,

$X^e - axis$: Points to the mean Greenwich meridian, and

$Y^e - axis$: Orthogonal to the X and Z axes to form a right-handed system.

Figure 2.1 shows the relationship between inertial and ECEF coordinates, as well as the geodetic coordinates with respect to a rotationally symmetric ellipsoid. It is assumed in this study that the e-frame and i-frame differ only with respect to a rotation about the z-axis; thus the effects of polar motion, and other processes such as precession and nutation are ignored. If ω_e is the Earth's rate of rotation about its spin axis, then $\omega_e t$ (where t denotes time) is the angle of rotation between the inertial and ECEF frames.
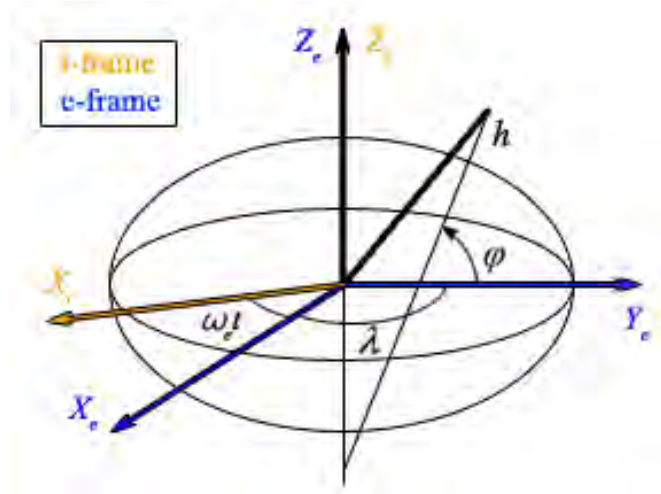
Figure 2.1: Inertial (i) and ECEF (e) Frames, with geodetic coordinates. Adapted from Jekeli (2001)

The transformation between the inertial and ECEF frames is thus given by a simple rotation as follows:

$$R_e^i = R_3(\omega_e t) = \begin{pmatrix} \cos\omega_e t & \sin\omega_e t & 0 \\ -\sin\omega_e t & \cos\omega_e t & 0 \\ 0 & 0 & 1 \end{pmatrix} \tag{2.1}$$

where,

R_i^e is the rotation matrix from the inertial to the ECEF frame,

R_3 is the rotation matrix about the third, or z, axis,

ω_e is the rotation rate of the Earth about its spin axis, and

t is time.

2.1.3 Local Level Frame (LLF or l-frame)

The local level frame is often used to navigate since users can refer to a compass to give them a sense of the North direction. Moreover, many maps are referenced to North and thus navigation is made easier if the users can orient themselves properly with respect
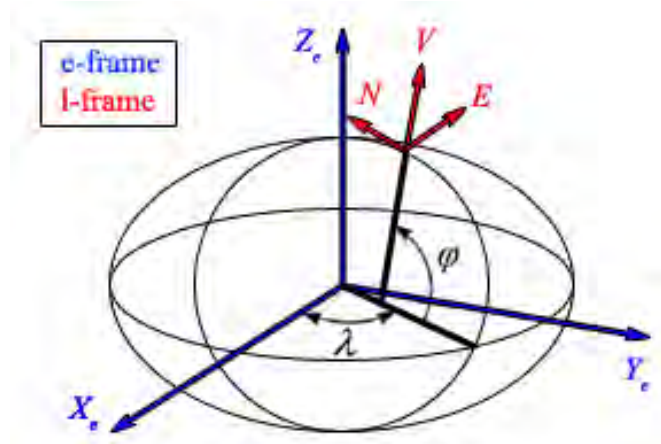
Figure 2.2: ECEF (e) and LLF (l) Frames. Adapted from Jekeli (2001)

to the map. Figure 2.2 shows the relation between the ECEF and LLF frames. The coordinate axes for the LLF frame are described as follows:

Origin   : Coincides with a local point (typically a sensor's centre)

V ($Z^l - axis$)   : Orthogonal to the reference ellipsoid pointing vertically,

N ($Y^l - axis$)   : Points to geodetic North, and

E ($X^l - axis$)   : Points to geodetic East.

The transformation between the ECEF frame and the local frame can be performed by consecutive rotations, as follows:

$$R_e^l = (R_l^e)^T = R_1(90° - \phi)R_3(\lambda + 90°) \tag{2.2}$$

where the superscript T is the transpose, and

R_e^l is the rotation matrix from the ECEF frame to the LLF frame,

R_1 is the rotation matrix about the first, or x, axis,

R_3 is the rotation matrix about the third, or z, axis,

ϕ is the latitude, and

λ is the longitude.

2.1.4   Body Frame (b-frame)

The body frame is an orthogonal coordinate frame. In this study, the axes of the body frame are made coincident with the axes of the inertial measurement unit (IMU). Figure 2.3 shows the body frame in relation to an IMU and an arbitrary LLF. The body frame is defined as follows:

Origin   : Coincides with the origin of the sensor triad

$X^b - axis$: Points to the right side of the sensor,

$Y^b - axis$: Points towards the front of the sensor, and

$Z^b - axis$: Orthogonal to the X and Y axes to form a right-handed frame.

The transformation from the body frame to the local frame can be performed as three consecutive rotations about the three orthogonal axes, as follows:

$$R_b^l = (R_l^b)^T = R_3(\psi)R_1(-\eta)R_2(-\xi) \tag{2.3}$$

where the superscript T is the transpose, and

R_b^l is the rotation matrix from the body frame to the LLF frame,

R_1 is the rotation matrix about the first, or x, axis,

R_2 is the rotation matrix about the second, or y, axis,

R_3 is the rotation matrix about the third, or z, axis,

ψ is the heading of the sensor,

η is the pitch of the sensor, and

ξ is the roll of the sensor.
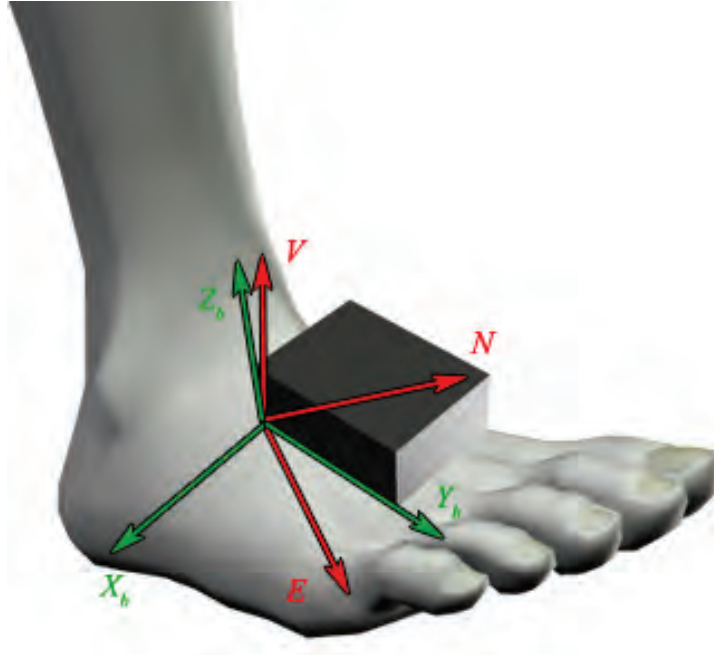
Figure 2.3: LLF frame (arbitrary North and East directions) and b-frame. The two frames' origins are coincident but are rotationally different.

For the purposes of inertial navigation, it is also important to be able to transform directly from the body frame into the ECEF frame. From equations 2.2 and 2.3, this transformation is possible and takes the following form:

$$R_b^e = R_l^e \cdot R_b^l \tag{2.4}$$

2.1.5 Joint Coordinate Frames

The coordinate frames discussed thus far have defined the INS navigation system. The descriptions of these frames and their relationship to each other is well defined and understood. However, they are not the only coordinate frames that exist. In fact, there are many frames that are more convenient depending on the application.
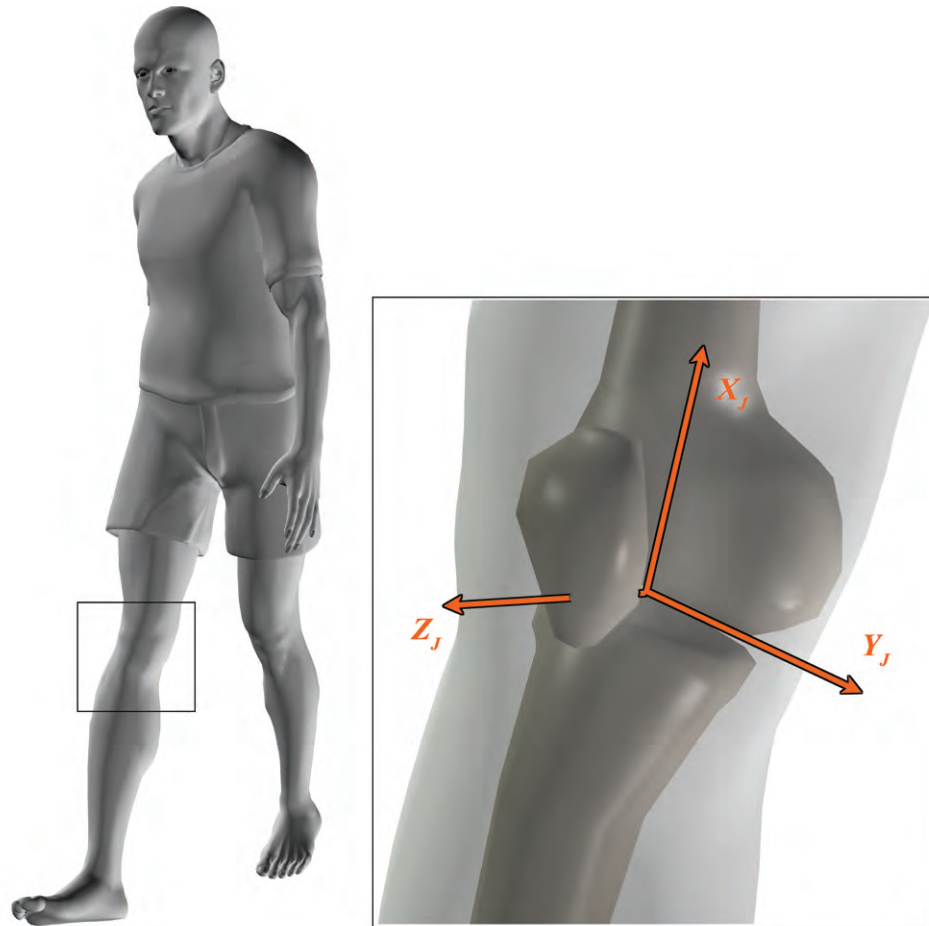
Figure 2.4: The joint coordinate frame is used to describe rotations and translations of the joint. Zoomed view of a knee joint coordinate frame (inset).

In Figure 2.4, a joint coordinate frame (JCF) is defined. The definition of this frame is as follows:

Origin : Coincides with the joint centre

$X^J - axis$: Points along the length of the proximal bone,

$Y^J - axis$: Points along the joint axis, and

$Z^J - axis$: Orthogonal to the X and Y axes to form a right-handed frame.

The JCF is a convenience that allows for a simple description of the rotations and translations that occur within a joint. For instance, rotation about the x-axis of the

JCF shown in Figure 2.4 represents flexion. Similarly, external and valgus rotations are described by rotations about the Y and Z-axes, respectively.

While the JCF is efficient for describing joint movements, it has an inherent flaw. The difficulty is defining the JCF in live subjects. Locating the joint centre and the joint rotation axis without invading the joint capsule is somewhat imprecise using external markers and therefore contributes error to the final measurements (Reinschmidt et al 1997). Improperly defining the JCF can lead to cross-talk between the rotations that are measured. Despite this shortcoming, the JCF is often used in kinematic experiments. In Chapter 6, the establishment of the JCF is described using optical markers.

2.2   Global Positioning System (GPS)

GPS is the product of a series of technological advances that took place in the latter half of the 20th century. The concept of positioning with GPS is based upon *trilateration*. In essence, trilateration is the estimation of position using three or more distances. This concept was not new at the time GPS was conceived. Given distances from three or more transmitters of known location, the observer could observe their position.

For this reason, in order for GPS to work properly, there are three requirements:

- *Positions of the satellites.* In order to carry out trilateration, the positions of the transmitters must be known very accurately. The more accurately these positions are known, the less error there is in the final position estimation.

- *Accurate timing.* In order to calculate the range between the satellite and the user using electromagnetic waves a precise timing system must be used. An error of only a millisecond in timing results in an inaccurate range of 300 km, so a sophisticated timing technique had to be developed. The GPS system had to be able to provide a time standard that was precise to a few nanoseconds in order to operate within the specifications.

- *Transferring time and position information.* The problem of keeping precise time and synchronizing clocks that are separated by considerable distances is an old one. In GPS, transferring the time of the highly precise satellite clock to the user's receiver that is equipped with a much less stable time-piece is very important for the acquisition of the range information.

These requirements are not easily solved, nor were they trivial problems for the designers of GPS. Fortunately, as GPS moved from planning to the implementation stages, orbit determination, atomic frequency standards, and the conceptualization of spread-spectrum signals made it possible to solve almost all of these issues.

The GPS system consists of three components: the space segment, the ground segment and the user segment (see Figure 2.5) (Misra & Enge 2004).

The space segment consists of a constellation of satellites that continuously broadcast signals. These satellites orbit the Earth in one of six orbital planes, and take one sidereal day (approximately 23 hours, 56 minutes) to complete one revolution. As of May 13, 2008 there are 32 GPS satellites orbiting the Earth (USCG 2008). Each satellite's position is transmitted to the user via the broadcast ephemeris as a set of orbital and clock parameters which are used to compute the satellites position at any given time (Kaplan & Hegarty 2006). The satellite orbits are monitored continuously from several stations around the Earth, and the orbital parameters are updated a maximum of three times per day via uploads made from the ground segment.

Recall that trilateration requires the measurement of ranges from transmitters of known position. In GPS, these transmitters are the satellite which are moving upwards of 4 km/s. The position of a satellite at any given instant however, can be estimated with an error of no worse than a few metres based on the predictions made 24-28 hours earlier.

The control segment is primarily concerned with monitoring the health and orbits of
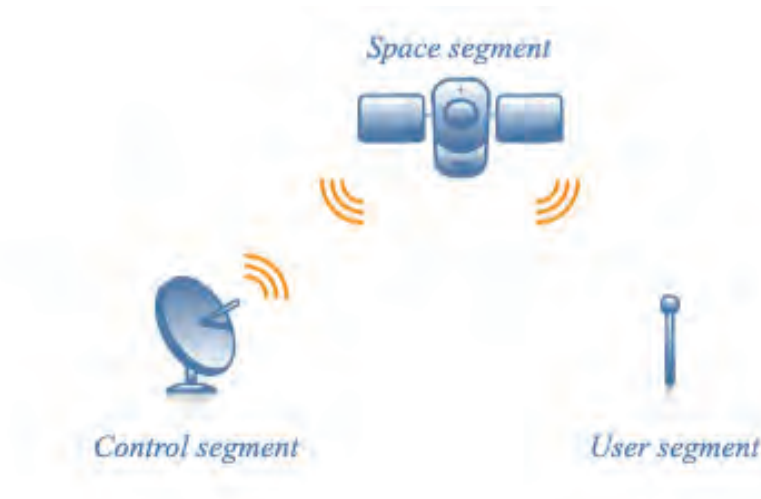
Figure 2.5: The three components of the GPS architecture: Control segment, space segment and user segment. Adapted from Misra & Enge (2004).

the satellites. Distributed across the globe, multiple stations are used to determine the accuracy of the broadcast ephemeris. The orbits of the satellites are predicted forward based on current orbit trajectories and as needed, the updated orbit and clock parameters are uploaded to the satellite in order to update the ephemeris information.

The user segment is the largest portion of the GPS architecture. Although the GPS was originally designed for civilian and military use, the civilian applications of GPS have resulted in a multi-billion dollar industry. Currently, the market for precision GNSS products is estimated at $3 billion, and is expected to grow to approximately $6-8 billion by 2012 (Lorimer & Gakstatter 2008). However, this estimate grows significantly when all end-user applications are included. For instance, it has been forecast that by 2013 GNSS end-user devices and systems will generate yearly revenues of $240 billion (ABI Research 2008).

GPS relies on Code Division Multiple Access (CDMA) to distinguish one satellite from another and transmit information from the satellite vehicle to the user. The signal is spread-spectrum and bi-phase modulated centred around two central frequencies: L1 (1575.42 MHz) and L2 (1227.60 MHz), with a third frequency, L5 (1176.45 MHz) being

implemented on upcoming block IIF satellites. The GPS signals are modulated by two Pseudo-random noise (PRN) codes: the Coarse-acquisition (C/A) code on L1 and the P code on L1 and L2, which is restricted to military usage by means of encryption. Currently, there are six block IIR-M satellites broadcasting an L2C code on L2, but this code is not expected to be fully implemented until 2011. In addition to these PRN codes, the satellites transmit a navigation message which contains the satellite's ephemeris as well as the constellation's almanac information.

For this study, single frequency (L1 only) measurements will be taken. As such, there are three different measurements that are currently available:

1. Code phase or *pseudorange* measurements,

2. *Carrier phase* measurements, and

3. *Doppler* or incremental phase measurements.

With the modernization of GPS and the addition of the L2C code on L2 and the new L5 frequency made available to civilians, there are sure to be many new measurements available, but they are not relevant to this study.

2.2.1 Pseudorange Measurements

In order to determine the range between the satellite and the antenna the propagation time of the electromagnetic signal is measured. This value, when scaled by the speed of light, gives an apparent distance from which to estimate the range. The term *pseudo*range is used because the propagation of the signal is disturbed by many factors that lead to inaccurate timing, and thus an inaccurate range. Equation 2.5 shows the contributing factors that comprise the pseudorange (Cannon & Lachapelle 2005).

$$p(t) = \rho(t) + c \cdot [dt(t) - dT(t)] + d_{orb}(t) + d_{ion}(t) + d_{trop}(t) + \eta_p \qquad (2.5)$$

where, (t) represents the value of the variable at time t, and

p is the measured pseudorange (m),

ρ is the geometric range between the satellite and the antenna (m),

c is the speed of light (m/s),

dt is the satellite clock error (s),

dT is the receiver clock error (s),

d_{orb} is the satellite position (or orbit) error (m),

d_{ion} is the ionospheric delay (m),

d_{trop} is the tropospheric delay (m), and

η_p is the error due to noise and multipath (m).

2.2.2   Doppler Measurements

The Doppler frequency represents the rate of change of the carrier phase observable (Kaplan & Hegarty 2006). The Doppler effect is caused by the relative movement of the satellite relative to the antenna or *vice versa*. Equation 2.6 represents the mathematical result of the Doppler effect.

$$f_{doppler} = \left(\frac{1 \pm \frac{v_{antenna}}{c}}{1 \pm \frac{v_{satellite}}{c}} \right) \cdot f_{satellite} \tag{2.6}$$

where,

$f_{doppler}$ is the measured Doppler frequency (Hz),

$f_{satellite}$ is the transmitted frequency ($f_{L1} = 1575.42$ MHz),

$v_{satellite}$ is the speed of the satellite in the direction of the antenna (m/s),

$v_{antenna}$ is the speed of the antenna in the direction of the satellite (m/s), and

$\pm$ depends on whether the antenna or satellite are moving closer together or farther apart.

The velocity of the satellite ($v_{satellite}$) can be accurately determined via the ephemeris, and the L1 frequency is known ($f_{satellite}$). Therefore, the velocity of the antenna ($v_{antenna}$) can be determined to a high level of accuracy if there are few distortions of the Doppler measurement.

Much like the pseudorange is affected by atmospheric effects, clock effects and noise, the Doppler measurement is also so affected. However, since the Doppler measurement is the rate of change of the carrier phase observable, it is only dependant on the time derivative of the quantities in equation 2.5. Equation 2.7 shows the contributing variables to the Doppler measurement (Cannon & Lachapelle 2005). Note the difference in sign for the ionospheric component (d_{ion}). This change in sign reflects the *code delay* and *carrier advance* characteristic of the ionosphere on GPS the signal (*ibid*).

$$\dot{\phi}(t) = \dot{\rho}(t) + c \cdot [\dot{dt}(t) - \dot{dT}(t)] + \dot{d}_{orb}(t) - \dot{d}_{ion}(t) + \dot{d}_{trop}(t) + \eta_{\dot{\Phi}} \qquad (2.7)$$

where, (t) represents the value of the variable at time t, and

$\dot{\phi}$ is the measured Doppler (m/s),

$\dot{\rho}$ is the geometric range rate between the satellite and the antenna (m/s),

c is the speed of light (m/s),

$\dot{dt}$ is the satellite clock error drift (s/s),

$\dot{dT}$ is the receiver clock error drift (s/s),

$\dot{d}_{orb}$ is the satellite position (or orbit) error drift (m/s),

$\dot{d}_{ion}$ is the change in ionospheric delay over time (m/s),

$\dot{d}_{trop}$ is the change in tropospheric delay over time (m/s), and

$\eta_{\dot{\Phi}}$ is the drift error due to noise and multipath (m/s).

Unlike the pseudorange equation, the effects of the clock drifts, and atmospheric effects are small since these errors typically do not change quickly with time. Since the

rate of change of any of the above quantities is small, the Doppler measurement results in a very accurate estimation of the antenna's velocity.

2.2.3   GPS Errors and Mitigation

GPS errors are commonly classified into one of two categories: common mode and non-common mode errors (Farrell & Barth 2001). The first type of errors, the common mode errors, are highly spatially correlated. More succinctly, the common mode errors experienced by one receiver are very similar to the errors experienced by a receiver in close proximity. Examples of common mode errors are satellite errors such as clock errors or orbit determination errors, as well as atmospheric effects. The latter classification, non-common mode errors, are those that show very little spatial correlation, and as such, are not common amongst receivers in close proximity to each other. Examples of non-common mode errors include receiver clock errors, multipath and noise.

Given this classification of GPS errors it is possible to reduce, and sometimes eliminate, common mode errors through a process called differential GPS or DGPS. The principle is to compute the measurement differences between the reference station and the rover antenna. By applying this difference in tandem with the previously known position of the reference station, the position of the rover can be computed very precisely. This concept of DGPS is depicted in Figure 2.6.

There exist three different types of differencing: namely, *single differencing*, *double differencing* and *triple differencing*. In the context of this study, only single and double differencing are employed. Triple differencing is mentioned here for completeness, but will not be discussed further. Of single and double differencing, each has their own advantages and disadvantages and are applicable in certain situations. These characteristics will be explained in the following paragraphs.

An important note about differencing is that it is only effective at reducing or eliminating common mode errors. Non-common mode errors such as multipath and noise,
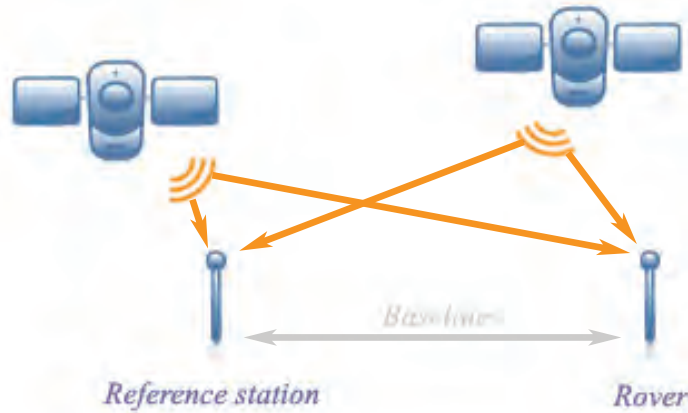
Figure 2.6: The concept of DGPS depicting the reference station, rover, satellites and the distance between the antennae (baseline). Adapted from Cannon & Lachapelle (2005).

tend to accumulate upon differencing measurements. For instance, since noise is assumed to be uncorrelated (white) and Gaussian in nature, the standard deviation increases by a factor of $\sqrt{2}$ with every differencing operation (see Equation 2.8). Therefore, while the noise on single differencing is increased by a factor of $\sqrt{2}$, the noise power in double differencing is increased by a factor 2, and in triple differencing by $2\sqrt{2}$, and so on:

$$\sigma_{noise} = \sqrt{\sigma^2 + \sigma^2} = \sqrt{2} \cdot \sigma. \tag{2.8}$$

Single differencing can be further sub-divided into two classifications: *single differencing between satellites*,

$$\triangledown = (\bullet)_{Satellite1} - (\bullet)_{Satellite2} \tag{2.9}$$

and *single differencing between receivers*,

$$\triangle = (\bullet)_{Receiver1} - (\bullet)_{Receiver2} \tag{2.10}$$

where $(\bullet)$ is any of the observations discussed previously. For example, using pseudoranges as in equation 2.5, equation 2.9 becomes,

$$\nabla = [p(t)]_{Satellite1} - [p(t)]_{Satellite2}$$

$$= \nabla\rho(t) + \nabla dT(t) + \nabla d_{orb}(t) + \nabla d_{ion}(t) + \nabla d_{trop}(t) + \nabla\eta_p. \quad (2.11)$$

Note the disappearance of the receiver clock term (dt). Since the receiver clock term is identical in both measurements taken by the same receiver, this factor is eliminated. Similarly, Equation 2.10 becomes,

$$\triangle = [p(t)]_{Receiver1} - [p(t)]_{Receiver2}$$

$$= \triangle\rho(t) + \triangle dt(t) + \triangle d_{orb}(t) + \triangle d_{ion}(t) + \triangle d_{trop}(t) + \triangle\eta_p. \quad (2.12)$$

Note again, the disappearance of the satellite clock term (dT) which is common to both measurements.

Double differencing is essentially an application of both single differences (between satellite and between receiver) at once. It can be expressed mathematically as follows:

$$\triangle\nabla = [(\bullet)_{Receiver1} - (\bullet)_{Receiver2}]_{Satellite1} - [(\bullet)_{Receiver1} - (\bullet)_{Receiver2}]_{Satellite2}. \quad (2.13)$$

For example, if pseudorange measurements are used, Equation 2.13 becomes

$$\triangle\nabla = \triangle \nabla \rho(t) + \triangle \nabla d_{orb}(t) + \triangle \nabla d_{ion}(t) + \triangle \nabla d_{trop}(t) + \triangle \nabla \eta_p. \quad (2.14)$$

Note both clock terms $(dt$ and $dT)$ have been eliminated in Equation 2.14. Double difference, phase observations are used in Chapter 7 as a reference navigation solution in order to assess the accuracy of the GPS/INS navigation solution.

Satellite Orbital Error (d_{orb})

As mentioned previously in this section, knowledge about the position of the satellites is paramount to the accuracy of the final position solution. Satellite orbital errors are a

result of the discrepancy between the true satellite position and the computed satellite position from the broadcast ephemeris.

Since the satellites' positions are computed from a predicted trajectory model that is created by the control segment there are inherent errors. Furthermore, the parameters defining these models are uploaded a maximum of three times per day. These errors are typically confined to only a few metres. Still, the typical error induced by the final position solution is on the order of 3-5 metres (Lachapelle 2007).

The satellite orbital error is considered a common mode error and is therefore greatly reduced by between-receiver differencing (Misra & Enge 2004). The geometric effects of an orbital error are obvious in the context of trilateration. It should also be apparent that the closer together the receivers (i.e. the more similar the geometry), the more effective the differencing is in reducing the effects of orbital errors. Typically, receivers located 100 km apart are able to reduce the orbital errors to less than 5 cm (*ibid*).

Ionospheric Error (d_{ion})

The ionosphere is a layer of the Earth's atmosphere extending from 50 km to 1000 km above the surface consisting of ionized gas (*ibid*). The ionization which results in mobile charges in the atmosphere is caused by radiation from the sun. As such, the effects of the ionosphere are variable with various solar conditions. For example, between day and night, or between stages of the solar cycle.

Since the electron content of the ionosphere affects the density of the air, it also affects the refractive indices of the various layers of the atmosphere. Concordantly, the signals emanating from the satellites are slowed from the nominal speed of light in a vacuum (c). This refractive effect also results in a code delay and a phase advance which accounts for the sign difference in equations 2.5 and 2.6.

Again, ionospheric errors are considered common mode because they effect the satellite signal in the direction of the line-of-sight from the receiver. Receivers in close prox-

imity experience signals in similar lines-of-sight and therefore the errors are similar. As such, differencing is an effective means of reducing ionospheric errors. For instance, the user equivalent range error due to the ionospheric effects for a satellite overhead after differencing between two receivers 100 km apart is on the order of 5-20 cm, but can inflate to 1 m in active ionospheric conditions (*ibid*). Also, satellites at low elevation angles are likely to experience more residual error since the signal travels through a greater length of ionosphere than a satellite broadcasting directly overhead.

Another method of eliminating ionospheric effects is to use a measurement that is based on the ratio of the L1 and L2 measurements, know as the *ionosphere free* observable (Cannon & Lachapelle 2005). While this is a very effective means of mitigating ionospheric errors, it is not used in this study and is not discussed further.

Tropospheric Error (d_{trop})

The troposphere is the layer of the Earth's atmosphere familiar to most people. It extends from the Earth's surface up to 50 km altitude (Cannon & Lachapelle 2005). This portion of the atmosphere is associated with weather and as such, contains variable humidity, temperature, pressure and other conditions that can affect the satellites' signals propagation. Since the tropospheric error is essentially cause by the impedance of the atmosphere on the signal, it is sometimes referred to as *tropospheric delay*.

The tropospheric error can be nominally divided into the *dry component*: resulting from the dry gasses in the troposphere, and a *wet component*: attributed to the water vapour content of the troposphere (Lachapelle 2007). Approximately 90% of the tropspheric delay is due to the dry component under normal weather conditions. Fortunately, the dry component is highly predictable and can be modelled with a 1% accuracy. The remaining 10% of the ionospheric error (i.e. the wet component) is difficult to model since water vapour varies with the local weather. As such, the accuracy of the wet component prediction is conservatively estimated at 10-20%.

Differencing is generally effective at reducing tropospheric errors since, much like iono-spheric errors, it affects the line-of-sight propagation of the satellites' signals. However, tropospheric errors can be highly spatially uncorrelated in particular weather conditions such as thunderstorms and cold fronts. In general, the residual errors due to tropospheric effects after modelling on two receivers spaced 100 km apart is on the order of 10-15 cm. These residual errors are sometimes higher for satellites at low elevation angles, much like for ionospheric errors.

Receiver Clock Error (dt)

Since the receiver's time piece is of much lower quality than the highly accurate satellite clock network, there exists an offset between the true GPS time and the time maintained by the receiver. This offset is known as the receiver clock error. Since the error is a result of the internal time keeping componentry, the error is common to all range measurements taken at a given epoch.

As such, given sufficiently redundant range measurements, the receiver clock error can be estimated in the GPS computations, and subsequently corrected. As detailed previously, another approach to removing the receiver clock error is to difference mea-surements taken between satellites. Since the error is common mode, the effects of the receiver clock error can be completely eliminated using this procedure.

Satellite Clock Error (dT)

The ability to maintain time aboard the satellites is one of the technological advances that makes satellite navigation possible. Highly precise Cesium and Rubidium oscillators, combined with corrections from the ground segment make GPS time one of the most accurate time references in the world (Kaplan & Hegarty 2006).

Clock correction parameters form part of the broadcast ephemeris. Essentially, these parameters form a second-degree clock deviation model that adjusts for satellite clock deficiencies. These values are uploaded from the ground segment to the satellite in timely
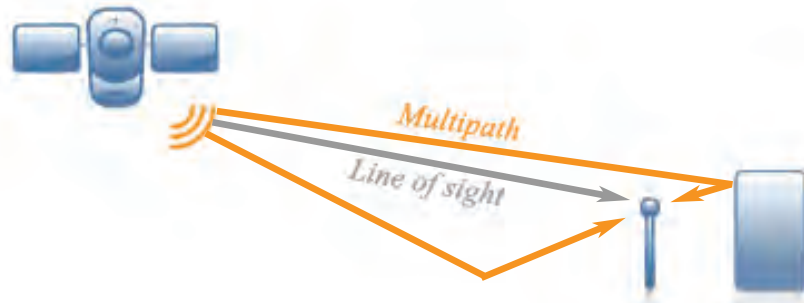
Figure 2.7: Multipath signals in GPS. Adapted from Godha (2006).

intervals to ensure accurate time keeping. The satellite clock error is a common mode error and as such is eliminated by between-receiver differencing.

Multipath

As discussed thus far, most errors associated with satellite navigation result from attenuation or disruption of the signal. Another cause of error is the accumulation of reflected signals by the receiver, or multipath (see Figure 2.7). The range estimate between the antenna and the satellite is assumed to be the straight line distance travelled by the signal from the satellite to the antenna. Any signal that is reflected one or more times before arriving at the antenna results in a delay and thus the range is distorted.

Since the possible sources of multipath are numerous (i.e. local buildings, ground, antenna housing, etc) and the specific delay is dependant on the localized geometry, multipath is not a common mode error. As such, multipath is additive upon differencing and forms a large fraction of the total error experienced in satellite-based location and position in many applications.

Receiver and System Errors

The final sources of error that will be discussed here are related to the system noise that is inherent to electronic measurements. Each electrical appliance experiences thermal noise and interference by outside systems. In most high end receivers, the noise effects are negligible in carrier phase measurements and a few decimetres in code phase. Moreover, these noise characteristics are deterministic in many cases and can be largely eliminated by performing *zero baseline calibration*, whereby two receivers are connected to the same antenna (Cannon & Lachapelle 2005). Since all other errors are common between the two receivers, any differences seen between receivers must be a result of receiver noise.

Summary of GPS Errors

The ability to eliminate certain errors in GPS measurements depends largely on their spatial correlation and the distance between the antennas from which the measurements are being differenced. Common mode errors are eliminated or greatly reduced through differencing, while non-common mode errors are potentially increased by differencing. Table 2.1 summarizes the GPS errors discussed above and gives a range of the magnitude of each error on the accuracy of the final position solution in single point and differential modes. Notice that some errors are completely eliminated by single differencing.

Table 2.1: GPS pseudorange error sources (Lachapelle 2007)

Error source	Single point [m]	Differential [ppm]
Orbital	3 - 5	0.1 - 0.5
Satellite clock	2 - 3*	-
Ionosphere	2 - 50	0.5 - 2
Troposphere	2 - 30	1 - 1.5
Code multipath	0.2 - 3**	-
Code noise	0.1 - 2	-
* After application of clock correction parameters		
** Under benign operating conditions		

2.3   Inertial Navigation System (INS)

An INS is a self-contained Dead Reckoning (DR) navigation system, which provides dynamic information about position and velocity, based on the measurements obtained from an Inertial Measurement Unit (IMU) (Jekeli 2001). An IMU consists of a triad of orthogonal accelerometers and gyroscopes. The basic operating principle of the IMU is Newton's *First Law of Motion*, which was stated in Section 2.1.1.

In effect, the force applied to the accelerometer results in an acceleration that can be quantified and measured. This acceleration, when integrated with respect to time, provides a change in velocity; and concordantly, when doubly integrated with respect to time, provides a change in position. Thus, an INS generically provides the *change* in position and velocity. In order to determine the body frame's position and velocity in an absolute sense the initial condition (initial position, velocity and attitude) must first be known (El-Sheimy 2007).

The computation of position and velocity from an IMU would thus seem simple: a straightforward time integration. However, as discussed in Section 2.1, the IMU records measurements in a different coordinate frame than position and velocity are usually expressed. The triaxial accelerations are given in the IMU body frame, whereas a user wanting map coordinates, for instance, requires the results in a LLF or ECEF frame.

Fortunately, by combining the acceleration measurements with knowledge of the attitude (or the change in attitude) of the IMU body frame, a series of transformations can be employed to acquire measurements in any of the coordinate frames discussed in section 2.1. For this reason, a triad of gyroscopes is usually installed in a similarly orthogonal triad to the accelerometers in an IMU. It follows that the accuracy of the angular measurements given by the IMU is fundamental to an INS, since errors in transformation of the acceleration measurements ultimately result in position and velocity errors. It is stated by El-Sheimy (2007) that the ability of an INS to enable the continuous

determination of position, velocity and attitude primarily depends on the quality of the gyroscope sensors used.

2.3.1 IMU Mechanization

Mechanization of the IMU measurements allow for the conversion of the specific acceleration (f^b) and angular velocity (ω^b) recorded by the IMU into useful position, velocity and attitude information (Savage 2000). Since the IMU measurements will be combined with GPS measurements in this study, the mechanization will require the expression of the IMU data in the ECEF frame. What follows in this section is largely influenced by El-Sheimy (2007).

The mechanization of the raw measurements obtained from an IMU (namely, accelerations and angular velocities in the IMU body frame) can be described as two distinct steps:

1. *The body sensed angular velocities are integrated with respect to time to compute the transformation matrix from the IMU body frame to the ECEF frame.* The specific angular velocity measured by the gyroscope includes the Earth's angular velocity as well as the IMU body's angular velocity. It is therefore necessary to remove the Earth's effect by transforming the Earth's angular velocity into the IMU body frame and detaching it from the recorded measurement. Once the IMU measurement has been adjusted, the rotation matrix from the IMU body frame to the ECEF frame (R_b^e) can be formed.

2. *The computed rotation matrix (R_b^e) is used to rotate the measured specific acceleration from the IMU body frame to the ECEF frame.* The specific acceleration measured by the IMU includes the IMU acceleration as well as the acceleration due to gravity (γ^e). The gravity vector must therefore be removed from the measured specific acceleration before the time integration to acquire velocity and position

changes.

The above two steps can be expressed mathematically by equation 2.15 from El-Sheimy (2007):

$$
\begin{bmatrix} \dot{r}^e \\ \dot{v}^e \\ \dot{R}_b^e \end{bmatrix} = \begin{bmatrix} v^e \\ R_b^e \langle a^b \rangle - 2\Omega_{ie}^e v^e + \gamma^e \\ R_b^e \left(\Omega_{ei}^b + \langle \Omega_{ib}^b \rangle \right) \end{bmatrix} \tag{2.15}
$$

where, dots ($\dot{\bullet}$) denote the derivative with respect to time, and the superscript 'b' ($\bullet^b$) and the superscript 'e' ($\bullet^e$) denote the IMU body frame and the ECEF frame, respectively. Also,

r^e is the position vector in the ECEF frame (x^e, y^e, z^e) (m),

v^e is the velocity vector in the ECEF frame (v_x^e, v_y^e, v_z^e) (m/s),

γ^e is the gravity vector in the ECEF frame (γ_x^e, γ_y^e, γ_z^e) (m/s^2),

R_b^e is the rotation matrix from the IMU body frame to the ECEF frame,

Ω_{ie}^e is the rotation rate of the Earth with respect to the inertial frame given in the ECEF body frame (rad/s),

Ω_{ei}^b is the rotation rate of the Earth with respect to the inertial frame given in the IMU body frame (rad/s),

Ω_{ib}^b is the rotation rate of the IMU body with respect to the inertial frame given in the IMU body frame (rad/s),

Note that the values in the angle braces ($\langle \bullet \rangle$) in equation 2.15 are the measurements collected from the IMU. Essentially, the system can be resolved in four steps which will be discussed in the following sections:

1. Correction of the raw data

2. Updating the attitude

3. Transformation of the specific acceleration to the LLF

4. Updating the position and velocity.

Correction of the Raw Data

Most low-cost IMUs have significant sensor errors, namely the turn-on bias, in-run bias, scale factors and other misalignment errors (Park & Gao 2002, Hou 2004). While a detailed discussion of these errors will be reserved for Section 2.3.2, it is sufficient to state that the nominal values for these errors can be attained through laboratory calibration or estimated in a Kalman Filter.

Once the sensor errors are acquired, the raw measurements can be scaled as follows:

$$\Delta\theta_{ib}^i = \frac{\Delta\tilde{\theta}_{ib}^b - b_g\Delta t}{1 + S_g} \tag{2.16}$$

$$\Delta v_f^i = \frac{\Delta\tilde{v}_f^b - b_a\Delta t}{1 + S_a} \tag{2.17}$$

where the tilde ($\tilde{\bullet}$) represents the raw measurements, and,

b_a, b_g are the biases for the accelerometer and gyroscope,

S_a, S_g are the scale factors for the accelerometer and gyroscope and,

Δt is the time increment of integration.

Updating the Attitude

As previously mentioned, the measured angular velocity of the IMU body is a combination of IMU body angular velocity and that of the Earth with respect to the inertial frame. It is therefore important to compute the angular increment of the Earth due to rotation

with respect to the IMU body frame in order to nullify the Earth's rotational effects on the measurement, as follows:

$$\Delta\theta_{ie}^b = R_e^b \cdot \omega_{ie}^e \cdot \Delta t = R_e^b \begin{bmatrix} 0 \\ 0 \\ \omega_e \end{bmatrix} \Delta t \qquad (2.18)$$

where ω_e is the Earth's rotation rate (15.041 °/h), and thus the angular increment due to the IMU body rotation with respect the ECEF frame is given by

$$\Delta\theta_{be}^b = \Delta\theta_{bi}^b - \Delta\theta_{ie}^b. \qquad (2.19)$$

Since the angular increments have been calculated, the rotation matrix that transforms from the IMU body frame to the ECEF frame (R_b^e) can be updated, and thereby update the attitude states. The preferred algebraic construct for rotational transformations for orthogonal systems is quaternions (Savage 2000) and can be updated with the computed angular increment, $\Delta\theta_{be}^b$ ($\Delta\theta_x^b$, $\Delta\theta_y^b$, $\Delta\theta_z^b$), as follows:

$$\begin{bmatrix} q_1 \\ q_2 \\ q_3 \\ q_4 \end{bmatrix}_{k+1} = \begin{bmatrix} q_1 \\ q_2 \\ q_3 \\ q_4 \end{bmatrix}_k + \frac{1}{2} \begin{bmatrix} c & s\Delta\theta_z^b & -s\Delta\theta_y^b & s\Delta\theta_x^b \\ -s\Delta\theta_z^b & c & s\Delta\theta_x^b & s\Delta\theta_y^b \\ s\Delta\theta_y^b & -s\Delta\theta_x^b & c & s\Delta\theta_z^b \\ -s\Delta\theta_x^b & -s\Delta\theta_y^b & -s\Delta\theta_z^b & c \end{bmatrix} \begin{bmatrix} q_1 \\ q_2 \\ q_3 \\ q_4 \end{bmatrix}_k \qquad (2.20)$$

where q_i is a complex representation of a vector, $c = 2\cos\frac{\theta}{2} - 1$, $s = \frac{2}{\theta}\sin\frac{\theta}{2}$ and $\theta = \sqrt{(\Delta\theta_x^b)^2 + (\Delta\theta_y^b)^2 + (\Delta\theta_z^b)^2}$.

From Savage (2000), it follows that the rotation matrix, R_b^e, can be computed as follows,

$$[R_b^e]_{k+1} = \begin{bmatrix} q_1^2 - q_2^2 - q_3^2 + q_4^2 & 2\left(q_1 q_2 - q_3 q_4\right) & 2\left(q_1 q_3 + q_2 q_4\right) \\ 2\left(q_1 q_2 - q_3 q_4\right) & q_2^2 - q_1^2 - q_3^2 + q_4^2 & 2\left(q_2 q_3 - q_1 q_4\right) \\ 2\left(q_1 q_3 + q_2 q_4\right) & 2\left(q_2 q_3 - q_1 q_4\right) & q_1^3 - q_1^2 - q_2^2 + q_4^2 \end{bmatrix} \tag{2.21}$$

At this stage, it is possible to compute the roll (ξ), pitch (η) and heading (ψ) with respect to the LLF with the rotation matrix that transforms from the IMU body frame to the LLF frame (R_b^l):

$$R_b^l = R_e^l \times R_b^e \tag{2.22}$$

$$\xi = -\tan^{-1}\left(\frac{\left(R_b^l\right)_{3,1}}{\left(R_b^l\right)_{3,3}}\right) \tag{2.23}$$

$$\eta = \sin^{-1}\left(\left(R_b^l\right)_{3,2}\right) \tag{2.24}$$

$$\psi = \tan^{-1}\left(\frac{\left(R_b^l\right)_{1,2}}{\left(R_b^l\right)_{2,2}}\right) \tag{2.25}$$

where $\left(R_b^l\right)_{p,q}$ is the element on the pth row and q^{th} column of the R_b^l matrix.

Transformation of the Specific Acceleration to the LLF

Since the rotation matrix (R_b^e) changes by a small amount between time $t = k$ and $t = k + 1$ an updated rotation matrix is needed for each epoch. However, it was shown above that the computation of the rotation matrix is complex and timely. For this reason, El-Sheimy (2007) suggests that the average orientation of the IMU during the time interval $t = k$ and $t = k + 1$ be used to form the rotation matrix, as follows:

$$\Delta v_f^e = (R_b^e)_k \left(I + \frac{1}{2} S^b \Delta v_f^b\right) \tag{2.26}$$

$$\Delta v_f^e = (R_b^e)_{k+1} \left(I + \frac{1}{2} S^b \Delta v_f^b \right) \tag{2.27}$$

where I is the identity matrix and S^b is the skew-symmetric form of the angular increments in equation 2.19.

Updating the Position and Velocity

Finally, the transformed velocity increment can be computed as in equation 2.28.

$$\Delta v^e = \Delta v_f^e - 2\Omega_{ie}^e v_k^e \Delta t + \gamma^e \Delta t \tag{2.28}$$

In the above equation, the second term $(2\Omega_{ie}^e v_k^e \Delta t)$ represents the correction for the Coriolis acceleration. Note that this term is calculated using the previous epoch's velocity (v_k^e). The third term $(\gamma^e \Delta t)$ is a correction for the gravity vector.

Once the transformed and corrected velocity increment is acquired, the final update to the body's velocity and position state can be performed, as in equations 2.29 and 2.30, respectively.

$$v_{k+1}^e = v_k^e + \Delta v^e \tag{2.29}$$

$$r_{k+1}^e = r_k^e + \frac{\Delta v_{k+1}^e + \Delta v_k^e}{2} \Delta t \tag{2.30}$$

Thus, the IMU mechanization is complete. The measurements given by the IMU were transformed and corrected to give the position and velocity updates and the attitude of the IMU body was determined. The process of IMU mechanization is depicted in Figure 2.8 as a summary of the last four sections.

2.3.2 IMU Sensor Errors

While Micro-Electro-Mechanical Systems (MEMS) technology has become one of the fastest growing sectors of the electronic technology market and is experiencing break-
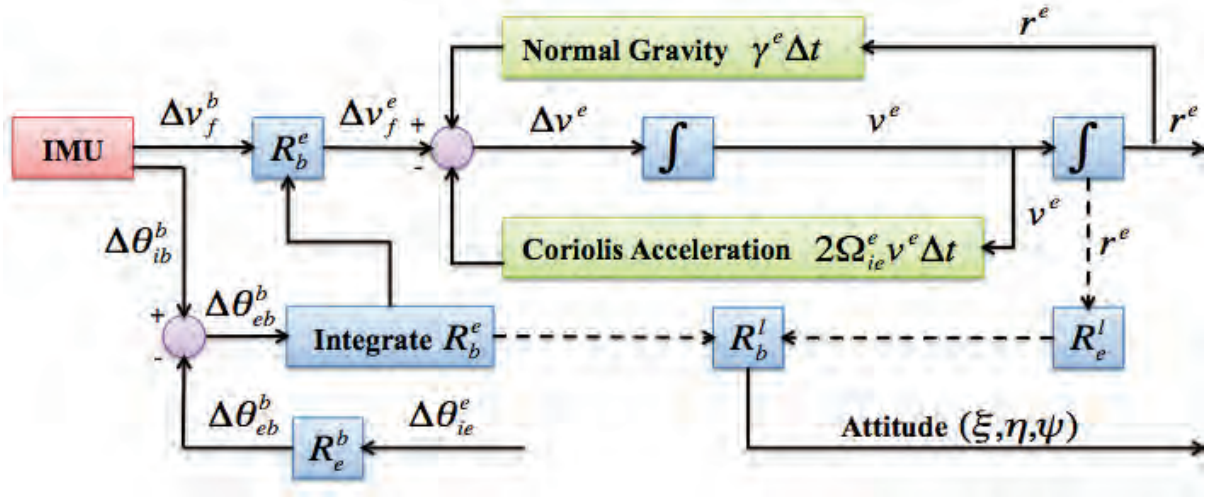
Figure 2.8: ECEF INS mechanization. Adapted from El-Sheimy (2007)

throughs on a seemingly daily basis, MEMS inertial devices have been unable to eliminate the error behaviour of their larger predecessors (Park & Gao 2002). In fact, smaller inertial devices are often subject to larger sensor errors since there is an effort to combine micro-scale manufacturing with low-cost components. These sensor errors are common to the accelerometer and the gyroscope and are called scale factors, turn-on biases (instability from successive turn-ons), drift (changes to the bias during usage) and noise. These errors and their affect on the inertial measurements can be summarized as follows (El-Sheimy 2007):

$$\tilde{f} = f + b_f + f \cdot S_f + f \cdot m_f + \eta_f \tag{2.31}$$

$$\tilde{\omega} = \omega + b_g + \omega \cdot S_g + \omega \cdot m_g + \eta_g \tag{2.32}$$

where,

- $\tilde{\bullet}$ represents the measurement recorded by the IMU,
- $\bullet_f$ represents an error characteristic of the accelerometer,
- $\bullet_g$ represents an error characteristic of the gyroscope,

f is the specific acceleration,

ω is the angular velocity,

b is the sensor bias,

S is the scale factor,

m is the error due to non-orthogonality of the sensor triad, and

η is the sensor noise.

Some of these errors are stochastic (random) in nature while others are deterministic. In order to account for the deterministic sensor errors (namely biases and scale factors), their nominal values must be estimated. There are two approaches that are commonly used to estimate the values of the sensor bias and scale factor (El-Sheimy 2007):

1. lab calibration, or

2. estimation as states in the process functional model.

The first approach is to determine the error characteristics through specific lab-controlled calibration and then correct the inertial measurements before using them in the navigational processing. The second approach is to include these errors as part of the functional model and estimate them as states (much like position and velocity are states). The second approach is adopted for this study since it is possible to account for changes the error characteristics while the sensor is being use.

Still, other errors, (namely the sensor noise) are stochastic in nature and must be modelled rather than estimated. This section provides a characterization of each of the these errors and details their stochastic and deterministic properties.

Noise

Noise is inherent to any electronic measurement. It is inherent to the sensor itself or any other electronic equipment that interferes with the output signals being measured

(Kay 1998). In general, noise is stochastic in nature; that is, it can not be estimated as a nominal value. Typically it is modelled as a zero-mean white Gaussian noise. For accelerometers and gyroscopes this means that the error attributed to noise is typically modelled as angular/velocity random walk, and the noise density is generally given units of $units/\sqrt{Hz}$.

The important consideration when dealing with noise is the power level of the noise compared with the signal power level. There are many ways to characterize the noise power for accelerometer and gyroscope measurements. Petovello (2003) characterized the noise power by taking the standard deviation of a few seconds of static data at several points along the data set. The mean of these standard deviations formed the heuristic approximation of the noise power.

A second method of determining noise power, as outlined in Skaloud (1999) and Nassar (2003), is based on wavelet decomposition of the data. Essentially, the signal and noise is successively broken down into low and high frequency components. While the low frequency components represent slow moving errors (i.e. bias drift), the higher frequency components represent the sensor's noise. The standard deviation is taken to be the noise power estimate much like in the method proposed by Petovello (2003).

Another method for IMU noise estimation is the Allan variance (e.g. El Sheimy et al 2008) whereby the noise characteristics of the inertial sensors can be modelled through the representation of the RMS random drift error as a function of averaging time. Although this method was not implemented in this thesis, the Allan variance is an effective means of noise characterization since it is directly observable and relatively easy to compute.

Sensor Bias

The inertial sensor bias is defined as the average of the output of each sensor over a specified time, measured at specific operating conditions that have no correlation with input acceleration or rotation (IEEE 2001). Since the error is expressed over a period of

time, the units for accelerometer bias and gyroscope bias are metres per square second (m/s^2) and degrees per hour (°/h), respectively.

There are typically two components to the sensor bias; the initial turn-on bias and the bias drift. Turn-on bias is deterministic and constant over a sortie of data. In most high-end IMUs the turn-on bias is negligible, but this is not the case for low-cost IMUs. Moreover, the turn-on bias in low-cost IMUs is not stable over time, thus requiring frequent calibration. The bias drift refers to the rate at which the error in inertial sensors accumulate over time (El-Sheimy 2007). This component of the sensor bias is not deterministic in nature, and is therefore modelled stochastically.

Scale Factors

A scale factor is the ratio of a change in the output relative to a change in the input intended to be measured (IEEE 2001). Since this value is a ratio it is unitless, and is typically given as parts per million (PPM). Typically the nominal value of the scale factor is constant both for high-end and low-cost IMUs. However, for low-cost IMUs the scale factor can change by small amounts and is therefore modelled stochastically using any suitable random process (El-Sheimy 2007).

Non-Orthogonality

The sensors in an IMU are to be mounted in an orthogonal triad (both accelerometers and gyroscopes). Manufacturing errors and general degradation of the sensor can lead to changes in the sensor assembly that result in the triad not being perfectly orthogonal to one another. This condition results in the measurements of each sensor in the triad becoming correlated to the others. Axes misalignment, in general, are modelled as part of the INS error equations (El-Sheimy 2007).

2.3.3 IMU Initial Alignment

When an IMU is turned on, the orientation of the IMU body coordinate frame is unknown. It is therefore necessary to perform an initial alignment of the IMU to establish the IMU body coordinate frame. This alignment consists of two modes; the *horizontal alignment* and the *heading alignment.*

Horizontal Alignment

The initial estimate of the rotations about the horizontal axes (roll and pitch) are acquired through a process called accelerometer levelling. Essentially the measurements from all three accelerometers in the orthogonal triad measure the gravity vector under static conditions. The computed velocity increments from the three sensors are then used to compute the roll (ξ^b) and pitch (η^b) of the IMU body using the following (Petovello 2003):

$$\xi^b = -\sin^{-1}\left(\frac{\Delta\bar{v}_x^b}{\gamma\Delta t}\right) \tag{2.33}$$

$$\eta^b = \sin^{-1}\left(\frac{\Delta\bar{v}_y^b}{\gamma\Delta t}\right) \tag{2.34}$$

where,

$\Delta\bar{v}_\bullet^b$ represents the time-averaged velocity increment in a given direction given in the IMU body frame,

γ is the nominal gravity value and,

Δt is the time interval over which the velocity increment is averaged.

Also important is the level of accuracy attained from these estimates. El-Sheimy (2007) has shown that the accuracy of the initial estimates of the IMU body roll and pitch are given respectively by

$$\delta\xi^b = \frac{(b_a)_x}{\gamma} \tag{2.35}$$

$$\delta\eta^b = \frac{(b_a)_y}{\gamma} \tag{2.36}$$

where $(b_a)_i$ is the accelerometer bias in the ith direction.

Based on Equations 2.35 and 2.36 above, the sensitivity of the level error to the accelerometer bias is 0.06 $°/mg$ (degree per milli-g). According to the data in Table 1.2, the accuracy of the coarse estimate of the roll and pitch for the Crista IMU^{TM} is 1.5°-2°.

Heading Alignment

Acquiring an initial estimate of the rotation about the the vertical axis is achieved through gyro compassing. In essence, knowledge about the rotation rate of the Earth is measured by all three gyroscopes in the orthogonal triad under static conditions. From the angular increments of the gyroscopes, the heading of the IMU body coordinate frame can be computed with (Petovello 2003):

$$\Delta\bar{\theta}_{ib}^h = R_1(-\eta)R_2(-\xi)\Delta\bar{\theta}_{ib}^b \tag{2.37}$$

$$\psi = -\tan^{-1}\left(\frac{(\Delta\bar{\theta}_{ib}^h)_x}{(\Delta\bar{\theta}_{ib}^h)_y}\right) \tag{2.38}$$

where $\Delta\bar{\theta}_{ib}^h$ is the time-averaged vertical component obtained after the roll and pitch estimates are applied.

Unfortunately, this procedure is only valid for IMUs that have a sensor bias and noise power that does not exceed the Earth's rotation rate (Grewal et al 2007). In the case of most MEMS IMUs today, this is not the case.

Another approach to heading alignment is to estimate the initial heading information from an external source such as a magnetic compass (magnetometer), which uses the ambient magnetic field to orient itself. Unfortunately, the ambient magnetic field is not consistent and is affected by any ferrous material (materials that themselves have a magnetic field).

The final approach discussed here is to perform dynamic heading alignment using GPS velocity measurements (Shin 2005), as follows:

$$\psi_{GPS} = \tan^{-1}\left(\frac{v_{GPS}^e}{v_{GPS}^n}\right) \tag{2.39}$$

where v_{GPS}^e and v_{GPS}^n are the east and north components of the GPS derived velocities in the LLF frame.

Since this approach is feasible in the context of this study, it is appropriate to discuss the accuracy of this approach. Hence the variance in the GPS-derived heading, as derived through covariance propagation, is given by

$$\begin{aligned}
\Delta\psi_{GPS}^2 &= \frac{(v_{GPS}^e)^2}{(v_{GPS}^e)^2 + (v_{GPS}^n)^2} \cdot (\Delta v_{GPS}^e)^2 + \frac{(v_{GPS}^n)^2}{(v_{GPS}^e)^2 + (v_{GPS}^n)^2} \cdot (\Delta v_{GPS}^n)^2 \\
&= \frac{(\Delta v_{GPS})^2}{v_{GPS}^2}
\end{aligned} \tag{2.40}$$

where

$(\Delta\bullet)^2 \quad$ represents the variance in $\bullet$

$v_{GPS}^2 \quad = (v_{GPS}^e)^2 + (v_{GPS}^n)^2.$

From Equation 2.40, the greater the horizontal velocity, the better the estimation of heading. Therefore, this method should only be used when the horizontal velocity is sufficiently high.

2.4   Photogrammetry

As mentioned in Chapter one, optical cameras have become the gold standard for human motion analysis. Moving forward, it is important to understand how these photogrammetric measurements are formed, and more importantly, describe the errors that are inherent to this system.

Fundamentally, optoelectric methods are positional - deriving the positions of optical markers in 3D space from information gathered in 2D pictures. The basic algorithm includes precise knowledge of camera parameters such as the focal length, lens distortions and sensor characteristics as well as precise knowledge of the cameras' positions in 3D space. From this information, colinearity equations are used alongside overlapping pictures to derive the subject's position. For a detailed discussion of photogrammetry read Schenk (2000).

2.4.1 Rotation Angles

A landmark study, Kidder et al (1996), described a method of optical marker placement that was instrumental in observing the various segments of the foot and ankle complex. The four foot model segments, as described in the Kidder study, were the shank (tibia and fibula), rearfoot (calcaneus, talus, and navicular), forefoot (cuneiforms, cuboid and metatarsals) and the big toe (hallux) - see Figure 1.3d. The lower limb model used in the rest of this study will be consistent with this model proposed by Kidder et al (1996).

The Kidder study was able to compute the rotations of the various segments of the lower limb and foot by evaluating the orientation of co-planar optical markers (see Figure 2.9 and Figure 2.10). For example, determining the orientation of the rearfoot involves forming a plane from the three markers placed on the posterior, lateral and medial aspects of the calcaneus as per the orange plane in Figure 2.9. Similarly, the orientation of the forefoot is determined by the markers placed on the medial and lateral metatarsals (blue plane), and the shank is determined by the markers placed on the anterior aspect of the tibia and the lateral and medial malleolae (green plane).

A simple method of determining the orientation of a plane at any given time is to analyze the normal vector ($\vec{n}$) to that plane. Equation 2.41 shows how cross product and positions of any three co-planar points define the normal vector. Equations 2.42, 2.43, and 2.44 show how the rotation around the x-axis (ω), y-axis (ϕ), and z-axis (κ)
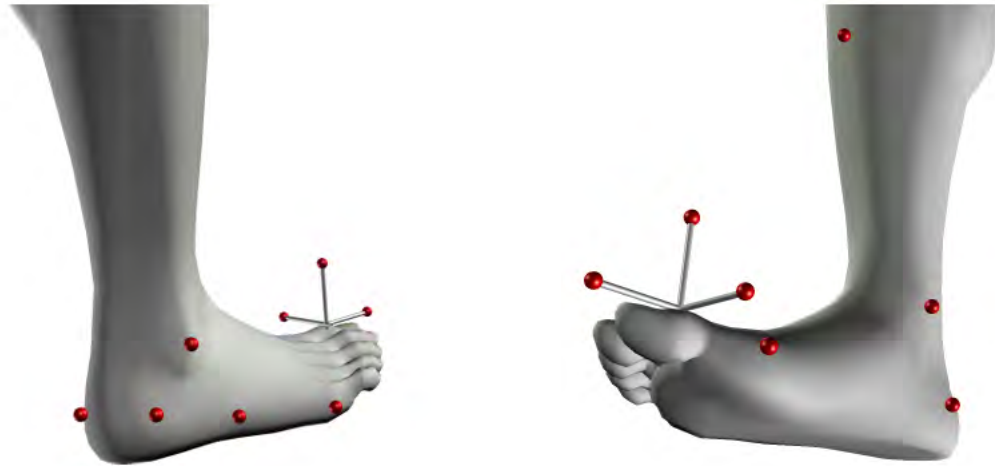
Figure 2.9: Placement of reflective markers to isolate the segments of the foot and ankle: Shank (anterior tibia, lateral and medial malleolae), Rearfoot (posterior, lateral and medial aspects of calcaneus), and forefoot (medial and lateral metatarsals). Adapted from Kidder et al (1996)
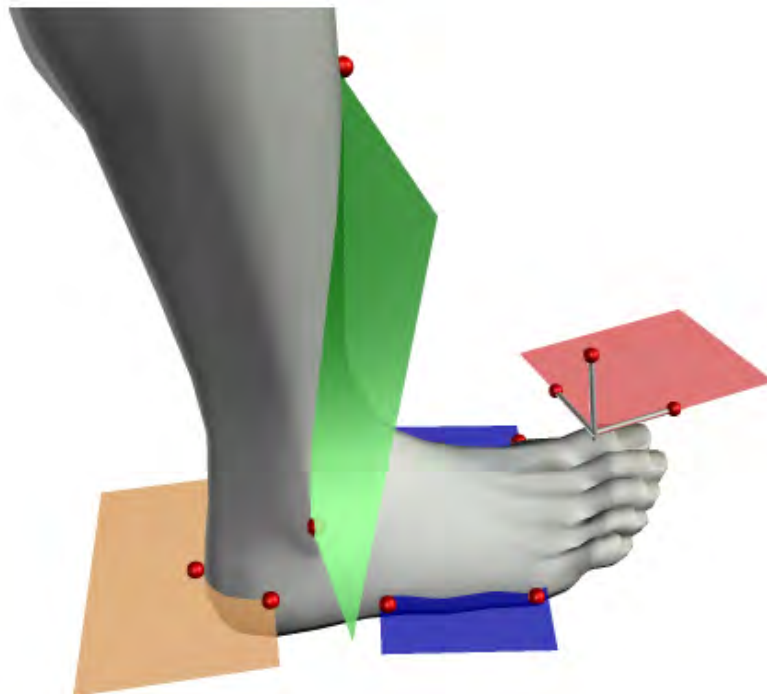
Figure 2.10: Planes formed by the placement of optical markers proposed by Kidder et al (1996). Each segment of the lower limb can be measured independently

are calculated from the 3D normal vector, respectively.

$$\vec{n} = \begin{bmatrix} x_2 - x_1 \\ y_2 - y_1 \\ z_2 - z_1 \end{bmatrix} - \begin{bmatrix} x_3 - x_1 \\ y_3 - y_1 \\ z_3 - z_1 \end{bmatrix} \tag{2.41}$$

$$\omega = \tan^{-1} \frac{z_n}{y_n} \tag{2.42}$$

$$\phi = \tan^{-1} \frac{x_n}{z_n} \tag{2.43}$$

$$\kappa = \tan^{-1} \frac{x_n}{y_n} \tag{2.44}$$

where x_n, y_n, z_n form the normal vector to the plane.

2.4.2 Errors in Rotation Angles

In this paper, the error in the measurements is of particular interest. Equation 2.45 shows the error in the angle measurement in terms of the normal vector. For brevity, only the error for ω is shown, but the errors for ϕ and κ are derived in a similar fashion:

$$\begin{aligned} \Delta\omega^2 &= \left(\frac{\delta\omega}{\delta z_n}\right)^2 \cdot \Delta z_n^2 + \left(\frac{\delta\omega}{\delta y_n}\right)^2 \cdot \Delta y_n^2 \\ &= \frac{\Delta z_n^2}{(z_n + 1)^2} + \frac{\Delta y_n^2}{(y_n + 1)^2} \end{aligned} \tag{2.45}$$

where $\Delta\bullet_n^2$ is the variance in $\bullet_n$.

Equations 2.46 show the error in the normal vector component (z_n) as a function of the positions and positional errors of the three markers respectively. Errors in the other normal vector components are derived similarly.

$$\Delta z_n^2 = \left(\frac{\delta\omega}{\delta x_1}\right)^2 \cdot \Delta x_1^2 + \left(\frac{\delta\omega}{\delta x_2}\right)^2 \cdot \Delta x_2^2 + \left(\frac{\delta\omega}{\delta x_3}\right)^2 \cdot \Delta x_3^2$$
$$+ \left(\frac{\delta\omega}{\delta y_1}\right)^2 \cdot \Delta y_1^2 + \left(\frac{\delta\omega}{\delta y_2}\right)^2 \cdot \Delta y_2^2 + \left(\frac{\delta\omega}{\delta y_3}\right)^2 \cdot \Delta y_3^2 \qquad (2.46)$$
$$= (2y_2 - y_1 - y_3)^2 \cdot \Delta x_1^2 + (y_3 - y_2)^2 \cdot \Delta x_2^2 + (y_1 - y_2)^2 \cdot \Delta x_3^2$$
$$+ (x_3 - x_1)^2 \cdot \Delta y_1^2 + (2x_1 - x_2 - x_3)^2 \cdot \Delta y_2^2 + (x_2 - x_1)^2 \cdot \Delta y_3^2$$

From equations 2.45 and 2.46, the quality of the orientation of the plane is given in terms of the positions of the markers and variance of those positions, thus the mathematical model is defined. These values (positions and variance) are typically arrived at through Least Squares Adjustment or like calculations.

Since the plane is determined by measuring the positions of the markers in 3D space, the factors that influence the quality of those positions are important. The quality of the position observations is dependant on four factors (Habib 2007).

1. *Primitive registration.* The ability to locate the marker in a reliable fashion in photographs depends on both the resolution (i.e. the granularity of the pixels) and the radiometric quality of the image. In the Kidder study, the centroid of the markers was measured to determine the position of the marker in all images. This has two benefits: firstly, automated computer algorithms can be defined to perform centroid determination, and second, the centroid of spherical figures is relatively easy to determine and thus there is little computational load. The identification of the markers is also made more complicated by blurring of features in the image, so in cases of high dynamics, (i.e. running), the precision of the system is expected to decrease (see Figure 2.11).

2. *Internal and external orientation calibration.* The calibration of the cameras internal parameters and position calibration. Since photogrammetry is an application of
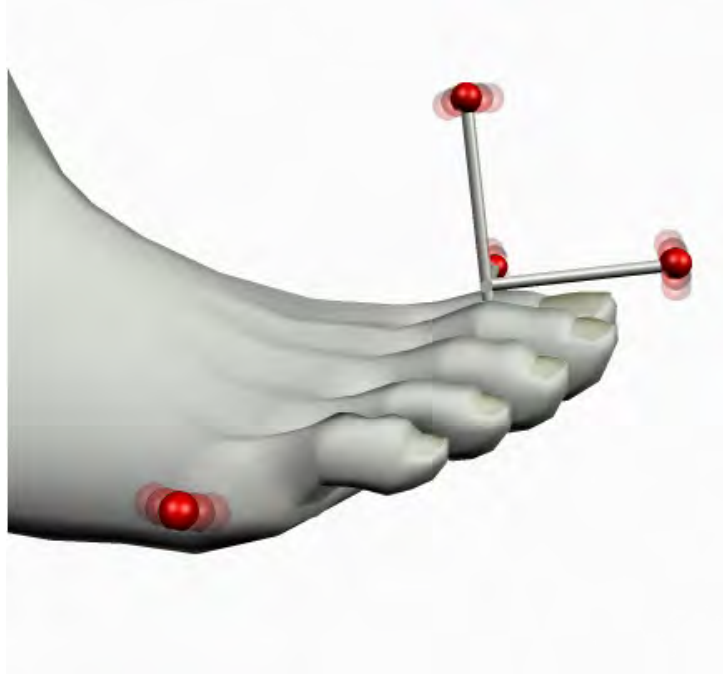
Figure 2.11: Registration of optical markers can be difficult to automate. Insufficient shutter speed can cause motion blur in the images making it hard for image processing algorithms to define the markers

collinearity observations involving the incident light bundles to the camera, knowledge of the internal camera characteristics (i.e. focal length, radial lens distortion coefficients, de-centring lens distortion coefficients, etc.) is crucial to the precision of the system. For this reason, the system must either be calibrated often or requires the use of expensive metric cameras whose metrics come documented by the manufacturer and stay static over time.

3. *Geometry.* The geometry of the markers placement affects the reliability of the measurements. For instance, the markers placed on the rearfoot in the Kidder study are placed in an approximately 90° configuration which means that the quality of the roll and pitch measurements are similar in magnitude. However, the markers that demarcate the shank form a narrower triangle which makes the determination of heading slightly more sensitive to noise than the roll and pitch angles.

4. *Coordinate Control.* Adequate control points are needed to orient the subject rela-

tive to the local coordinate frame. In order to orient the observations in a meaning-ful coordinate frame (i.e. a horizontal local frame) each image must have at least three markers that orient the photograph. In the Kidder study, the triad located on the Hallux was used in this capacity. The weakness in this design is that the Hallux is itself part of the dynamic system and therefore subject to noise associated with movement.

The last consideration for kinematic analysis using the optical approach is the reg-istration of markers across multiple frames. Since the markers are constantly moving, the markers are expected to be in different positions in sequential frames of the video captured. The problem is then matching each marker with its conjugate in the following frames. To this end, Kidder employed a marker-of-least-movement matching algorithm. In this case, since the frame rate of the video was two hundred frames per second, the movement of each marker was smaller than half the distance between markers and thus the Euclidean distance of the points to their nearest conjugate in subsequent frames acted as the matching algorithm.

Chapter 3

Estimation Methods

This chapter provides an overview of the of the estimation theory that was used in this research. More specifically, the discrete time, linear and non-linear Kalman filters which were used are described in detail. For an exhaustive treatment of the Kalman filters used here, please refer to Grewal et al (2007) and Grewal (2007).

3.1   Estimation

For the purpose of this study, estimation is a process of obtaining a unique set of values for a set of parameters from a set of observations. This requires that there is a functional relationship between the unknown parameters and the observations (Grewal 2007). Or in a mathematical sense, there must exist a transformation (H) from the parameter space (x) into the observation space (z). This mathematical relationship is expressed as a function of time (t):

$$z(t) = H(t)x(t) + \eta(t) \tag{3.1}$$

where,

$\quad H(t) \qquad$: is the design matrix of the system,

$\quad x(t) \qquad$: is the parameter state vector, and

$\quad \eta(t) \qquad$: is the measurement noise.

Therefore, the parameter space can be resolved if the number of independent observations (m) is equal to or greater than the number of parameters (n). In the event that

that the number of observations exceeds the number of parameters $(m > n)$ then an averaging can be employed such as Least-Squares Estimation (LSE), which minimizes the measurement residuals for a given solution. Such methods optimize the set of parameters.

As with any linear system, in the event that the number of observations is less than the number of parameter $(m < n)$ then a unique parameter state can not be formed. This is a result of parameter space being a one-for-one transformation from the observation space (Equation 3.1). However, the formation of the parameter space can be performed using more information than just the measurements. For instance, the parameters' dynamics can be used to formulate the parameter state space, as follows:

$$\dot{x}(t) = F(t)x(t) + G(t)w(t) \tag{3.2}$$

where the dot ($\dot{\bullet}$) denotes a time derivative, and

$\quad F(t) \quad$: is the system dynamic matrix,

$\quad x(t) \quad$: is the parameter state vector,

$\quad G(t) \quad$: is the noise shaping matrix, and

$\quad w(t) \quad$: is the process driving noise.

This requires previous knowledge of the parameter space behaviour, but allows for fewer measurements to be used in determining the parameter space. An estimator that uses both the relationship between the measurement space and parameter space (Equation 3.1) and the knowledge of system dynamics (Equation 3.2) is the Kalman filter.

In order to place this discussion in the context of this research, human locomotion is a highly repeatable movement with confined dynamics. Since the measurements (positions, velocities, accelerations and rotation rates) can be transformed into the parameter space (positions, velocities and time) and the parameters dynamics are roughly determined, the Kalman filter is an optimal estimator for this research. For this reason, the Kalman

filter is used to transfer the GPS and INS measurements into position, velocity and time parameters.

Since the measurements provided by the sensors are given in discrete time intervals, and the parameters are to be estimated at specified epochs rather than in continuous time, an important adaptation had to be made to the estimation equations 3.1 and 3.2.

A discretized Kalman filter is used in these cases. The discrete time adaptation of Equation 3.2 is

$$x_{k+1} = \Phi_{k+1,k} x_k + w_k \tag{3.3}$$

where,

$\Phi_{k+1,k}$: is the state transition matrix between time t_k and t_{k+1},

x_k : is the parameter state vector at time t_k, and

w_k : is the process driving noise.

The most important distinctions between Equations 3.2 and 3.3 are the differences that exist between the system dynamic matrix ($F(t)$) and the discrete-time state transition matrix ($\Phi_{k+1,k}$). In fact, the two are congruent if $F(t)$ is time-invariant over the transition time interval. In cases where $F(t)$ is not time-invariant, special adaptation must be made. However, Petovello (2003) has shown that shortening the transition time interval mitigates much of the error. The state transition matrix as a Taylor series expansion in terms of the system dynamic matrix is

$$\Phi = e^{F\Delta t} = I + F\Delta t + \frac{(F\Delta t)^2}{2} + ... \tag{3.4}$$

where I is the identity matrix and Δt is the transition time interval.

A quantity that remains as yet unmentioned is the process driving noise (w_k). This element allows for a certain variability (or dynamics) in the parameter space, otherwise

known as process noise. This quantity is considered random in nature with a zero-mean distribution. The variance of the process driving noise can be represented as a variance matrix, Q_k, in discrete time. It can be expressed in terms of the integral of the continuous time process noise matrix $Q(t)$, as follows:

$$Q_k = \int_{t_k}^{t_{k+1}} \Phi_{k+1,\tau} G(\tau) Q(\tau) G^T(\tau) \Phi_{k+1,\tau}^T d\tau \tag{3.5}$$

Lastly, the measurement model shown in Equation 3.1 can be shown in its discretized form:

$$z_{k+1} = H_{k+1} x_{k+1} + \eta_{k+1} \tag{3.6}$$

where η_{k+1} is the measurement noise. This value is often determined by manufacturers' specifications or sensor calibration and is assumed to be zero-mean and normally distributed value with a variance that can be represented with a variance-covariance matrix, R_{k+1}.

3.1.1   Kalman Filter

A Kalman filter is a recursive algorithm that first predicts the state of the unknown parameters forward to the next epoch based on knowledge of the parameters' dynamics and then updates the parameter states with a weighted average of measurements and the predicted states (Grewal 2007). The Kalman filter algorithm assumes that the parameter space can estimated forward in time by Equation 3.3, and that the parameter space can be mathematically related to the measurement space by Equation 3.6. As mentioned previously, it is also assumed that the process driving noise (w_k) and the measurement noise (η_k) are uncorrelated, zero-mean and normally distributed.

The first task in the Kalman filter algorithm is the prediction of the parameter states and their uncertainties. This prediction is based on the current estimate of the parame-

ter's state and the knowledge of the parameter space dynamics. This prediction gives an *a priori* estimate of the parameters state for the next time epoch. The prediction of the parameter state and the uncertainty in the parameter state are respectively computed by

$$\hat{x}_{k+1}^{(-)} = \Phi_{k+1,k}\hat{x}_k^{(+)} \tag{3.7}$$

$$P_{k+1}^{(-)} = \Phi_{k+1,k}P_k^{(+)}\Phi_{k+1,k}^T + Q_k \tag{3.8}$$

where,

$\hat{\bullet}$: represents a predicted value,

$\bullet^{(-)}$: represents a predicted quantity before the measurement update,

$\bullet^{(+)}$: represents a predicted quantity after the measurement update, and

P_k : is the variance-covariance matrix of the estimated parameters at time, t_k.

The second task in the Kalman filter algorithm is the update of the parameter states and their uncertainties by weighting the new measurements and the predicted parameter states along with their uncertainties. In order to perform this step, two items are required; first, the updates calculated from predicted dynamics and by measurements, and second, a weighting mechanism to weight the updates accordingly.

The first step is accomplished by formulating an innovation sequence (v_{k+1}). Essentially, the innovation sequence is the difference between the measured observation (z_{k+1}) and the predicted observation ($\hat{z}_{k+1}$), and thus represents the amount of new information introduced in the system by the measured observations. It is computed by using

$$v_{k+1} = z_{k+1} - \hat{z}_{k+1} = z_{k+1} - H_{k+1}\hat{x}_{k+1}^{(-)}. \tag{3.9}$$

The second step is accomplished by formulating the Kalman Gain matrix (K_{k+1}). It is a factor that weights the innovation series and therefore regulates the effect of the measured observations of the state of the next epoch's parameters. For a detailed discussion of the Kalman Gain, refer to Grewal et al (2007). The mathematical formulation of the Kalman Gain is

$$K_{k+1} = P_{k+1}^{(-)} H_{k+1}^T \left(H_{k+1} P_{k+1}^{(-)} H_{k+1}^T + R_{k+1} \right)^{-1}. \tag{3.10}$$

Finally, the parameter states and their uncertainties can be updated using the innovation sequence and the Kalman Gain. The update of the parameter states and the parameter uncertainties are respectively

$$\hat{x}_{k+1}^{(+)} = \hat{x}_{k+1}^{(-)} + K_{k+1} v_{k+1} \tag{3.11}$$

$$P_{k+1}^{(+)} = (I - K_{k+1} H_{k+1}) P_{k+1}^{(-)}. \tag{3.12}$$

As mentioned previously, the Kalman filter algorithm is a recursive technique. This means that the parameters estimated at one epoch are carried forward and used in the next epoch. In the case of Kalman filtering, the updated parameters for this epoch $(\hat{x}_{k+1}^{(+)})$ and their uncertainties $(P_{k+1}^{(+)})$ are carried forward to the next epoch and made $\hat{x}_k^{(+)}$ and $P_k^{(+)}$, respectively. Figure 3.1 depicts the recursive nature of the Kalman filter algorithm.

3.1.2   Non-linear and Extended Kalman Filter

In the previous section, the underlying assumption, by virtue of using linear operations, was that the parameter dynamics and the measurements could be linearly transformed into the parameter space and *vice versa*. However, in the case of satellite navigation, the relationships between the measurements (ranges and Doppler) and the parameters (position, velocity and time) are not linear.
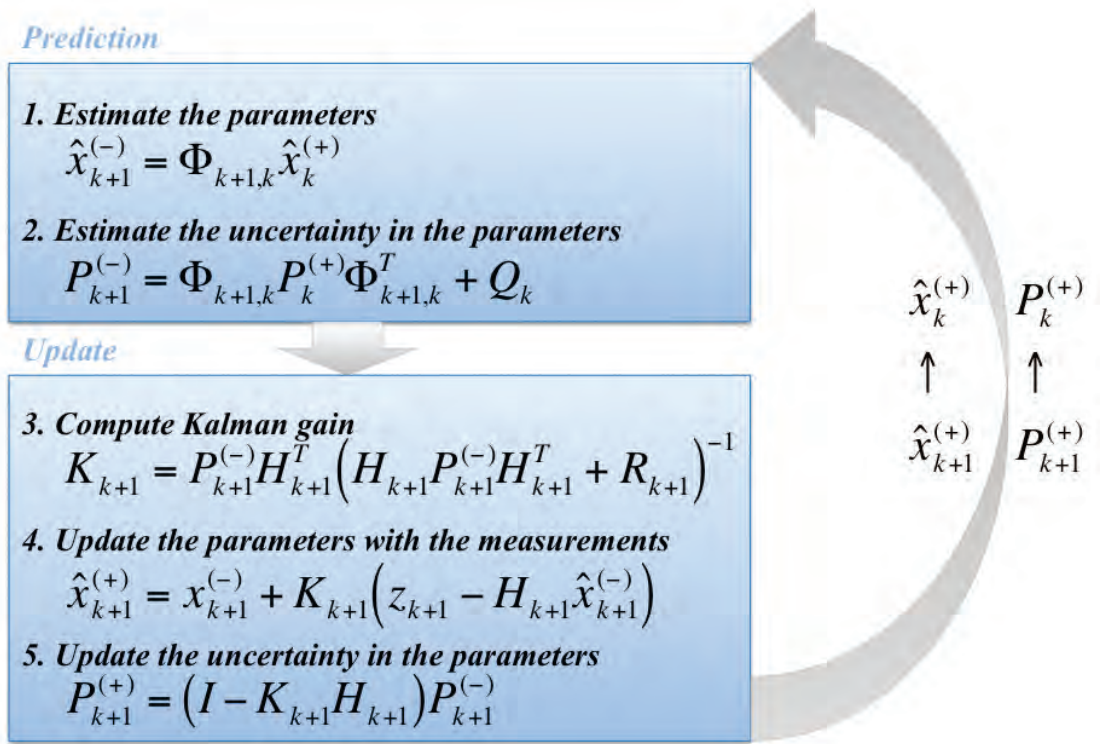
Figure 3.1: Discrete-time Kalman filter algorithm

The approach for non-linear cases such as this, is to linearize the system model first and then apply the regular Kalman filter algorithm to obtain the parameter states (Grewal et al 2007). As such, the non-linear process and measurement models are given by

$$x_{k+1} = f(x_k, k) + w_k \tag{3.13}$$

$$z_{k+1} = h(x_{k+1}, k+1) + \eta_{k+1} \tag{3.14}$$

where f and h are known, non-linear functions of the parameters. Since the process dynamics and the measurement themselves are a function of the parameters, it is necessary to have a nominal estimate of the parameters before the filter can be initiated. Subsequent iterations of the filter involve updating the nominal values with perturbations, as

follows:

$$x_{k+1} = x_{k+1}^* + \delta x_{k+1} \tag{3.15}$$

where,

$\bullet^*$: represents the nominal state of the parameters, and

$\delta \bullet$: represents perturbation from the nominal value.

Assuming the perturbations are sufficiently small, the first-order Taylor series expansion of Equations 3.13 and 3.14 is performed about the selected nominal trajectory to formulate

$$\delta x_{k+1} = \Phi_{k+1,k} \delta x_k + w_k \tag{3.16}$$

$$\delta z_{k+1} = H_{k+1} \delta x_{k+1} + \eta_{k+1}. \tag{3.17}$$

Equation 3.16 is the linear process model for a linearized Kalman filter, with the state vector being replaced by the parameter perturbations (δx_{k+1}). Likewise, Equation 3.17 reflects the linear measurement model, with the measurement vector replaced with measurement misclosures between the measured and predicted observations. In addition, the transition matrix ($\Phi_{k+1,k}$) and the design matrix (H_{k+1}) in the above equations are now a function of the partial derivatives of the non-linear functions with respect to the parameters, evaluated at the selected nominal values of the parameters.

In the linearization case described above, the nominal values selected for the parameters around which the linearization is performed is predetermined. This is known as a Linearized Kalman filter (LKF). In another scenario, the nominal values of the parameters are updated at every epoch with the newly estimated values of the parameters. As

such, the point around which the linearization is performed is constantly changing. This second scenario is known as the Extended Kalman filter (EKF). After the linearization is performed, the regular Kalman filter algorithm is performed to acquire the updated parameter states.

3.2 Reliability Testing

One of the main concerns of any navigation or positioning system is erroneous measurements (Kaplan & Hegarty 2006). In GPS/INS, the faulty measurements that are of concern are the pseudoranges from the GPS receiver (Kuusniemi 2005). This is due to the pseudorange's susceptibility to code noise, multipath, and low C/N_o. Blunders can not be compensated with the given measurement noise model since a blunder occurs too far away from the mean of the assumed white, Gaussian noise model. For this reason, it is paramount to perform blunder detection on the GPS measurements and reject erroneous measurements before they are used in the navigation/position solution.

Reliability testing is thus the action of ensuring that these faulty measurements are discarded, and thereby ensuring that the measurement model is reliable. In practise, this is implemented by pre-screening the incoming measurements and ensuring that measured observations are comparable to the predicted measurements. In the context of Kalman filtering, these misclosures are contained in the innovation sequence, thus making it easy to perform the reliability test, since innovations are necessarily zero-mean and normally distributed so that

$$v_{k+1} \sim N(0, \sigma_{v,k+1}^2) \tag{3.18}$$

with a variance defined by

$$\sigma_{v,k+1}^2 = H_{k+1} P_{k+1}^{(+)} H_{k+1}^T + R_{k+1} \tag{3.19}$$

where,

$N(p,q)$: denotes a normal distribution with p mean and q variance, and

$\sigma^2_{v,k+1}$: is the variance of the innovation sequence at time, t_k.

Since blunders necessarily depart from the mean by many multiples of the standard deviation, they are apt to cause a non-zero-mean condition, thereby breaking the above assumption. In the notation used by Teunissen & Salzmann (1989), Equation 3.18 becomes the following:

$$v_{k+1} \sim N(M_{k+1}\nabla_{k+1}, \sigma^2_{v,k+1}) \qquad (3.20)$$

where,

M_{k+1} : is a transformation matrix from the blunder space to the measurement space, and

∇_{k+1} : is a vector of blunders.

Since the presence of a blunder results in a measurable departure from zero-mean, the method for detecting blunders can be a two-part statistical procedure. The first step, called the *Global Test*, is a Chi-Squared statistical test to determine if there are any inconsistencies in the measured observations as a whole. If this test passes, it is concluded that no blunders exist. However, if the test fails, (i.e. a blunder is present amongst the measured observations) then the second step; the *Local Test* is performed. In this step, each misclosure is tested individually to isolate the blunder. If the blunder is identified, it is removed from the measurements, and the two step process is initiated again until no blunders can be identified. At this point the reliability testing is considered complete. For a treatment of the reliability testing procedure as applied to GPS/INS positioning see Petovello (2003).

Chapter 4

GPS/INS Integration

In the past two chapters the basis of GPS, INS and estimation has been discussed. This chapter begins with the conceptualization of GPS/INS integration. While two integration strategies are available - namely, *Loose Coupling* and *Tight Coupling* - only the latter is presented here. Reasons for selecting the tightly coupled over the loosely coupled architecture are also addressed.

Various aspects of GPS/INS integration are explained including the usage of GPS and INS measurements in an integrated model as well as the use of zero-velocity conditions to mitigate estimated parameter errors.

A brief discussion is given at the end of this chapter about the software that was developed to this end and consideration is given to implementing the algorithms in real-time, although all of the results shown in this thesis were done post mission.

4.1   GPS/INS Integration Strategies

In most applications, GPS and INS are integrated in one of two ways: loose coupling and tight coupling. The two strategies differ in the type of information that is shared between the two systems and in the structure of the computations that are performed.

Godha (2006) and Petovello (2003) offer excellent descriptions of the two integration strategies. For brevity, only the tightly coupled GPS/INS architecture is described here and particular attention is paid to the modifications that were made to gather kinematic information.

Two basic implementations exist concerning how INS measurements are handled. The first is called the *open loop* which deals with the estimation of the INS errors using GPS

information, and does not interfere with the operation of the INS. The second is called the *closed loop*, since it involves compensation of the sensor errors within the mechanization scheme using estimated bias and scale factors that are computed in the Kalman filter (Nayak 2000).

For this thesis, a closed loop implementation was considered. This is an important departure from the inertial kinematic studies that were reviewed in Section 1.3.3, since sensors error are typically determined through calibration and are assumed constant.

4.1.1 Tightly Coupled GPS/INS Integration

Tightly coupled GPS/INS uses a single centralized Kalman filter to process the final navigation solution. The inputs into the Kalman filter are the differences between the measured GPS pseudoranges and Doppler and the predicted pseudoranges and Doppler derived from the IMU mechanization. Much like the loosely coupled integration strategy, the filter estimates the position and velocity changes and applies them to the INS results. Figure 4.1 depicts the tightly coupled integration strategy.

The tightly coupled integration strategy has multiple inherent advantages over the loosely coupled scheme. First, since the measured GPS pseudoranges and Doppler are used (rather than a full GPS navigation solution), there is no requirement for a minimum number of satellites. Any pseudorange or Doppler measurement can aid the solution, and thus a tightly coupled filter is ideal in circumstances where there is low GPS availability, such as in urban environments or indoors.

Second, the use of a single filter means there is no requirement to artificially inflate the process noise, as in the loosely coupled integration strategy. This means that the process can be more accurately modelled without processing artifacts being added to the computations. This represents a significant statistical advantage for tightly coupled systems over loosely coupled ones.

Of late, the use of tightly coupled integration between GPS and INS is gaining pop-
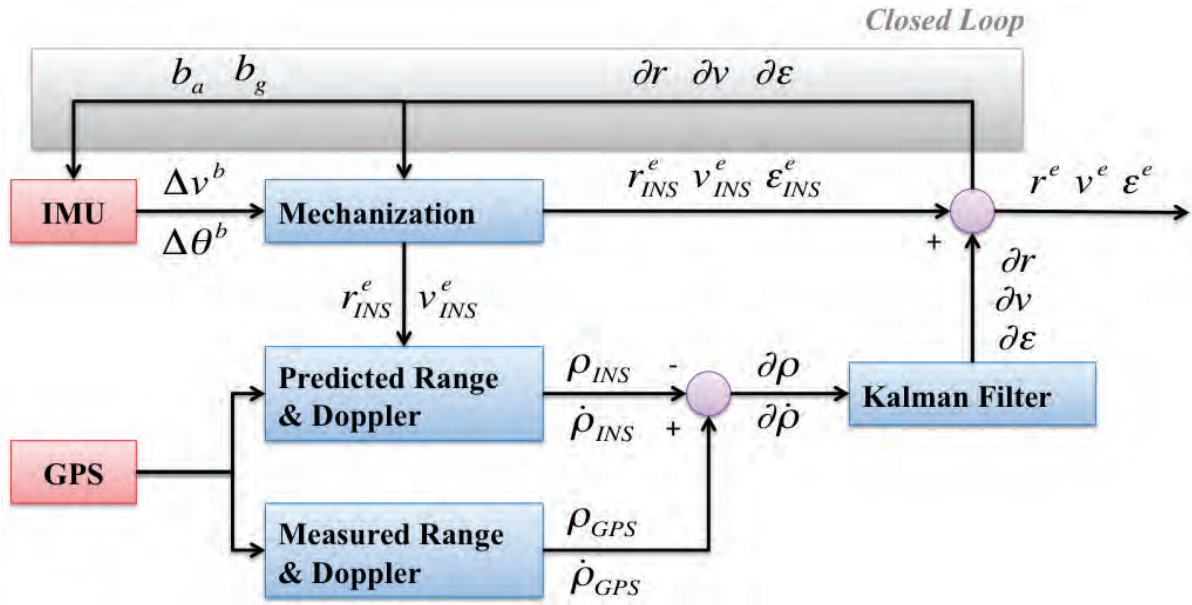
Figure 4.1: Closed loop, tightly coupled GPS/INS integration algorithm

ularity in the literature (Godha 2006). A likely cause of this is the ability for tightly coupled systems to use sub-optimal GPS availability to aid the navigation solution. In this study, the tightly coupled integration strategy is favoured because of the statistical improvements over the loosely coupled approach and better navigational performance.

4.2   GPS Filter

In Section 2.2, the GPS measurements were described as a range estimate (pseudorange or carrier measurements) and a velocity estimate (Doppler). The challenge is thus to provide a mathematical relationship between these measurements and the desired parameters. In scenarios where the antenna is static or moves very little only the position needs to be estimated (P model). In these cases, observing the velocity adds very little information since the antenna is assumed to stay in the same position (Grewal et al 2007). In circumstances where the antenna is assumed to move at a constant velocity, both the position and velocity can be estimated (PV model), or at constant acceleration, the acceleration parameters can be estimated as well (PVA model).

If the antenna is moving, than the PV model has been shown to have better performance than the P model (Grewal et al 2007). In pedestrian navigation, the antenna is assumed to move and thus both the position and velocity are estimated, the latter being modelled as a random walk process. As such, there is no appreciable gain in using the PVA model over the PV model (Godha et al 2006), and so the PV model is described here.

For this thesis, the measurements include GPS pseudorange and Doppler measurements. As such, the parameter space is augmented with the receiver clock error. Since receiver clocks experience first and second order effects, both the receiver clock bias and the receiver clock drift are estimated.

4.2.1   System Model

In light of the previous discussion, the GPS filter must contain both navigation and sensor error parameters. The navigation error parameters are represented in vector form by

$$x_n = \left[\overbrace{\delta r_x^e \quad \delta r_y^e \quad \delta r_z^e}^{\delta r^e} \quad \overbrace{\delta v_x^e \quad \delta v_y^e \quad \delta v_z^e}^{\delta v^e} \right]^T \tag{4.1}$$

where,

δr^e : is the position error vector in the ECEF frame $(\delta r_x^e,\ \delta r_y^e,\ \delta r_z^e)$, and

δv^e : is the velocity error vector in the ECEF frame $(\delta v_x^e,\ \delta v_y^e,\ \delta v_z^e)$.

Recall that the position error dynamics is simply the error in velocity and that the velocity error dynamics is modelled as a random walk process. Thus, the position and velocity error dynamic model is given by

$$\delta \dot{r}^e = \delta v^e \tag{4.2}$$

$$\delta \dot{v}^e = \eta_v$$

where,

$\dot{\bullet}$: denotes the time derivative, and

η_v : is the velocity process noise.

The velocity process noise variance (q_v) is assumed to reflect the dynamics of the body frame, and is thus estimated by the standard deviation of the accelerations experienced by the body frame.

As mentioned, the sensor error parameters describe the receiver clock bias and drift, and are represented by

$$c\dot{t} = c\delta t + c\eta_t \tag{4.3}$$

$$c\dot{\delta t} = c\eta_{\delta t}$$

where,

c : denotes the speed of light,

η_t : is the clock error noise, and

$\eta_{\delta t}$: is the clock drift noise.

In order to compute the clock error variance (q_t and $q_{\delta t}$), a standard clock stability model is used (Jekeli 2001). This model is shown here as follows:

$$q_t = 2h_0 \qquad (4.4)$$

$$q_{\delta t} = 8\pi^2 h_2 \qquad (4.5)$$

where,

h_0, h_2 : denote the Allan variance parameters of the receiver clock.

Concordantly, the final system model can be expressed by combining Equations 4.2 and 4.3, written here in state-space form as

$$
\overbrace{\begin{bmatrix} \delta \dot{r}^e \\ \delta \dot{v}^e \\ \dot{t} \\ \delta \dot{t} \end{bmatrix}}^{\dot{x}} = \overbrace{\begin{bmatrix} 0_{3\times3} & I_{3\times3} & 0 & 0 \\ 0_{3\times3} & 0_{3\times3} & 0 & 0 \\ 0_{1\times3} & 0_{1\times3} & 0 & 1 \\ 0_{1\times3} & 0_{1\times3} & 0 & 0 \end{bmatrix}}^{F} \overbrace{\begin{bmatrix} \delta r^e \\ \delta v^e \\ t \\ \delta t \end{bmatrix}}^{x} + \overbrace{\begin{bmatrix} 0_{3\times3} & 0 & 0 \\ I_{3\times3} & 0 & 0 \\ 0_{1\times3} & c & 0 \\ 0_{1\times3} & 0 & c \end{bmatrix}}^{G} \overbrace{\begin{bmatrix} (\eta_v)_{3\times1} \\ \eta_t \\ \eta_{\delta t} \end{bmatrix}}^{w}. \qquad (4.6)
$$

The corresponding process noise matrix is thus written as

$$
Q(t) = \begin{bmatrix} (q_v)_{3x3} & 0 & 0 \\ 0_{1x3} & q_t & 0 \\ 0_{1x3} & 0 & q_{\delta t} \end{bmatrix}. \qquad (4.7)
$$

The discrete transition matrix ($\Phi_{k,k+1}$) and process noise matrix (Q_k) are formed by using Equations 3.4 and 3.5, respectively.

4.2.2 Measurement Model

The pseudorange (ρ) and Doppler ($\dot{\phi}$) measurements are related to the satellite and antenna positions and velocities by

$$\rho = \sqrt{(r_{s,x} - r_x)^2 + (r_{s,y} - r_y)^2 + (r_{s,z} - r_z)^2} + ct \qquad (4.8)$$

$$\dot{\phi} = \frac{(r_{s,x} - r_x)(v_{s,x} - v_x) + (r_{s,y} - r_y)(v_{s,y} - v_y) + (r_{s,z} - r_z)(v_{s,z} - v_z)}{\rho} + c\delta\dot{t} \qquad (4.9)$$

respectively where,

$r_{\bullet}$: represents the position of the antenna in a given direction,

$v_{\bullet}$: represents the velocity of the antenna in a given direction,

$\bullet_{s,\bullet}$: represents either the position or the velocity of the satellite.

Note that the measurements are not linear functions of the parameters. As discussed in the previous section, since the measurement model is non-linear, a linearized filter must be used. As such, the linearized design matrices are a function of the measurements and the estimated parameters:

$$H(\rho) = \begin{bmatrix} \frac{\delta\rho^1}{\delta r_x} & \frac{\delta\rho^1}{\delta r_y} & \frac{\delta\rho^1}{\delta r_z} & 0 & 0 & 0 & 1 & 0 \\ \vdots & \vdots & \vdots & \vdots & \vdots & \vdots & \vdots & \vdots \\ \frac{\delta\rho^N}{\delta r_x} & \frac{\delta\rho^N}{\delta r_y} & \frac{\delta\rho^N}{\delta r_z} & 0 & 0 & 0 & 1 & 0 \end{bmatrix}_{N\times 8} \qquad (4.10)$$

$$H(\dot{\phi}) = \begin{bmatrix} \frac{\delta\dot{\phi}^1}{\delta r_x} & \frac{\delta\dot{\phi}^1}{\delta r_y} & \frac{\delta\dot{\phi}^1}{\delta r_z} & \frac{\delta\dot{\phi}^1}{\delta v_x} & \frac{\delta\dot{\phi}^1}{\delta v_y} & \frac{\delta\dot{\phi}^1}{\delta v_z} & 0 & 1 \\ \vdots & \vdots & \vdots & \vdots & \vdots & \vdots & \vdots & \vdots \\ \frac{\delta\dot{\phi}^N}{\delta r_x} & \frac{\delta\dot{\phi}^N}{\delta r_y} & \frac{\delta\dot{\phi}^N}{\delta r_z} & \frac{\delta\dot{\phi}^N}{\delta v_x} & \frac{\delta\dot{\phi}^N}{\delta v_y} & \frac{\delta\dot{\phi}^N}{\delta v_z} & 0 & 1 \end{bmatrix}_{N\times 8} \qquad (4.11)$$

where,

$\left.\frac{\delta}{\delta r_{\bullet}}\right|_{\hat{x}_{k-1}^{(+)}}$: represents the partial derivative with respect to the position error, evaluated at the last estimated position and velocity,

$\left.\frac{\delta}{\delta v_{\bullet}}\right|_{\hat{x}_{k-1}^{(+)}}$: represents the partial derivative with respect to the velocity error,

evaluated at the last estimated position and velocity,

N : is the number of satellites providing measurements.

Combining Equations 4.10 and 4.11 thus gives the following final linearized design matrix:

$$H = \begin{bmatrix} H(\rho) \\ H(\dot{\phi}) \end{bmatrix}_{2N \times 8} \tag{4.12}$$

and the measurement misclosures are thus given as follows:

$$\delta z = \begin{bmatrix} \rho \\ \dot{\phi} \end{bmatrix}_{2N \times 8} - \begin{bmatrix} \tilde{\rho} \\ \tilde{\dot{\phi}} \end{bmatrix}_{2N \times 8} \tag{4.13}$$

where the pseudorange (ρ) and Doppler ($\dot{\phi}$) are single-point measurements and $\tilde{\bullet}$ is a predicted measurement computed using the predicted filter model.

The next important consideration is the formation of the measurement noise, or measurement variance-covariance matrix. Effectively, this matrix provides an estimate of the accuracy of the measurements being used. These values are often supplied by manufacturers or derived through calibration.

It is typically assumed that the measurements made by a GPS receiver are uncorrelated and thus the off-diagonal elements of the measurement noise matrix are zero. The diagonal elements of this matrix typically reflect the variance of the pseudoranges. However, there are other considerations that affect the estimated measurement variance.

Petovello (2003) provides a methodology for differentially weighting the satellite measurements based on their elevation angle (e) relative to the antenna's horizon. As satellites are positioned at lower elevation angles, the amount of ionospheric and tropospheric disturbance is increased and thus the measurements from those satellites should be considered less accurate. The computation of the modified standard deviation values is given by (Petovello 2003)

$$\sigma_\rho^* = \frac{1}{\sin e} \cdot \sigma_\rho. \tag{4.14}$$

4.3   INS Error Filter

The INS mechanization procedure discussed in Section 2.3.1 is used to process the raw IMU measurements to give position, velocity and attitude in the ECEF frame. However, mechanization is dependant on accurate measurements as input. There is no mathematical procedure within mechanization to mitigate faulty observables or characterize sensor errors. For this, the INS filter must estimate the INS error parameters.

4.3.1   System Model

Typically, an INS filter has nine navigation parameters: three for position errors, three for velocity errors and three for attitude errors. However, with low cost inertial devices the sensor errors are deterministic and can be estimated alongside the navigation error parameters in the parameter space.

Navigation Error States

The behaviour of the inertial navigation error parameters is defined by the perturbation of the mechanization equations. The algorithm for this perturbation analysis is well documented (Jekeli 2001, El-Sheimy 2007), and is therefore not reiterated here. The resultant error model can be stated in the series of differential equations, as follows:

$$
\begin{aligned}
\delta \dot{r}^e &= \delta v^e \\
\delta \dot{v}^e &= N^e \delta r^e - 2\Omega_{ie}^e \delta v^e - F^e \epsilon^e + R_b^e \delta f^b \\
\dot{\epsilon} &= -\Omega_{ie}^e \epsilon^e + R_b^e \delta w^b
\end{aligned}
\tag{4.15}
$$

where,

δr^e : is the position error vector in the ECEF frame (δr_x^e, δr_y^e, δr_z^e),

δv^e : is the velocity error vector in the ECEF frame (δv_x^e, δv_y^e, δv_z^e),

F^e : is the skew-symmetric matrix representing the specific force,

ϵ^e : is the misalignment error vector (ϵ_x^e, ϵ_y^e, ϵ_z^e),

N^e : is a tensor of the gravitational gradients,

Ω_{ie}^e : is the skew-symmetric matrix of the Earth's angular velocity with respect to the inertial frame,

R_b^e : is the rotation matrix from the body frame to the ECEF frame,

δf^b : is the accelerometer sensor error vector, (δf_x^b, δf_y^b, δf_z^b),

$\delta \omega^b$: is the gyroscope sensor error vector, ($\delta \omega_x^b$, $\delta \omega_y^b$, $\delta \omega_z^b$).

Inertial Sensor Error States

The inertial sensor measurement model was given previously by Equations 2.31 and 2.32. With high-end inertial devices the sensor biases, scale factors and non-orthogonality errors are negligible (Godha 2006) and thus the only sensor errors represented in the filter are bias-drift (δb) and noise (η). In this case, Equations 2.31 and 2.32 can be simplified to

$$\delta f = \tilde{f} - f = \delta b_a + \eta_a$$
$$\delta \omega = \tilde{\omega} - \omega = \delta b_g + \eta_g. \tag{4.16}$$

The bias drift in the INS sensor is therefore modelled as a first-order Gauss-Markov process as follows:

$$\delta \dot{b}_a = -\frac{1}{\tau_a} \delta b_a + \eta_{b_a}$$
$$\delta \dot{b}_g = -\frac{1}{\tau_g} \delta b_g + \eta_{b_g} \tag{4.17}$$

where,

$\tau_\bullet$: is correlation time, and

$\eta_{b_\bullet}$: is the Gauss-Markov process driving noise.

These Gauss-Markov parameters are typically determined through laboratory calibration (Nassar 2003). The Gauss-Markov process driving noise's standard deviation is computed using Equation 4.18 as follows:

$$q_{b_\bullet} = \sqrt{\frac{2\sigma^2}{\tau_\bullet}}$$

(4.18)

where σ^2 is the Gauss-Markov temporal variance (El-Sheimy 2007).

Equations 4.15 and 4.17 comprise the process model for what is called the *15 state filter*, which is shown in its entirety in equation 4.19. Represented here are nine navigation error parameters and six sensor error parameters.

$$
\overbrace{\begin{bmatrix} \delta\dot{r}^e \\ \delta\dot{v}^e \\ \dot{\epsilon} \\ \delta\dot{b}_a \\ \delta\dot{b}_g \end{bmatrix}}^{\dot{x}} = \overbrace{\begin{bmatrix} 0_{3\times3} & I_{3\times3} & 0_{3\times3} & 0_{3\times3} & 0_{3\times3} \\ N^e_{3\times3} & -2(\Omega^e_{ie})_{3\times3} & -F^e_{3\times3} & (R^e_b)_{3\times3} & 0_{3\times3} \\ 0_{3\times3} & 0_{3\times3} & -(\Omega^e_{ie})_{3\times3} & 0_{3\times3} & (R^e_b)_{3\times3} \\ 0_{3\times3} & 0_{3\times3} & 0_{3\times3} & (-1/\tau_a)_{3\times3} & 0_{3\times3} \\ 0_{3\times3} & 0_{3\times3} & 0_{3\times3} & 0_{3\times3} & (-1/\tau_g)_{3\times3} \end{bmatrix}}^{F} \overbrace{\begin{bmatrix} \delta r^e \\ \delta v^e \\ \epsilon \\ \delta b_a \\ \delta b_g \end{bmatrix}}^{x}
$$

$$
+ \overbrace{\begin{bmatrix} 0_{3\times3} & 0_{3\times3} & 0_{3\times3} & 0_{3\times3} \\ (R^e_b)_{3\times3} & 0_{3\times3} & 0_{3\times3} & 0_{3\times3} \\ 0_{3\times3} & (R^e_b)_{3\times3} & 0_{3\times3} & 0_{3\times3} \\ 0_{3\times3} & 0_{3\times3} & I_{3\times3} & 0_{3\times3} \\ 0_{3\times3} & 0_{3\times3} & 0_{3\times3} & I_{3\times3} \end{bmatrix}}^{G} \overbrace{\begin{bmatrix} \eta_a \\ \eta_g \\ \eta_{b_a} \\ \eta_{b_g} \end{bmatrix}}^{w}
$$

(4.19)

The process noise variance-covariance matrix ($Q(t)$) is given by

$$Q(t) = \begin{bmatrix} (q_a)_{3\times3} & 0_{3\times3} & 0_{3\times3} & 0_{3\times3} \\ 0_{3\times3} & (q_g)_{3\times3} & 0_{3\times3} & 0_{3\times3} \\ 0_{3\times3} & 0_{3\times3} & (q_{b_a})_{3\times3} & 0_{3\times3} \\ 0_{3\times3} & 0_{3\times3} & 0_{3\times3} & (q_{b_g})_{3\times3} \end{bmatrix}. \tag{4.20}$$

MEMS sensors have inherently high sensor errors due to low cost componentry and their small size. Table 1.2 shows the magnitude of the high turn on bias and first-order drift of the low-cost MEMS Crista IMU. Although these errors are deterministic in nature, the values from one usage to another can be highly variable. Moreover, calibration of the sensors before every usage is not feasible and so the error values are added to the filter process model and estimated along with the position, velocity and attitude values. The relationship of the IMU error parameters and the measurement errors are as follows (El-Sheimy 2007):

$$\tilde{f} = f S_a + b_a + \eta_a$$
$$\tilde{\omega} = \omega S_g + b_g + \eta_g \tag{4.21}$$

where,

f, ω : are the true specific acceleration and angular velocity,

$\tilde{f}, \tilde{\omega}$: are the measured acceleration and angular velocity,

$S_\bullet$: is the scale factor, and

$b_\bullet$: is sensor bias which is a combination of turn-on bias (b_{tob}) and bias drift (δb).

The sensor bias drift is modelled as a first-order Gauss-Markov process for both the accelerometers and the gyroscopes. The parameters for each sensor model were obtained through autocorrelation analysis conducted on static data that was collected in the lab.

Table 4.1: Sensor random noise spectral density and Gauss-Markov parameters for a Crista IMU

	Gyroscopes			*Accelerometers*		
	Noise	**Gauss-Markov**		**Noise**	**Gauss-Markov**	
	$(°/h/\sqrt{Hz})$	$\sigma(°/h)$	$\tau(s)$	$(m/s^2/\sqrt{Hz})$	$\sigma(m/s^2)$	$\tau(s)$
X	3610	7000	3000	0.026	0.12	4100
Y	3610	7000	3000	0.026	0.12	4100
Z	3610	7000	3000	0.026	0.12	4100

For this calibration, 16 h of data was collected. A correlation time was set to 5 min with an accuracy of 10%. The resultant Gauss-Markov parameters are shown in Table 4.1. These values are an average of the nine sensor models that were computed during the lab calibration. The mean values were used initially to start the filter and then were modified in subsequent processing to give appropriate predicted position variance numbers. This heuristic approach was time consuming and provides an area of potential research to solve the problem.

The sensor turn-on bias remained consistent for any given run and was therefore modelled as a random constant process. They are listed in Table 4.2.

During the lab calibration it was also determined that the scale factors (S) changed slowly over time, and as such they are also modelled as first-order Gauss-Markov processes (El-Sheimy 2007). This is represented mathematically as follows:

$$\dot{S}_a = -\frac{S_a}{\tau_{S_a}} + \eta_{S_a}$$
$$\dot{S}_g = -\frac{S_g}{\tau_{S_g}} + \eta_{S_g}.$$

(4.22)

Refer to Table 4.2 for the scale factor model parameter values.

With the addition of the twelve error parameters to the process model for low-cost MEMS IMUs, the new filter is called a *27 state filter*. This filter consists of the nine navigation error parameters as well as eighteen sensor error parameters. Equation 4.19 must therefore be augmented with the inertial sensor errors as follows:

Table 4.2: Turn-on bias and scale factor model parameters for a Crista IMU

| | *Gyroscopes* | | | *Accelerometers* | | |
| | Turn-on bias | Scale factor | | Turn-on bias | Scale factor | |
	$\sigma(°/h)$	$\sigma_{S_g}(ppm)$	$\tau_{S_g}(s)$	$\sigma(m/s^2)$	$\sigma_{S_g}(ppm)$	$\tau_{S_g}(s)$
X	1800	100000	18000	0.480	100000	18000
Y	1800	100000	18000	0.480	100000	18000
Z	1800	100000	18000	0.480	100000	18000

$$
\overbrace{\begin{bmatrix} \dot{b}_{a,tob} \\ \dot{b}_{g,tob} \\ \dot{S}_a \\ \dot{S}_g \end{bmatrix}}^{\dot{x}} = \overbrace{\begin{bmatrix} 0_{3\times3} & 0_{3\times3} & 0_{3\times3} & 0_{3\times3} \\ 0_{3\times3} & 0_{3\times3} & 0_{3\times3} & 0_{3\times3} \\ 0_{3\times3} & 0_{3\times3} & (-1/\tau_a)_{3\times3} & 0_{3\times3} \\ 0_{3\times3} & 0_{3\times3} & 0_{3\times3} & (-1/\tau_a)_{3\times3} \end{bmatrix}}^{F} \overbrace{\begin{bmatrix} \delta b_{a,tob} \\ \delta b_{g,tob} \\ S_a \\ S_g \end{bmatrix}}^{x}
$$

$$
+ \overbrace{\begin{bmatrix} 0_{3\times3} & 0_{3\times3} \\ I_{3\times3} & 0_{3\times3} \\ 0_{3\times3} & I_{3\times3} \\ 0_{3\times3} & 0_{3\times3} \end{bmatrix}}^{G} \overbrace{\begin{bmatrix} \eta_{S_a} \\ \eta_{S_g} \end{bmatrix}}^{w} \tag{4.23}
$$

As well, the process noise variance-covariance matrix shown in Equation 4.20 must be augmented with

$$
Q(t) = \begin{bmatrix} (q_{S_a})_{3\times3} & 0_{3\times3} \\ 0_{3\times3} & (q_{S_g})_{3\times3} \end{bmatrix}. \tag{4.24}
$$

The discrete process noise matrix and the corresponding transition matrix is obtained through Equations 3.4 and 3.5, respectively.

Aiding Sensor Error States

Since the filter in a tightly coupled integration scheme is centralized, it must account for INS *and* GPS error parameters in the same filter (Petovello 2003). Since the position

and velocity error parameters are common to both GPS and INS filters, these values do not need to be duplicated (see Equations 4.6 and 4.19). This leaves only the receiver clock error parameters (t and δt) to be added to the INS process model.

An unfortunate consequence of the addition of these two parameters is that the *15-state filter* and the *27-state filter* include 17 and 29 parameters, respectively. As per convention, these filters are still called 15-state and 27-state filters, although it remains a point of confusion. In this case, GPS is considered an *aiding source* to the INS, and correspondingly, the GPS receiver clock error parameters are called *aiding source error states*. It should be noted that this is not the case for the loosely-coupled integration since it employs a decentralized architecture.

4.3.2 Measurement Model

The type of measurement model used for the INS filter is dependant on the integration strategy being used. The measurement models for the closed loop, tightly coupled algorithm is discussed here. For a discussion of loosely coupled and open loop implementations refer to Petovello (2003) and Godha (2006).

Tight Coupling

In the tightly coupled integration algorithm, the measurement model resembles that of the GPS-only filter (see Equations 4.10 to 4.13), with the notable exception being the linearization point. Whereas in the GPS-only filter, the predicted estimates of the position and velocity were used as the linearization point, the INS filter uses the position and velocity derived from the lever-arm-corrected IMU mechanization.

4.4 Modifications for Pedestrian Kinematics

The standard tightly coupled architecture must be modified somewhat in order to provide kinematics information and exploit the dynamics of the repeatable human gait. While
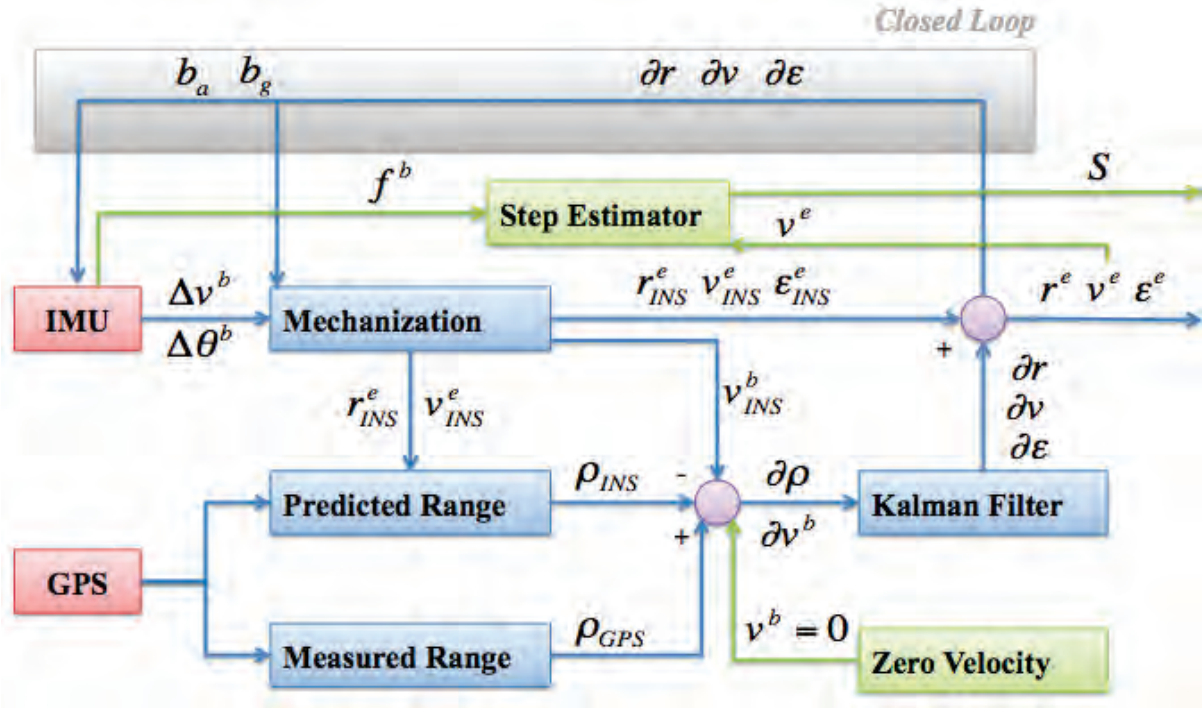
Figure 4.2: Tightly coupled GPS/INS algorithm step estimator as well as implementation of Zero Velocity Updates (ZUPTs).

the GPS/INS filter is able to produce all of the parameters that are needed for kinematics, it needs to be transformed to provide meaningful information. For instance, step length (SL) and step frequency (SF) are important metrics that are not direct outputs of the GPS/INS filter. In order to produce these values, steps must be detected and distinguished from one another.

The inputs for the step estimator in Figure 4.2 are the computed GPS/INS velocity (v^e) and the acceleration signal from the IMU (f^b). Therefore, the quality of the step estimator will depend on the quality of these two inputs.

A characteristic of gait dynamics that has proved valuable for the use of GPS/INS in pedestrian navigation is the repeatable and reliable application of Zero Velocity Updates (ZUPTs) while the foot is at rest on the ground. By knowing beforehand this aspect of the foot's dynamics, ZUPTs can be added to the filter to improve the performance (Godha 2006). Most importantly for this application, ZUPTs improve the quality of the

velocity input into the step estimator. Figure 4.2 shows how ZUPT's are implemented in relation to the GPS/INS filter.

4.4.1 Zero Velocity Updates

With low-cost inertial measurement devices, the position and velocity solutions can degrade rapidly because of the strong increase in the magnitude of the velocity error. In the presence of GPS, a position and velocity update is provided to control these errors (El-Sheimy 2007), however, satellite signals can often be obstructed or attenuated, and in the case of single-point GPS, the position accuracy can be limited.

Another alternative to GPS updates, is a zero-velocity update (ZUPT). In this scenario, the velocity errors are better estimated during periods when the INS body frame is known to have come to rest. In essence, when the body frame is not moving, any non-zero velocity measurement can be thought of as an error. From this, the error characterization of the inertial unit can be estimated and fed back to the mechanization equations for better inertial measurement accuracy. Figure 4.2 depicts the application of ZUPTs in the tightly coupled GPS/INS computation algorithm.

When a ZUPT epoch is detected, the difference between the inertial unit's measurement and zero-velocity condition are input into the Kalman filter. The measurement update equation can be written as

$$
\underbrace{\begin{bmatrix} v_{INS}^e - v_0^e \\ v_{INS}^n - v_0^n \\ v_{INS}^u - v_0^u \end{bmatrix}}_{\delta z} = \underbrace{\begin{bmatrix} \underbrace{0 \quad 0 \quad 0}_{position} & \underbrace{1 \quad 0 \quad 0}_{velocity} & \underbrace{0 \quad \ldots \quad 0}_{other states} \\ 0 \quad 0 \quad 0 & 0 \quad 1 \quad 0 & 0 \quad \ldots \quad 0 \\ 0 \quad 0 \quad 0 & 0 \quad 0 \quad 1 & 0 \quad \ldots \quad 0 \end{bmatrix}}_{H} \underbrace{\begin{bmatrix} \delta r^e \\ \delta v^e \\ \vdots \end{bmatrix}}_{\delta x} + \underbrace{\begin{bmatrix} \delta v^e \\ \delta v^n \\ \delta v^u \end{bmatrix}}_{\eta}. \tag{4.25}
$$

The use of ZUPTs in pedestrian navigation where the inertial sensor is mounted on the foot is particularly useful since the zero velocity condition can be applied in every

stance phase (Godha et al 2006, Kwakkel et al 2007, Kwakkel 2007). Since the foot is stationary for a few measurement epochs approximately every second, the navigation solution (i.e. position, velocity and attitude) are vastly improved (*ibid*).

Moreover, the use of ZUPTs can vastly improve the kinematic measurements as well. El-Sheimy (2007) shows that the velocity error dynamics are dependant on the inertial measurement errors. Equation 4.19 shown earlier describes how the INS error dynamics were related the estimated parameters. The relationship between the velocity error dynamics and the attitude parameters can be shown as

$$
\overbrace{\begin{bmatrix} \delta\dot{v}^e \\ \delta\dot{v}^n \\ \delta\dot{v}^v \end{bmatrix}}^{\dot{x}} = \overbrace{\begin{bmatrix} 0 & f^v & -f^n \\ -f^v & 0 & f^e \\ f^n & -f^e & 0 \end{bmatrix}}^{F} \overbrace{\begin{bmatrix} \delta\eta \\ \delta\xi \\ \delta\psi \end{bmatrix}}^{x} + \overbrace{\begin{bmatrix} \delta f^e \\ \delta f^n \\ \delta f^v \end{bmatrix}}^{w} \tag{4.26}
$$

where,

$\delta\dot{v}^\bullet$: are the velocity error dynamics,

$f^\bullet$: are the measured specific accelerations,

$\delta v^\bullet$: is the velocity error state,

$\delta f^\bullet$: is accelerometer sensor error, and

$\bullet^e, \bullet^n, \bullet^v$: denote east, north and vertical directions, respectively.

Of particular interest is that the relation between velocities in the north and east directions are related to the roll and pitch errors by the specific force measured in the vertical direction. Since gravity is included in the vertical specific force, the quantities are related by a factor of almost ten (i.e. $f^v \approx 9.81$ m/s^2). Effectively, this means that by accurately estimating the errors in the velocity, not only are the velocity estimates improved, but so are the accuracy of the computed roll and pitch. This is an important consideration when using inertial measurements for kinematic analysis.

4.4.2   Lever Arm Compensation

In the coming chapters, the placement of the GPS and inertial sensors is discussed. For this thesis, the antenna was placed on the top of the test subjects' head to maximize satellite visibility while the IMUs were placed on the various segments of the lower limb. The concern with this setup is that the point of linearization is the IMU mechanized position, while the GPS ranges are measured to the phase centre of the antenna. The offset between these two sensors could potentially introduce errors, or worse, cause instability in the GPS/INS filter. The solution to the problem is to resolve the lever arm between the two sensors to within an acceptable proximity.

Figure 4.3 shows the lever arm between the forefoot-mounted IMU and the GPS antenna. The estimation of the lever arm is complicated by the fact that the IMU is constantly in motion relative to the antenna. However, since the pseudorange measurements themselves have a predictable level of noise (0.5 m under nominal conditions), the lever arm need only be resolved to within this envelope.

The lever arm in the case of the forefoot-mounted IMU is estimated as the height of the individual (i.e. the correction is entirely in the vertical direction). In effect, the horizontal component of the lever arm is ignored completely. These changes are absorbed by the parameters of the filter - most notably the position, and to a lesser extent, the velocity. The effects of this error will be explored in the coming chapters.

Future research may explore the improvement that is gained by estimating the lever arm, or using the roll and pitch angles to better translate the linearization point (i.e. the IMU mechanized position) to the antenna position. In such a case, the quality of the gyroscopes, or rather the limitations of the rotation information, will be paramount factors to consider.
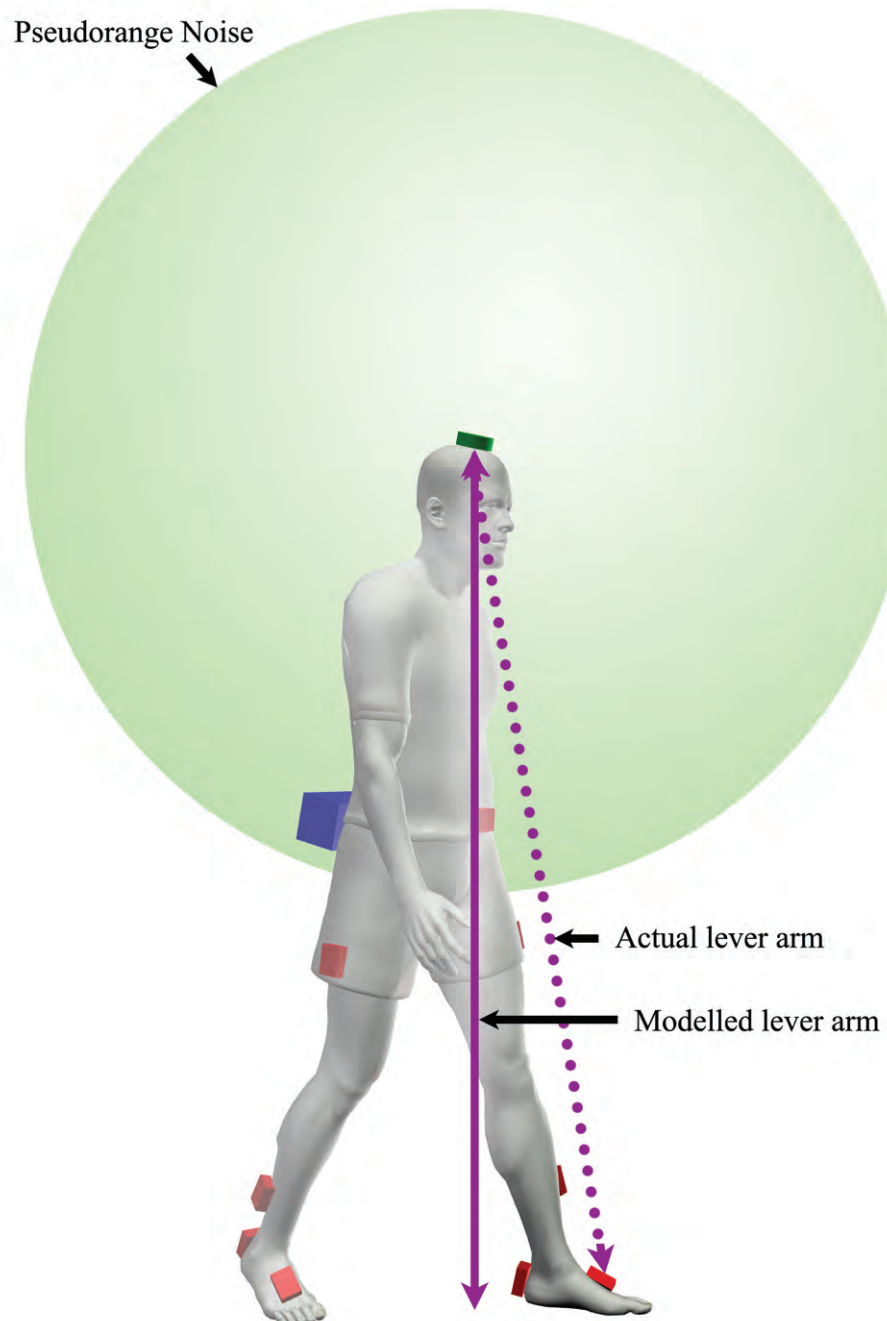
Figure 4.3: Lever arm compensation for the forefoot IMU within the normal pseudorange noise envelope.

4.5   Computations and Software

In order to implement lower limb kinematic analysis in software, each segment of the leg is abstracted as a single GPS/INS (see Figure 4.4). Each leg is represented by four separate segments and hence four GPS/INSs. In the following chapters the sensor placements are shown and described in detail.

Effectively, each segment of the lower limb was treated as a rigid member with a movable joint in between. The thigh, shank, rearfoot and forefoot were represented as separate GPS/INS systems. This allows the positions, velocities and attitudes of each member to be represented independently. By differencing the parameters of adjacent segments (i.e. the thigh and shank or the shank and rearfoot) the movement of the joints are observable.

In order to isolate the rotations of a joint, the rotations external to that joint must be removed. By subtracting the rotations experienced by the proximal segment's sensor from the distal segment's, only the rotations that are internal to the joint are extracted. For instance, by removing the rotations experienced by the thigh GPS/INS from the shank GPS/INS the rotations of the thigh, hip, and upper body are removed since they are experienced by both segments. What is left is the rotation that is experienced by the rotation in the joint.

The step estimator and ZUPTs are able to be applied in any of the GPS/INS systems. Figure 4.4 shows the step estimator as a component of the forefoot GPS/INS. While the step estimator could be applied to any segment, it will be shown in the next chapter that it performs best in the forefoot-mounted IMU case.

Each GPS/INS filter is run in a separate thread to optimize performance and ensure time synchrony. Since the measurements of adjacent systems must be differenced, each thread is held on the same epoch until all segments have returned results. This ensures data integrity and facilitates comparison of each threads results.
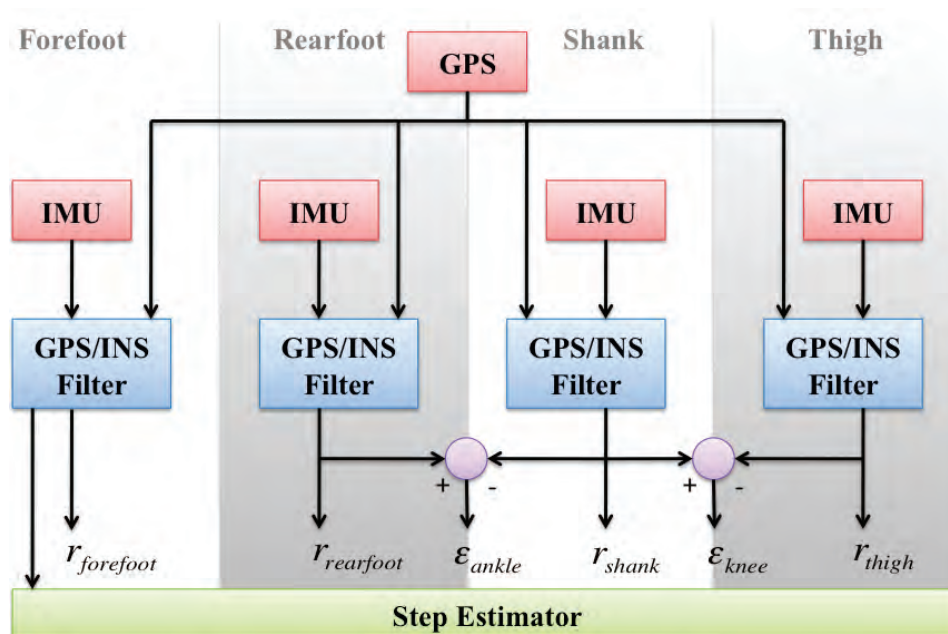
Figure 4.4: Software schema developed for the computation of lower limb kinematics.

The original pedestrian GPS/INS software was developed by Godha (2006), but was adapted to fit the current algorithm. The parallel processing, step detection and inter-thread computations were novel developments. Other changes made to the software, while numerous, are not worthy of mention. This software was used to process all data presented in this thesis.

Chapter 5

Pedestrian Navigation: Walking, Running and Sprinting

Pedestrian navigation encompasses a wide variety of gait scenarios. A pedestrian can walk, run or use any number of movements to traverse any given route. This chapter demonstrates the measurements of the proposed inertial navigation and kinematics algorithm for a walker and a runner.

Since the movements of the walking and running gaits are different, the algorithms are analyzed and contrasted with respect to parameters and performance. The results shown here were collected from a series of tests conducted in the Summer of 2008, around the University of Calgary in open sky conditions.

5.1 Field Test Description

In the first test, the author walked a prescribed route ($\sim 6.4\ km$) starting and ending at the CCIT building at the University of Calgary. The next test was conducted over the same course, except the subject was required to run at a comfortable speed. The results of both tests are discussed in this chapter.

5.1.1 Sensors and Equipment

The author was outfitted with nine Crista IMUs from CloudCap Technologies Inc. (see Figure 5.1). This IMU was designed to optimize both price and performance in GPS/INS integrated systems. It is a six axis measurement system consisting of three MEMS gyroscopic rate sensors and three accelerometers providing temperature compensated inertial data at a data rate of 100 Hertz. It has a built-in pulse-per-second (PPS) interface which facilitates the accurate time synchronization of the IMU and GPS data.
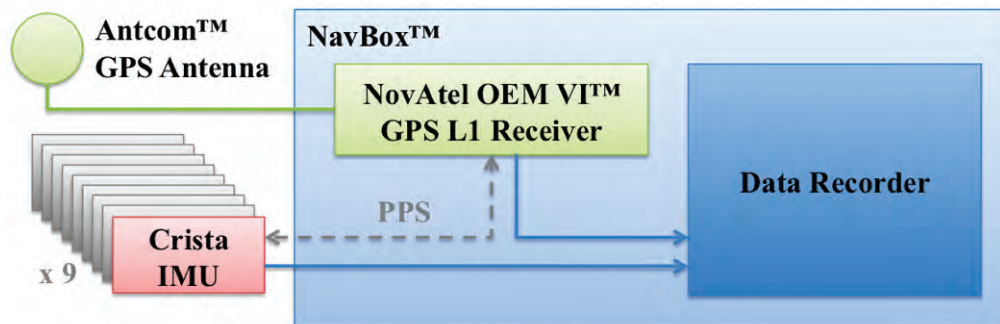
(a) Sensor schema
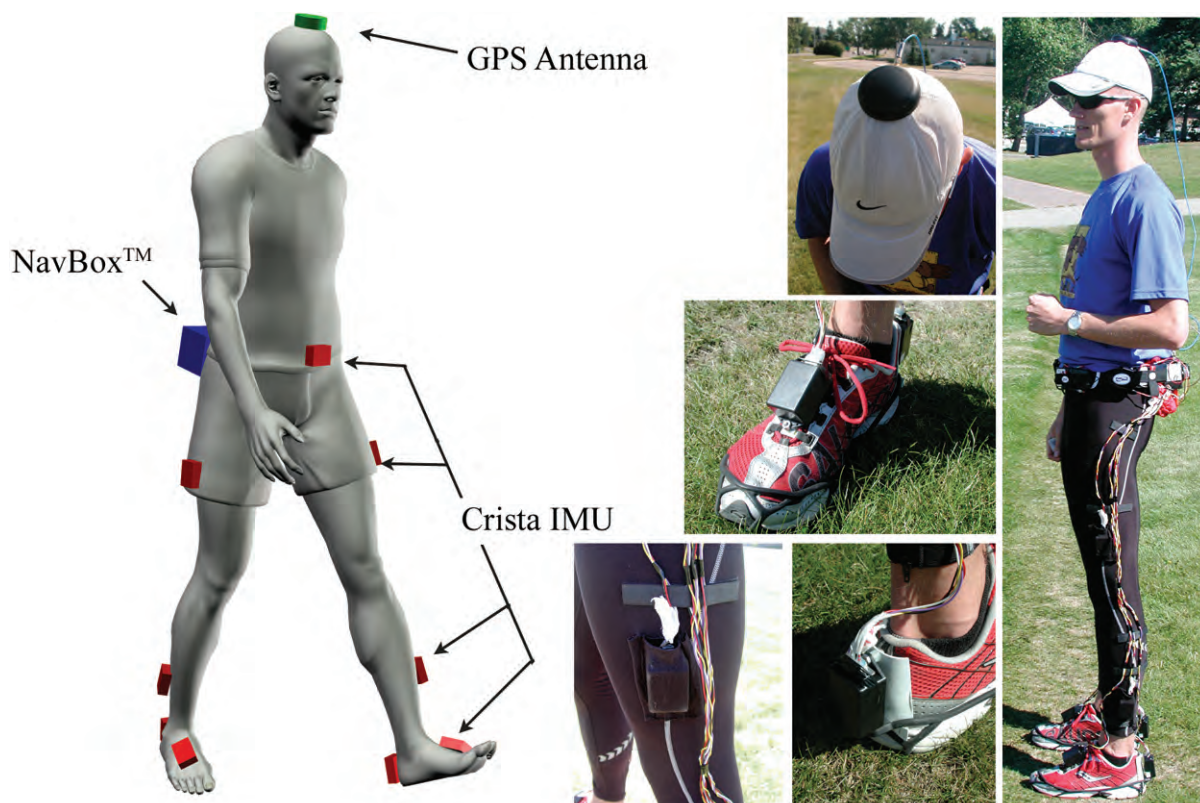
(b) Sensor placement

Figure 5.1: NavBox^{TM} with Antcom antenna and Crista IMUs. (a) Sensor schema. (b) Sensor placement. (inset) photos of walking experiment outside of CCIT building at the University of Calgary.

The dynamic range of the Crista IMU gyroscopes is ±900 °/s and $\pm10g$ for the accelerometer. The maximum acceleration recorded in this thesis was approximately 9.3g and 876 °/s for the rotation rate. Both values were recorded while the test subject was running, thus the Crista IMU was sufficient for this purpose.The dimensions of each Crista IMU unit is 2.05" x 1.50" x 1.00" and weighs 36.8 grams.

The author was also outfitted with an Antcom GPS antenna (Model: 2DG1215A-MNS-4) which was affixed to a ball cap to provide maximum satellite visibility. The antenna was also connected to a NovAtel OEM VI L1 GPS receiver which was able to log code range observations at a rate of 20 Hertz. The NovAtel OEM VI receiver was also able to provide a PPS signal that was output to all of the Crista IMUs to facilitate data synchronization.

The NovAtel OEM VI receiver was housed in a custom, belt-mounted data logging device called the NavBox^{TM} developed by the PLAN Group. Figure 5.1a shows the architecture of the NavBox, and Figure 5.1b shows the placement of the NavBox as well as the Crista IMUs and the Antcom antenna on the author.

5.1.2   Walk and Run Test Description

The test route was selected to include both uphill and downhill sections as well as a series of gradual and sharp turns to test the navigation solution of the GPS/INS solution. The different sections were also interesting from a kinematics perspective as they show the differences in gait as a result of the terrain's grade. The total distance travelled was 6.39 kilometres.

Figure 5.2 depicts various areas along the route. For the most part, there were open sky conditions, however in some instances satellite visibility was occluded by foliage or buildings. In effect, the route chosen reflects a typical sub-urban environment with changing skylines and partial and complete satellite occlusions. These conditions reflect the typical intended arena for the kinematic/navigation methodology. Since the test

Figure 5.2: Pictures of the suburban area in which the test was conducted.

subject is not restricted to the laboratory, measurements can be taken in a variety of environments.

5.2 GPS/INS Navigation Solution

One of the benefits of combining kinematic and navigation data together is the ability to correlate kinematic information with the kinds of terrain that the subject is exposed to while they walk or run. For instance, how does a person's knee flexion differ when they walk down a hill versus when they are on flat ground? How does it differ going uphill? What about ankle flexion?

(a)

(b)
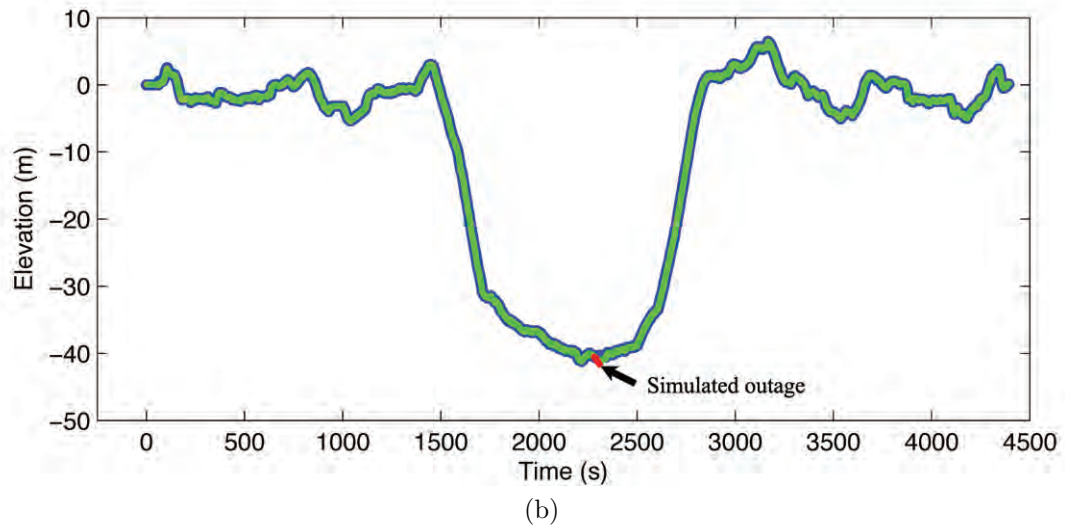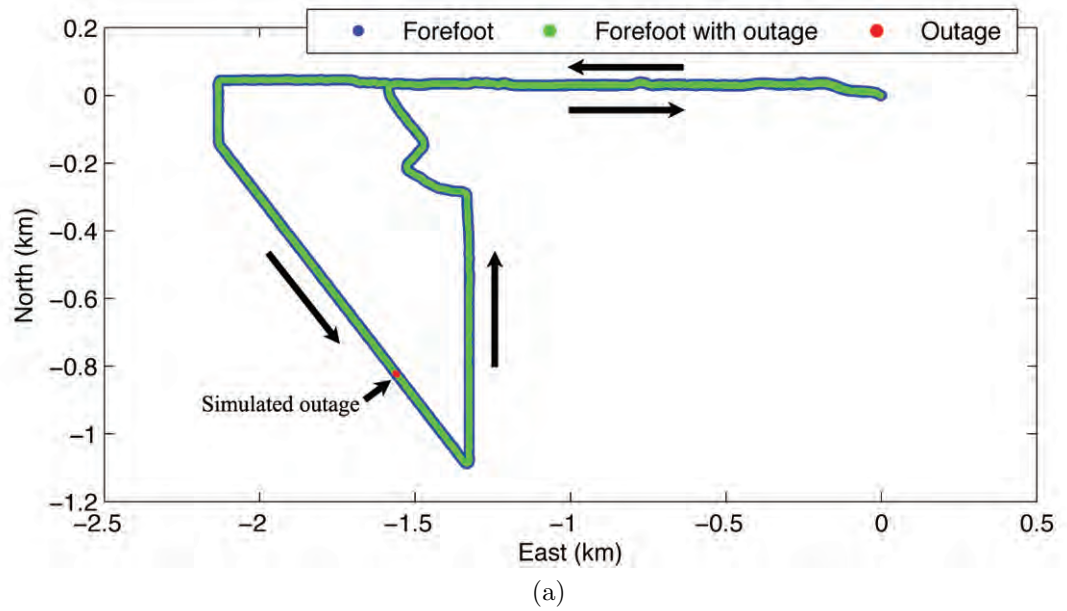
Figure 5.3: Planimetric and elevation trajectory of the test subject as calculated from the forefoot GPS/INS. Simulated 30 s satellite outage shown at 2400 seconds.

Before this GPS/INS methodology was proposed, these were painstaking questions because they involved elaborate setups to provide the answers. Treadmills mounted on platforms that were controlled by hydraulics have been used to show the effects of different grades on human walking (Lay et al 2006). While the results were informative, the cost and overhead to perform such experiments are prohibitive. It is much simpler if the experiments are performed outside, on real terrain. Moreover, the subjects could be measured on a variety of environments and conditions.

Figure 5.3 shows the planimetric and elevation trajectories of the test subject's path during the walking portion of this experiment. The accuracy of such trajectories have been well quantified before (Godha et al 2006), and therefore will not be analyzed here.

The navigation solution will be used to isolate areas of interest. For example, in this chapter, the question posed is, what are the kinematics of the lower limb on uphill, downhill and flat ground terrains, and more importantly, how do they differ?

Another important point to consider is the performance of the system in the absence of GPS measurements. In everyday tasks, the sky is often obscured or occluded by various structures such as trees and buildings. Other scenarios result in partial loss of sky visibility. In these cases, it is important to know the impact on the measurement reliability. For this reason, a simulated 30 s satellite outage was conducted at the 2400 s mark of the trajectory. Figure 5.3 shows the navigation solution with and without this outage. The results of both scenarios are analyzed later in this chapter to gain insight into the measurements' reliability.

First, the walking and running gait must be analyzed with respect to the measurements that are available. The accelerations and rotations of the segments of the lower limb are used to separate the repeatable units of gait, namely, the steps. Detecting steps is crucial for the kinematic analysis of walking and running since it allows for the comparison of one step and the next. In this algorithm, it is also important because of the

application of ZUPTs while the foot is stationary on the ground. The performance of the step detection algorithms is thus crucial for this technology and is presented here.

5.3 Gait Parameters

There are many metrics that are important when analyzing the human gait. From a navigation standpoint, the step length and direction are of vital importance. Other factors such as the distance travelled and speed are also interesting. From the kinesiologist's point of view, qualifying the different phases of the gait cycle, and quantifying cadence and walk ratios are of interest. The following section deals with these parameters and explains how each was determined using the measurements that were given by the accelerometers, gyroscopes and GPS receiver.

5.3.1 Phases of the Gait Cycle

Foot-mounted accelerometers are particularly efficient for detecting the four phases of the gait cycle, namely (1) *push-off* - where the heel lifts and weight is transferred onto the toe, (2) *swing* - where the foot is in the air, (3) *heel strike* - where the foot comes into contact with the ground again, and (4) *stance* - where the entire foot is in contact with the ground (Willemsen & Bloemhof 1990, Godha et al 2006, Kwakkel et al 2007). Figures 5.5 and 5.7 depict the gait cycle and the corresponding forefoot-mounted accelerometer signal for a walking and running gait, respectively. Table 5.1 shows the durations of the different phases the gait cycles for walking and running gaits for the author during this test. These results were acquired by averaging 30 steps on flat ground along the walk and run trajectories, respectively.

Immediately, it is apparent that the gait cycle of a runner is shorter than that of a walker, and that the profile of the gait cycle is significantly different. In the walking gait, the push-off and swing phases are mirrored by the heel strike and stance phases.
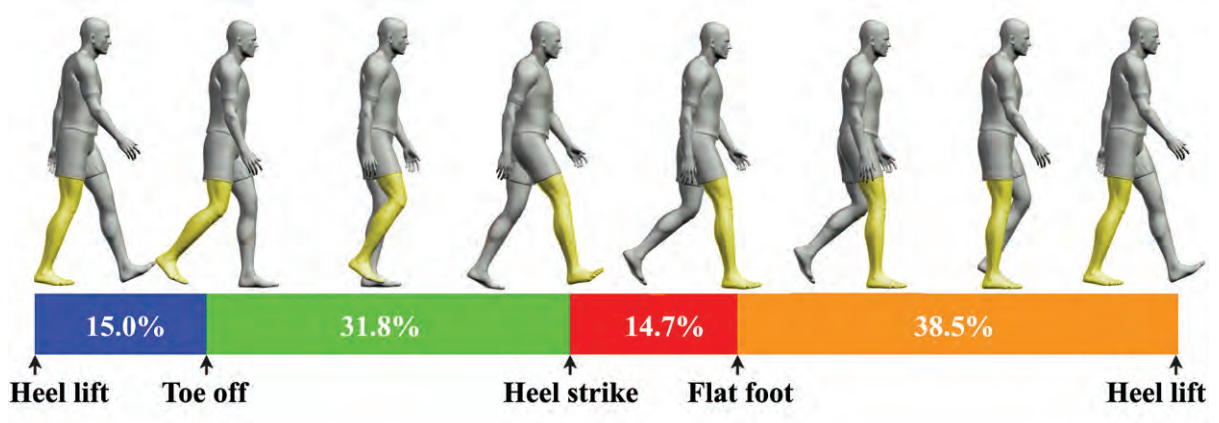
Figure 5.4: The walking gait cycle broken into phases; (blue) push-off, (green) swing, (red) heel strike, and (orange) stance.

While one leg is in the push-off phase, the other is in heel strike phase, and while one is in swing phase the other is in stance phase. This symmetry in the walking gait shows the rhythmical transfer of weight between the two limbs. Conversely, during the running gait this symmetry does not exist. Instead, both legs can be in the swing phase at the same time, and heel strike occurs while the other leg is still in the air. When running, the foot pushes off for a much longer period of time, reflecting the longer stride that is observable in most runners (see Table 5.1).

From Figures 5.5 and 5.7 , the push-off phase of the gait cycle is determined from a sharp increase in the acceleration, and occurs immediately after the flat acceleration of the previous step's stance phase. This drastic change in the acceleration is helpful in determining the beginning of the gait cycle, as will be shown in the next section.

Table 5.1: Typical durations of the phases of the gait cycle

Phase	Walk [s]	Run [s]
Push-off	0.20	0.34
Swing	0.37	0.22
Heel strike	0.18	0.09
Stance	0.47	0.13
Total	1.22	0.71
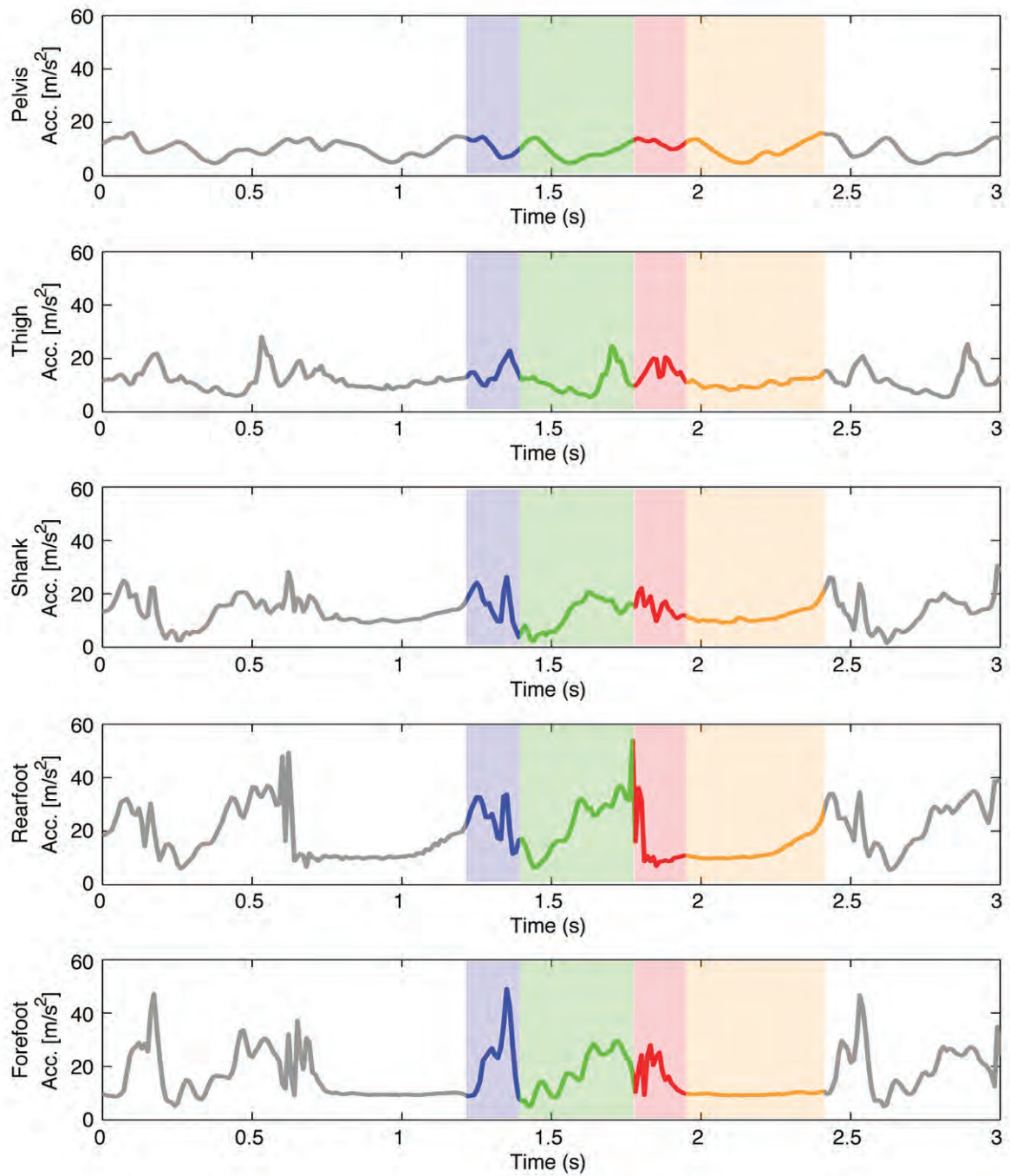
Figure 5.5: The phases of the step during walking can be determined by the accelerometer pattern. The forefoot sensor is best suited for determining gait phases.
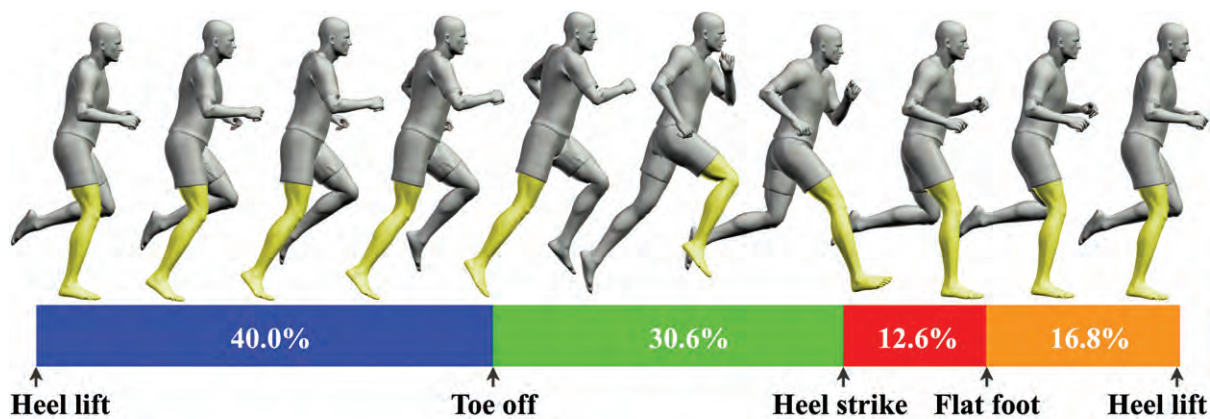
Figure 5.6: The running gait cycle can be broken into phases; (blue) push-off, (green) swing, (red) heel strike, and (orange) stance.

The next phase of the gait cycle, the swing phase, is characterized by a gradual increase in acceleration until it is abruptly halted by the heel contacting the ground. The acceleration of the forefoot can be more variable during the swing phase of the gait cycle since the foot is not in contact with the ground. However, the overall profile is most often the same: a slowly rising interval terminated by a sharp downwards trend. Godha et al (2006) shows that the slope of this portion of the gait cycle can be used to determine whether the subject is moving backwards or forwards. A negative slope indicates a forward moving individual and conversely, a positive slope indicates the subject is walking backwards.

The placement of the heel on the ground marks the transition from the swing to the heel strike phase of the gait cycle. Once the heel has hit the ground, the deceleration of the forefoot is very dramatic and characterized by large changes in the acceleration profile; both decreasing acceleration as the heel is stopped by the ground and increasing acceleration as the toe subsequently falls.

Finally, once the foot is entirely on the ground, the gait is said to be in the stance phase. This portion of the gait cycle is characterized by very little acceleration since the
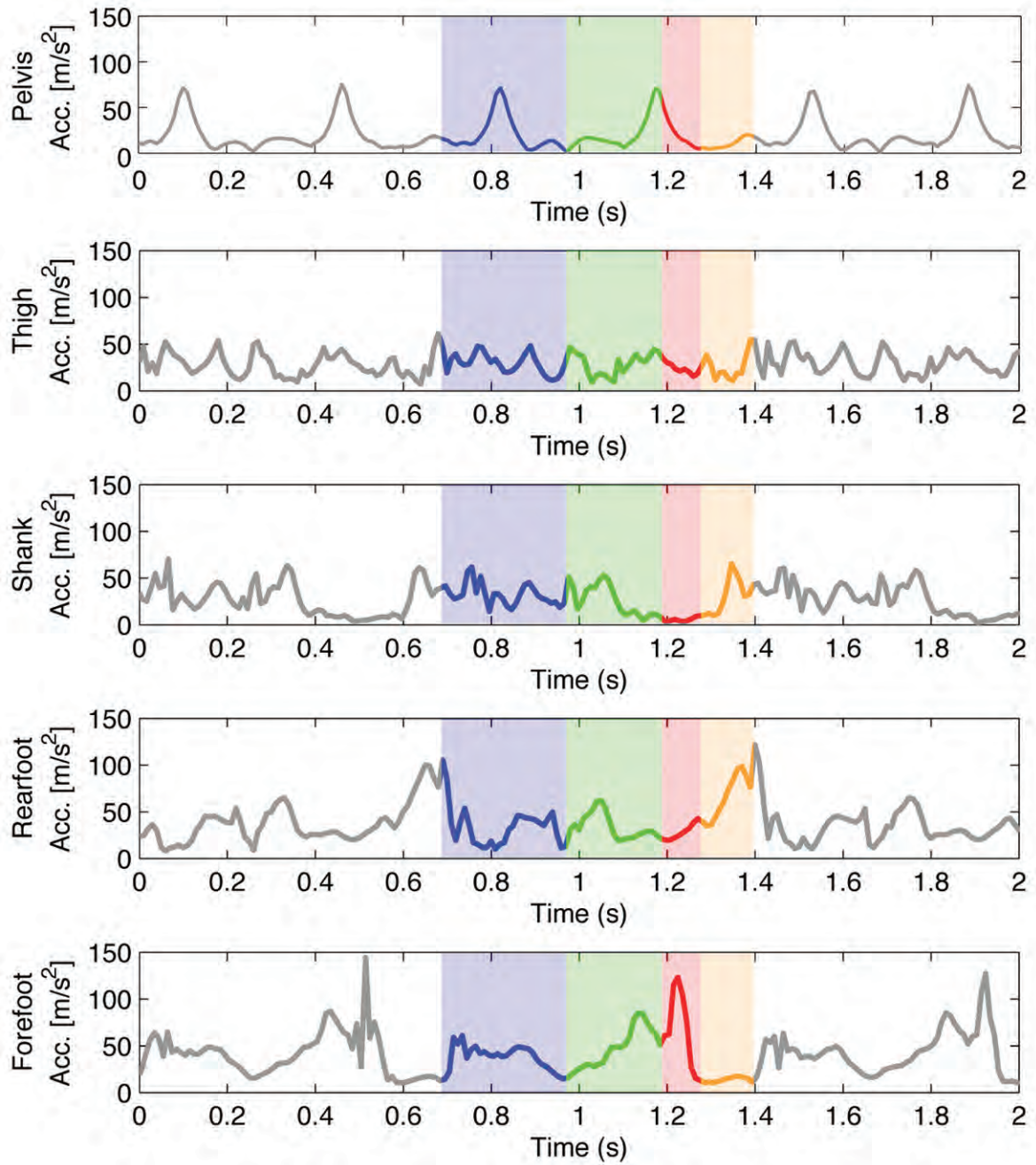
Figure 5.7: The phases of the step during running can be determined by the accelerometer pattern.

foot is essentially stationary. This portion will be shown to be important since the foot is in a zero-velocity condition, thus facilitating the application of ZUPTs. In Figure 5.7 the acceleration experienced during running shows more variability than in the walking gait. This will have important implications in the next sections related to stance phase and step detection.

5.3.2   Stance Phase Detection

In the last section, it was shown that the different phases of the gait cycle could be detected using the 3D acceleration signal. While it is easy to see these differences in the acceleration profile (see Figure 5.5), the question remains as to how to quantify the change from one phase to the next, and thereby allow an algorithm to detect which portion of the gait cycle the user is currently in. The process of detecting the stance phase on the gait cycle is particularly important for GPS/INS pedestrian navigation and kinematics since ZUPTs are applied only during the stance phase.

An automated algorithm for detecting the stance phase of the gait cycle has been shown successful in studies conducted in the past (Willemsen & Bloemhof 1990, Godha et al 2006, Kwakkel et al 2007). The variance of the acceleration signal is used to detect the period of zero acceleration that corresponds with the stance phase. Figure 5.8 depicts the 3D acceleration of the forefoot as well as the three-sample forward-moving variance. Also shown are the times at which ZUPTs were applied. Since the different phases of the gait cycle are delineated by sharp changes in acceleration, the moving variance of the acceleration signal can be used to detect changes in gait cycle. Moreover, during walking the stance phase is characterized by a period of very low variation compared with the other phases of the gait. Thus ZUPTs are applied when the three-sample variance reaches a sufficiently low threshold. In this case, the threshold was set between 1 and 1.5 $(m/s^2)^2$.

As expected, ZUPTs are applied to both the forefoot and the rearfoot at regular intervals during the stance phase. From Figure 5.8, the rearfoot experiences higher

dynamics during the latter portions stance phase and thus has fewer ZUPTs applied. The increased dynamics may be caused by the shape of the running shoe since they are often designed to lift the heel and make the forward movements of the foot easier. In any event, the extraneous dynamics are small in magnitude compared with the entire measurement volume and should have little effect on the overall performance of the system since multiple ZUPTs are still applied at regular intervals (approximately 4 ZUPTs/s).
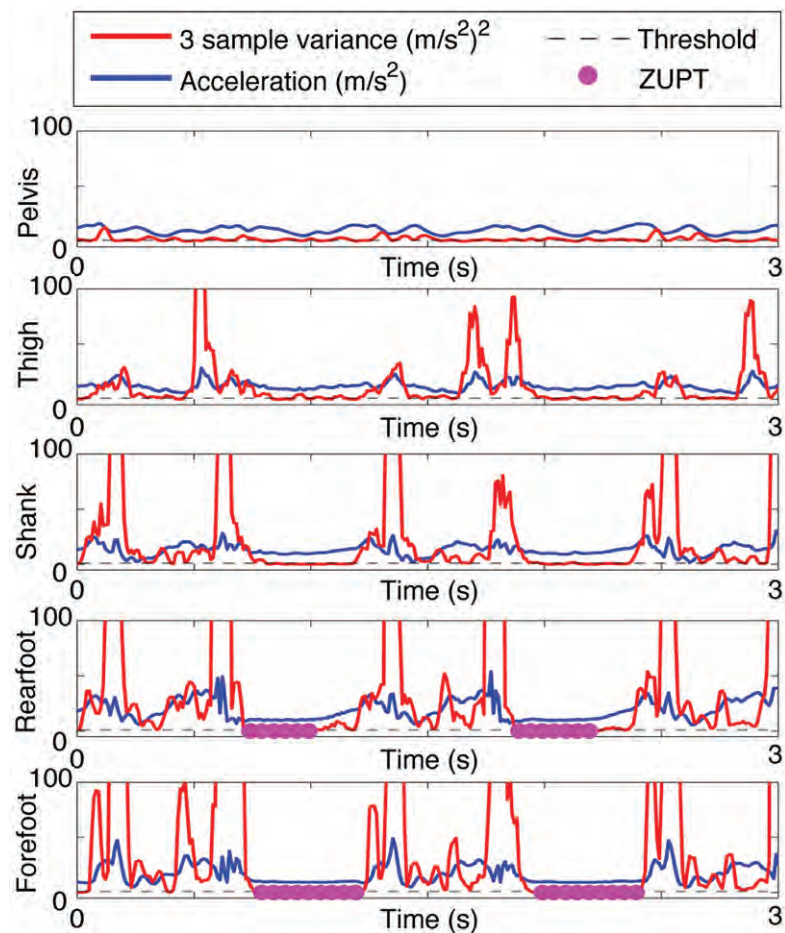
Figure 5.8: Zero Velocity Updates (ZUPTs) applied during walking using the variance of the accelerometer signal.

As expected, ZUPTs failed to be detected on the shank, thigh and pelvis-mounted sensors during the walking gait since these segments never come to rest during a normal walking gait cycle. In fact, ZUPTs were only applied to these sensors when the subject

comes to a full stop. The lack of ZUPTs for these measurements means that the sensor errors could potentially be unbounded, however as will be shown in the following section, this is not the case.

Thus far, the detection of the stance phase of the gait cycle and the application of ZUPTs has worked very well. However, the algorithm's limits are tested when applied to a running gait. Figure 5.9 shows the acceleration signal, 3 sample variance and applied ZUPTs during running. When compared to the walking scenario shown in Figure 5.8, the differences are obvious: fewer ZUPTs are applied during the running gait. In part, this is due to the shortened stance phase (130 ms vs 470 ms during walking). Since the foot is at rest for a shorter period of time, there will necessarily be fewer ZUPTs.

Another factor that results in the application of fewer ZUPTs during running is the higher dynamics experienced by the forefoot during the stance phase. The quicker transfer of weight onto the standing limb causes the foot to move during the stance phase and thus there are fewer moments where the foot is truly at rest.

Overall, the application of ZUPTs is successful for both walking and running gaits. The impact of ZUPTs on the navigation and kinematics measurements will be determined in upcoming sections. However, it is expected that the velocity misclosures are reduced by the application of ZUPTs which lead to more precise GPS/INS measurements.

5.3.3   Step Detection

In pedestrian navigation as well as in kinematics, it is important to know when the subject has taken a step. Step detection not only marks the beginning of the gait cycle, but also segments the subject's trajectory into discrete units. These units can be added together as in the case of navigation, or averaged over time in the case of kinematics.

In the previous sections, the phases of the gait cycle were identified and the stance phase was isolated in order to apply ZUPTs. In this section, the algorithm first proposed by Godha et al (2006) and later used by Kwakkel et al (2007) is tested for step detection
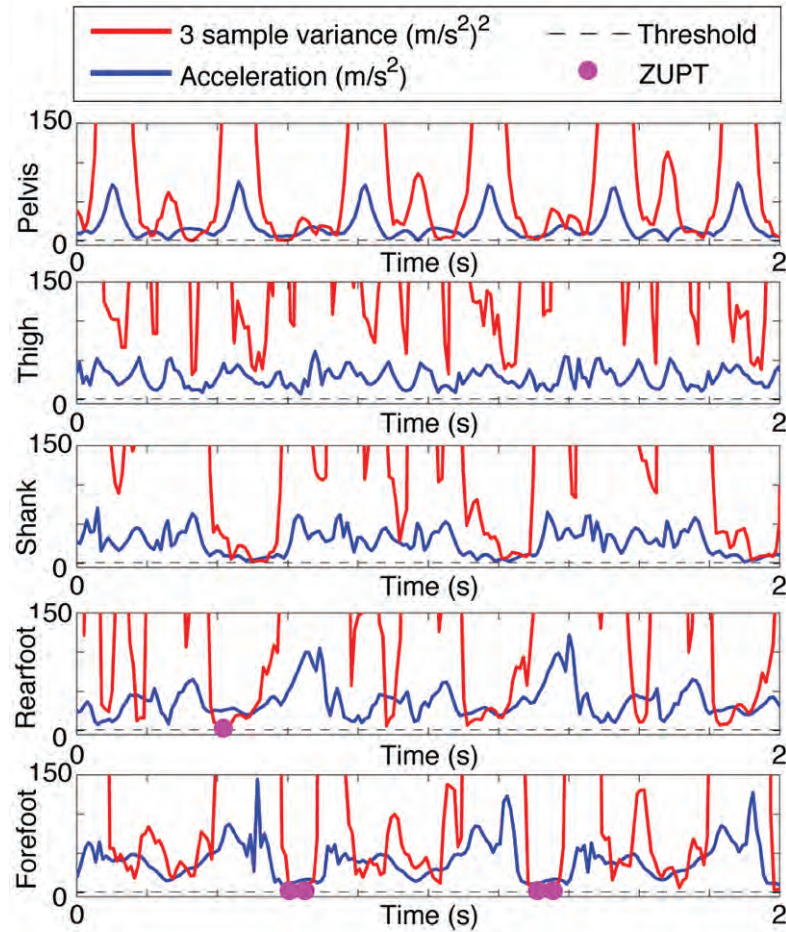
Figure 5.9: Zero Velocity Updates (ZUPTs) applied during running using the variance of the accelerometer signal.

for both walking and running gaits.

Figure 5.10 shows the acceleration of the forefoot as well as the forward-moving 30 sample variance for a subject walking with a regular gait. A step is detected when the moving variance moves above a threshold of 1 to 1.5 $(m/s^2)^2$, much like the stance phase detection algorithm discussed in the previous section.

Figure 5.10a shows that this algorithm is exceedingly good at detecting steps while the subject is moving with a regular walking gait. In this case, nearly every step was detected during the entire measurement volume. The literature shows that this step detection algorithm is greater than 99% accurate for walking individuals (Godha et al
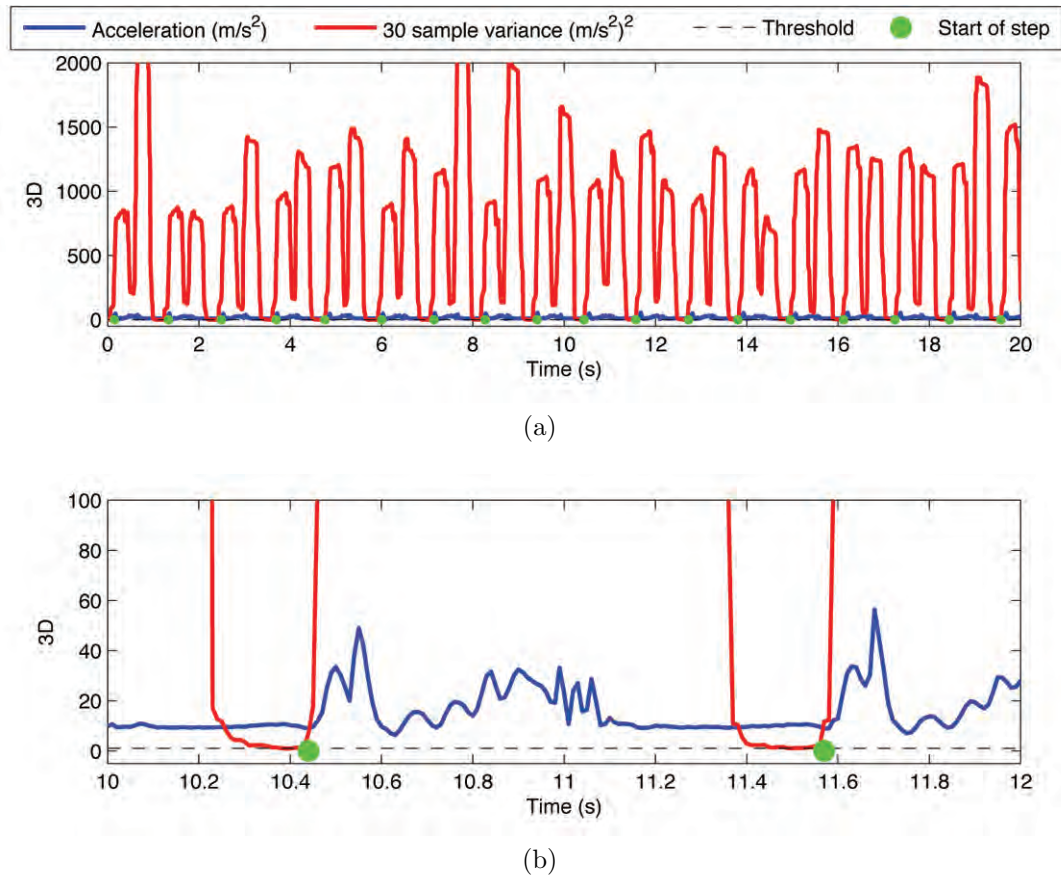
Figure 5.10: Step detection during walking using the variance of the forefoot accelerometer signal: (a) Steps are consistently detected using this method. (b) A magnified section of the above figure showing the exact point of step detection.

2006). This result was confirmed by this experiment.

The algorithm was designed particularly for forefoot-mounted IMUs. In fact, the step detection algorithm is far less robust for rearfoot-mounted IMUs as shown in Figure 5.11. The primary reason for the decreased performance can be attributed to the dynamics of the rearfoot. In contrast to the forefoot, the rearfoot IMU measures non-zero accelerations during stance phase. This increase in acceleration results in a less clearly defined transition between the stance phase and the push-off phase of the next gait cycle. Hence, the step detection algorithm becomes less effective.

Since the variance of the stance phase is higher on the rearfoot, the threshold needed
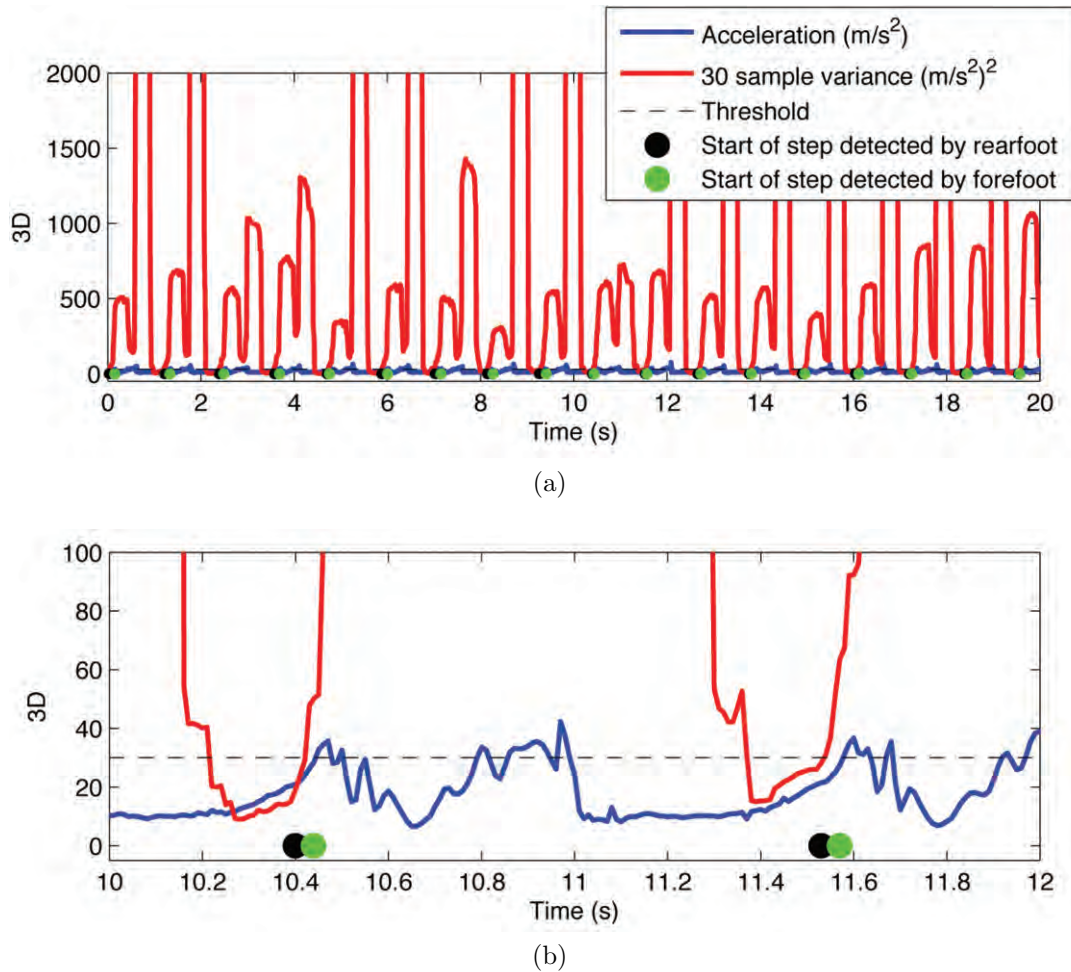
Figure 5.11: Step detection during walking using the variance of the rearfoot accelerometer signal: (a) Steps are consistently detected using this method. (b) A magnified section of the above figure showing the exact epoch of step detection.

to detect the beginning of the step must be increased. In Figure 5.11, the threshold is set to 30 $(m/s^2)^2$ to detect steps. At this threshold, most steps are detected at the same epoch as the forefoot, however, as shown in Figure 5.11, this also results in some steps being detected prior to actual heel lift.

Given that the forefoot acceleration has well defined edges that aid in the detection of step phases and that it can employ a lower threshold when detecting steps, the forefoot accelerometer is best suited for step detection.

When applied to a runner's gait, the step detection algorithm performed similarly,

with a few modifications to the algorithm. For instance, since the stance phase of the running gait is much shorter than in walking, the variance must be calculated using only 10 samples instead of the the 30 sample variance (see Figure 5.12). This modification allows the variance to descend below the threshold before the start of the next step.

The second modification made for running gaits is an higher threshold. The higher dynamics experienced during the stance phase of the running gait make it necessary to increase the variance threshold. In Figure 5.12 the threshold has been set to 30 $(m/s^2)^2$. At this level, the step detection algorithm performs very well, although not perfectly. In approximately 2-7% of steps, the step detection algorithm fails.

The missed-step phenomenon is seen at the 9 s interval of Figure 5.12 when a step is not detected because the variance does not descend below the threshold. A simple solution is to increase the threshold and thus detect the step at the 9 s epoch, however this would confound the issue greatly, since increasing the threshold would simultaneously cause the detection of false steps.

If the threshold in Figure 5.12 were increased to 35 $(m/s^2)^2$, a step would be detected at the 9 s epoch, but would also be falsely detected at the 8 s epoch. It is a matter of argument which is worse; a false step or a missed step. This algorithm is prone to both scenarios depending on the threshold that is set.

5.4 Gait Kinematics

For walkers and runners, the precise measurement of joint angles and positions can indicate overall health and locomotory efficiency. Exacting whether or not the knee comes to full extension upon heel-strike or whether the person is pushing off on their big toe can be excellent markers of pathology, weakness or simply a defining characteristic of a person's gait.

In this section, the specific movements of the walker's and runner's gaits are com-
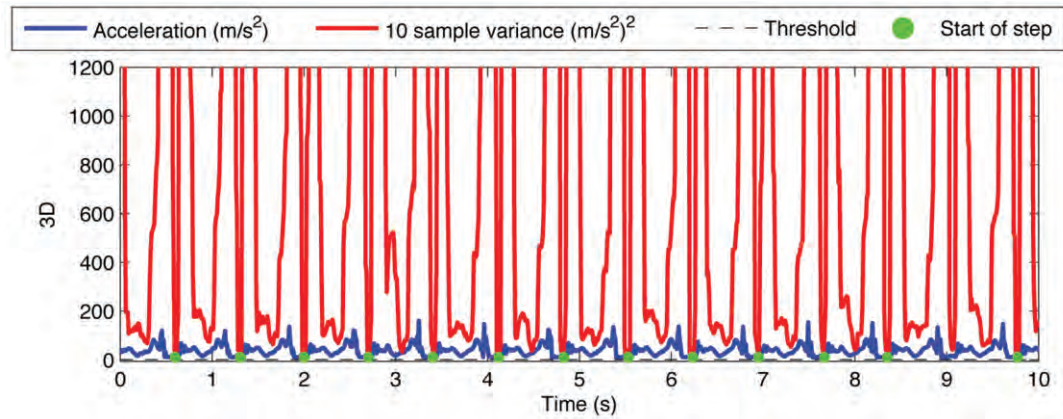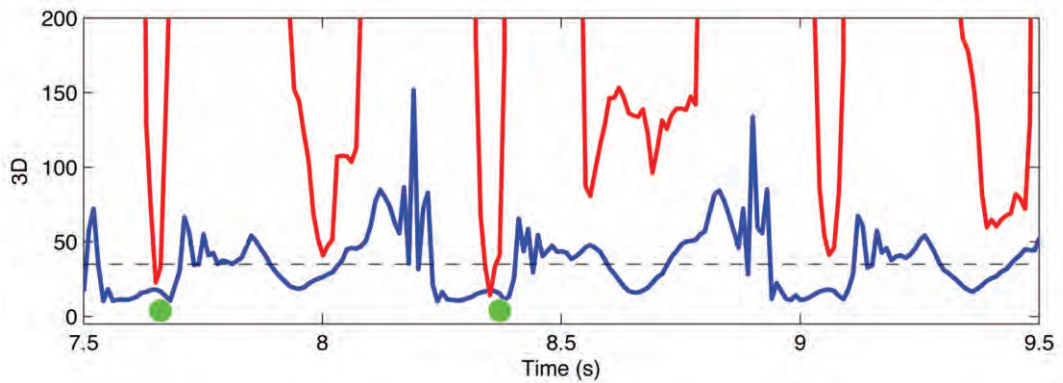
Figure 5.12: Step detection during running using the variance of the forefoot accelerometer signal: (a) Steps are consistently detected using this method. (b) A magnified section of the above figure showing the exact point of step detection and a missed step.

pared and discussed. The results presented here are meant to show the wide variety of movements that occur in different scenarios. Walking or running on flat-ground, uphill or down can have noticeable effects on an individual's gait which are consistent and measurable. Along sections of the trajectory shown in Figure 5.3, the knee and ankle rotations are examined along with the positions of the foot sensors to give an impression of the subject's movements.

In the following sections, there is no discussion of the accuracy of the measurements. that is to say, there is no attempt to compare these values to a *truth*. This discussion

is deferred to Chapter 6. However, an attempt is made to observe the precision of the measurements during a satellite outage.

When comparing two measurements that should be the same (i.e. measurements with and without GPS), an important metric of similarity is the coefficient of cross-correlation (Gao 2006). This value is used to look at the closeness of the shape of the two signals, and is computed as follows:

$$R_{xy} = \frac{n \cdot \sum xy - \sum x \cdot \sum y}{\sqrt{n \cdot \sum x^2 - \left(\sum x\right)^2} \cdot \sqrt{n \cdot \sum y^2 - \left(\sum y\right)^2}} \tag{5.1}$$

where,

R_{xy} : is the coefficient of cross-correlation,

x, y : are the time-aligned inertial and optoelectric data points, and

n : is the number of pairs of data.

Values that are close to one ($R_{xy} = 1$) mean that the signals are very similar. Conversely, values that are close to zero mean there is no correlation between the two signals. Mayagoitia et al (2002) have previously shown high levels of correlation between inertial and optoelectric data, but the study was limited to shank angles and angular velocity, and did not explore positional information or joint angles as is done here.

5.4.1 Step Kinematics

The relationship between step length (distance) and step frequency (time) is intriguing. Is more energy used to walk with long strides at a low frequency, or short strides at a high frequency? After all, walking speed is a function of both quantities, (speed = length × frequency).

Grieve & Gear (1966) established that there is a curvilinear relationship between walking speed (V) and step frequency ($SF = \alpha V^{0.58}$); in other words, the relationship

between step length and step frequency is constant over a wide range of walking speeds. A common explanation of this phenomenon is that an individual's stability and energy expenditure constrain the relationship between the two (Holt et al 1995).

To further characterize the relationship between step length and frequency, Nagasaki et al (1996) defined the ratio between the two quantities, known as the *walk ratio*. It is used as an index of spatial and temporal coordination. Figures 5.13 and 5.14 respectively depict the walk ratio for both the walking and running subjects.
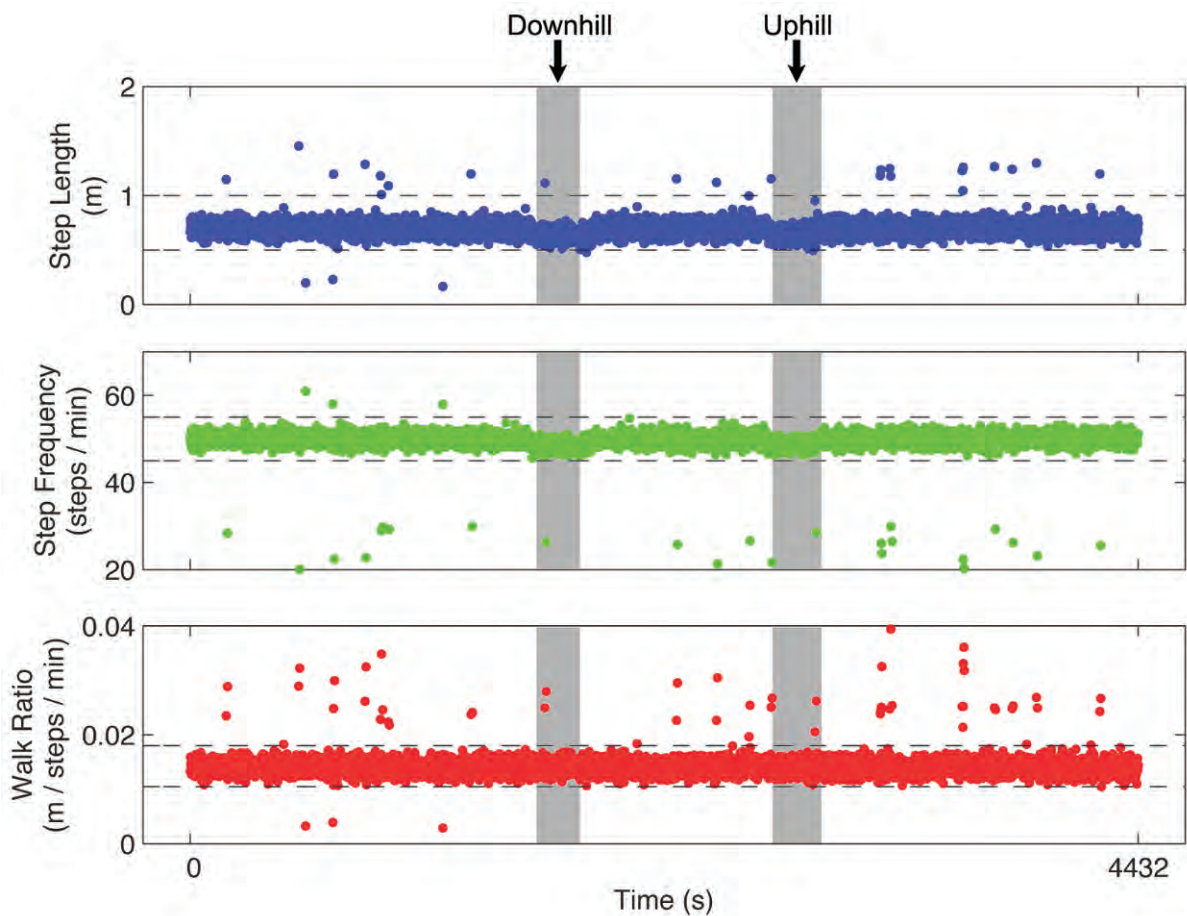
Figure 5.13: Walk ratio (step length / step frequency) during walking.

When the subject travelled downhill and uphill there was a noticeable decrease in both the step length and step frequency. This was true for both the walker and runner, however, the walk ratio remains largely unperturbed during these intervals. From Figures

5.13 and 5.14, the walk ratio is extremely consistent for both walkers and runners. Even though the walk and run were conducted at very different paces (5 vs. 11 km/h) and the subject ran up and down a hill which affected his step length and frequency, the walk ratio falls within 0.010 and 0.018 $m/steps/min$ for most steps.

Figures 5.13 and 5.14 show envelopes between which the vast majority of the step length, frequency and walk ratio points reside. Points falling outside of this envelope correspond to missed steps (steps not detected by the step-detection algorithm) and short steps (stutter steps taken by the subject while en-route). In either event, irregular steps (i.e. those steps falling outside the walk ratio envelope) are excluded from the kinematic analysis since they represent perturbations rather than typical steps. Interestingly, roughly 1% of the walking steps and 5% of the running steps are excluded using this criteria, which recall from Section 5.3.3, are the accuracy estimates of the step detection algorithm for walking and running gaits, respectively.

From Figures 5.13 and 5.14 the walk ratio for runners falls within a smaller range than for walkers. This result is consistent with previous work (e.g. Danion et al 2003). A possible explanation for this phenomenon is that the tempo and cadence for runners is particularly important for efficient energy expenditure and thus subjects are inherently prone to have a tight relationship between the length of their steps and their frequency.

Still the decreased variance in step length (and by extension in Walk ratio) shown in Figures 5.13 and 5.14 is larger than expected. According to Danion et al (2003), the variation of step length amongst running individuals should be noticeably lower than their walking counterparts.

The increased variance may be a result of the of pseudorange measurements that have low noise. In Section 4.4.2, it was assumed that the pseudorange noise was on the order of 0.5 m, and that the compensation of the lever arm resulted in a bias that fell within this noise envelope. However, hypothetically speaking, if the noise envelope was
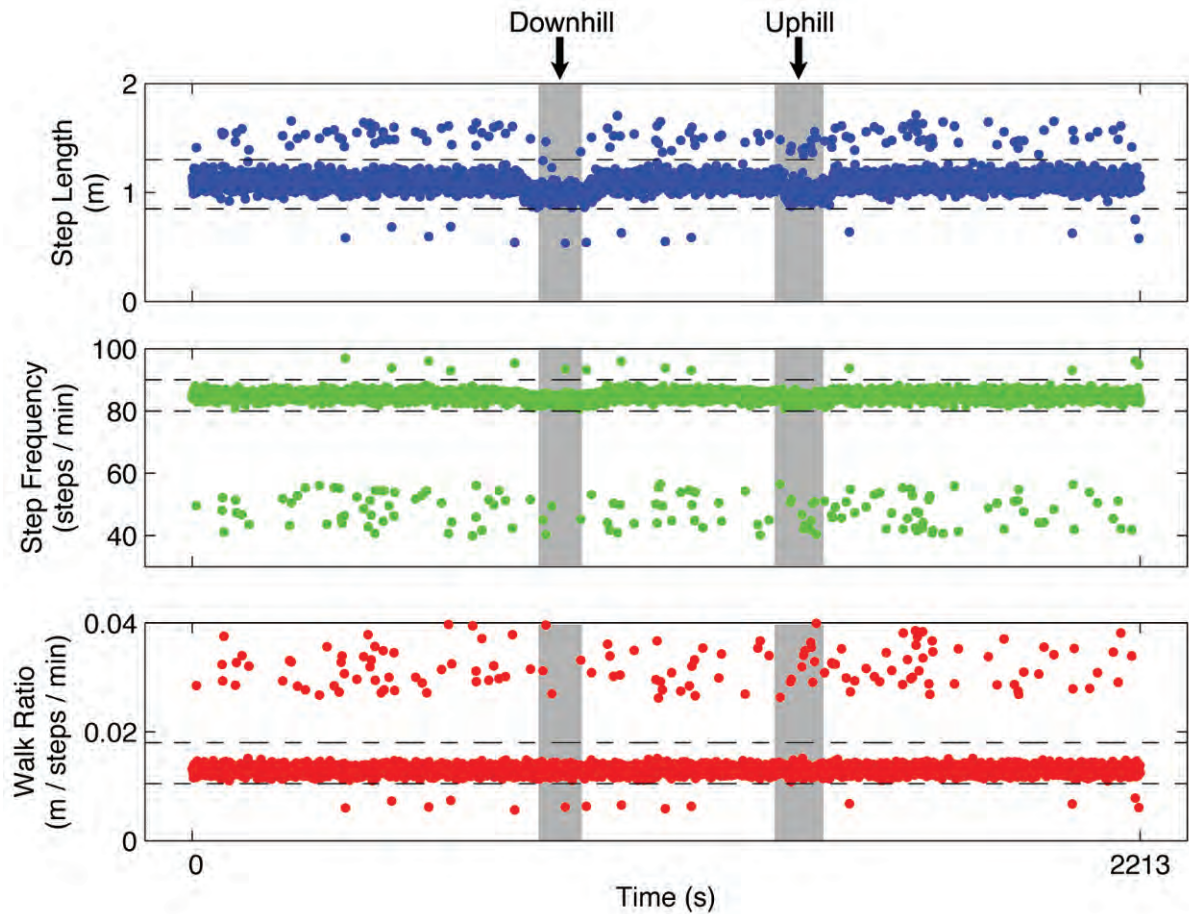
Figure 5.14: Walk ratio (step length / step frequency) during running.

in fact closer to 0.1 m or lower, the lever arm bias could result in variance such as is seen here. This hypothesis remains untested here, but further study in this area may show interesting results.

Another interesting study for the future may involve examining experienced versus new runners who presumably would have differing levels of energy efficiency. Thus wider walk ratio ranges would be expected for the new runners.

An important point made by Nagasaki et al (1996) concerning the walk ratio is that separate individuals have unique characteristic values. While the subject in this test showed walk ratio values between 0.010 and 0.018 $m/steps/min$, another may exhibit higher or lower values. This is an important consideration for using walk ratio in com-

mercial products since it would require either calibration or in-run determination of the walk ratio for a given person.

Having established a method for identifying missed or irregular steps, it is possible to explore the movements in the lower limb with an increased degree of reliability. By excluding irregularly short steps and missed steps, it is now possible to explore steps that are more or less typical. Figure 5.15 depicts the sagittal plane view of the mean step taken by the walker and runner, as well as the longest and shortest steps taken over a 30-step range. The number of steps were chosen to give the average value statistical significance and explore the range of values over a number of similar steps devoid of terrain effects such as uphill or downhill, or moving over or around obstacles.
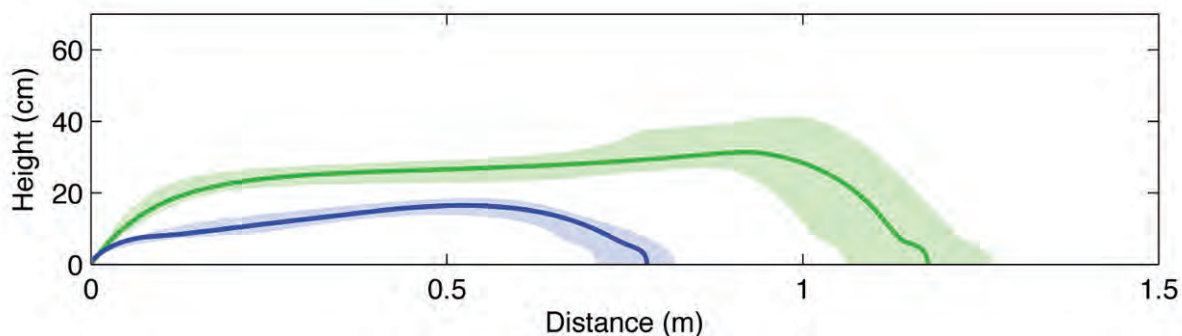
Figure 5.15: Positions of the forefoot during a mean step (line) as well as the shortest and longest steps (envelope) of a walking (blue) and running (green) subject.

In Figure 5.15 the difference between a walking and running gait becomes very apparent. In the runner's case, the distance covered in one step is much greater than for a walker. The foot also moves upwards with much greater amplitude for runners which is likely an indication of having both feet in the air at the same time. Of course, Figure 5.15 is only one comparison that is possible with the data that was gathered in this experiment.

Figure 5.16 depicts other comparisons that are possible using the position information: namely, lateralization (right vs. left - Figure 5.16a), slope (downhill vs. uphill - Figure

5.16b) and GPS available vs. outage (see Figure 5.16c).
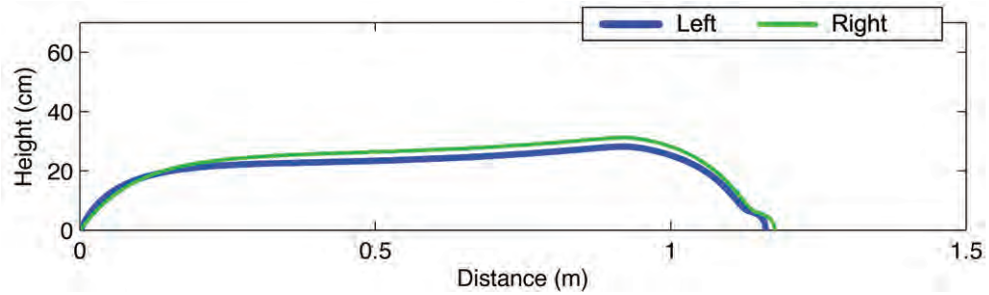
(a) Left vs. right foot during running
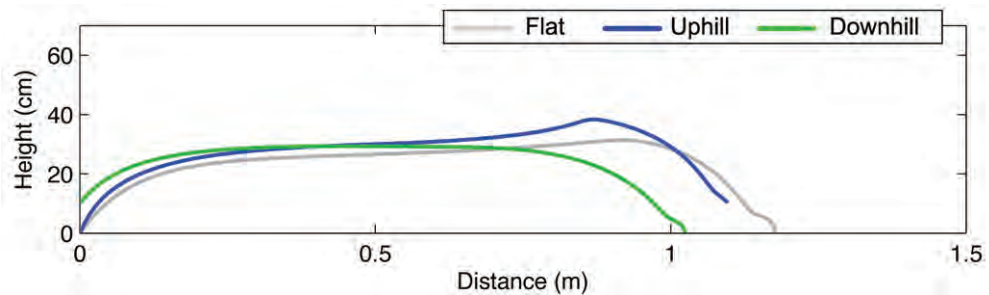
(b) Flat ground vs. uphill vs. downhill running
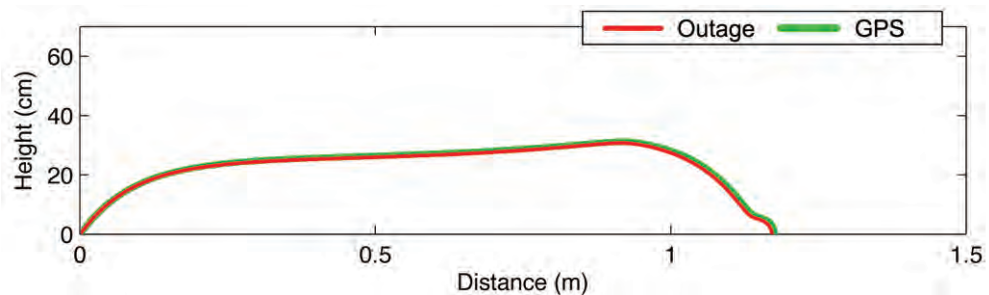
(c) GPS available vs. outage during running

Figure 5.16: Comparisons of various sagittal planes views of step in different conditions: (a) Right and left legs. (b) Flat-ground, uphill and downhill. (c) GPS available and GPS outage.

Interestingly, the right and left legs do not move perfectly symmetrically according to the measurements displayed in Figure 5.16a. This indicates that there may be muscle differences in the left leg that are leading to decreased amplitude. Clinically, lateralized gait, meaning a gait with differences between right and left legs, could indicate pathology which may require further investigation. In this case the differences are small and

there are no other indications of aberative movement so the likelihood is that these differences are either a peculiarity in this person's gait, the result of environmental factors, or measurement accuracy limitations.

Large differences can be observed in persons running up of down hill verses running on flat ground (see Figure 5.16b). In this case, the subject walked down a hill of 10% grade, and up a hill of roughly 9% grade. While these slopes are less rigorous than those explored by Lay et al (2006, i.e. 15% grade), the results follow similar patterns.

The last case (i.e. GPS outage versus having satellites observations available) is particularly interesting in this study because it provides an evaluation of the system's robustness. The use of low-cost inertial sensors in GPS/INS have been shown to degrade the navigation solution rapidly in the absence of GPS (Godha et al 2006), particularly because the heading deviates so rapidly. However, in the case of the kinematic information, the heading information does not drift much within the time of a single step. Therefore, the effects of heading drift in Figure 5.16c are marginal. Thus, only sub-millimetre deviations are observed in cases where no GPS satellite observations are available. Table 5.2 demonstrates the difference between the measurements in the presence of satellite observations and during GPS outages.

Table 5.2: Differences in step kinematics during the GPS outage shown in Figure 5.16c

	GPS Outage vs. GPS Available
Correlation (R_{xy})	1.000
RMS [mm]	0.1
Max [mm]	0.15

While there are differences between the positions estimated during GPS outage and GPS availability, the magnitude of those errors is negligible compared to the range of measurements. The signals are effectively the same as is evidence by the correlation figure ($R_{xy} = 1$) and low RMSE.

5.4.2   Rotation Kinematics

An obvious measurement in human gait analysis is the rotation about the joints of the lower limb. Knee and ankle flexion are amongst the more conspicuous rotations, however, ankle inversion and knee varus, as well as internal and external rotations are key clinical markers of a patient's gait health.

Figure 5.17 shows the mean and standard deviation of the knee and ankle rotations in the coronal, sagittal and transverse planes during 10 steps of flat-ground walking. The normal of the coronal plane, recall, is coincident with the direction of travel, while the normal of the sagittal and transverse planes are coincident with the right lateral and vertical directions, respectively. As will be shown in the next chapter, this convention departs slightly from some studies in the literature that adopt a joint axis system, however, there are also some studies that support this convention (Kidder et al 1996, Leardini et al 1999, Carson et al 2001).

Without knowing the true nature of the joint rotations it is not possible to comment on the accuracy of the rotation measurements. However, they are consistent with studies done in this field (*ibid*). The measures presented in Figure 5.17 are logical given the parameters of the experiment and fall within an expected range. The next chapter will investigate the accuracy of these measurements.

The 10 steps shown in Figure 5.17 occurred at the end of a 30 s interval when a GPS outage was simulated. This was done to investigate the effects of a GPS outages on rotational kinematic measurements, as was done in the previous section for step kinematics.

From the results in Figure 5.17, the effects of a GPS outage on the kinematic measurements are negligible ($< 0.1°$). Table 5.3 shows the correlation and RMS values for the two signals (GPS outage and GPS available). Much like the step kinematics, there are very few differences in the precision of the measurement without GPS observations
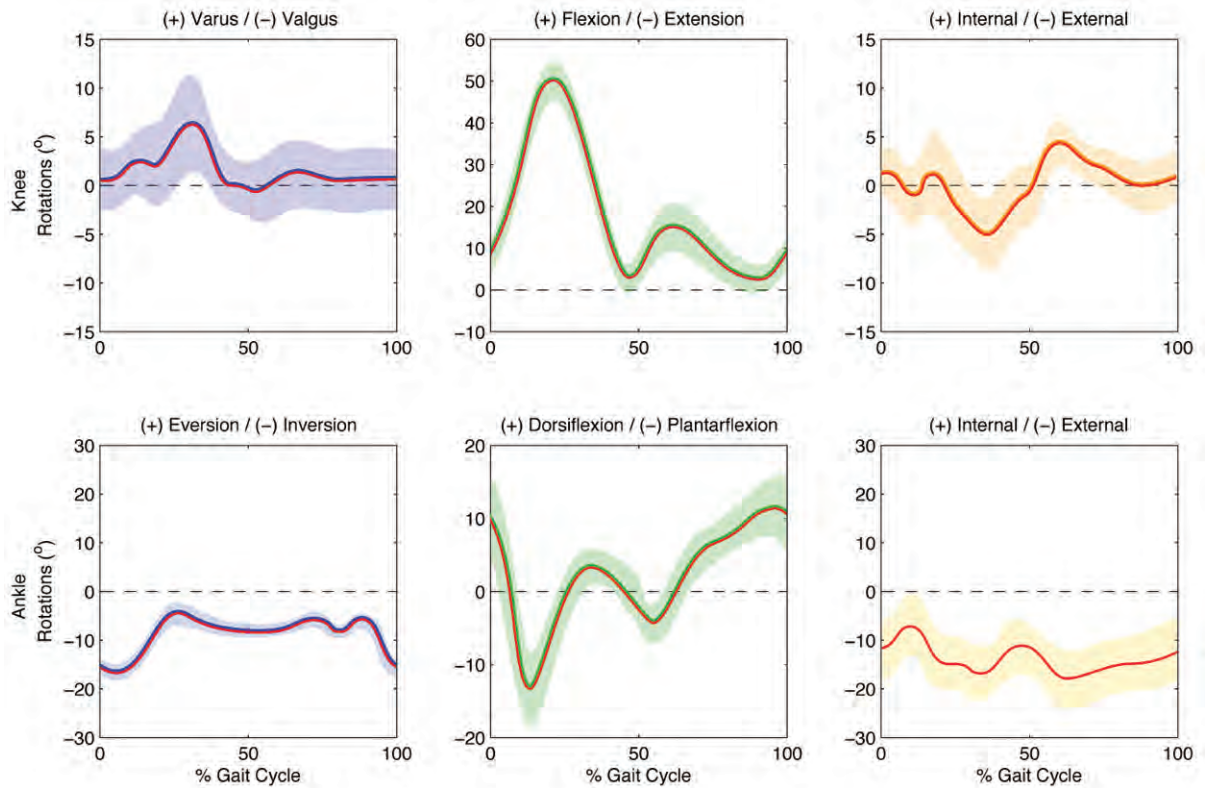
Figure 5.17: Rotations in coronal (blue), sagittal (green) and transverse (orange) planes of knee and ankle during walking gait. Rotations measured during GPS outage indicated by red line.

available.

As was shown in Section 5.4.1 there are a number of combinations of comparisons that could be performed on the given data. Similar figures to Figure 5.17 could be produced comparing uphill/downhill, left/right and a variety of other combinations. Some of these comparisons will be made in upcoming chapters and therefore are omitted here to avoid duplication.

Table 5.3: Differences in joint rotation kinematics during the 30 s GPS outages shown in Figure 5.17

	Knee Rotations		
	Coronal	*Sagittal*	*Transverse*
Correlation (R_{xy})	1.000	1.000	0.999
RMS [°]	0.05	0.05	0.07
Max [°]	0.13	0.12	0.14
	Ankle Rotations		
	Coronal	*Sagittal*	*Transverse*
Correlation (R_{xy})	1.000	1.000	1.000
Vertical RMS [°]	0.02	0.02	0.03
Max [°]	0.07	0.09	0.10

5.5   Results Summary

The experiment discussed in this chapter was the initial test of the proposed inertial-based kinematics analysis. A wide number of measurements were explored and discussed, and initial impressions are positive. A successful step detection algorithm was presented, as well as a method for applying ZUPTs during the stance phase of the walking and running gait. In addition, the walk ratio was established as a robust method to exclude faulty step measurements which will enhance much of the subsequent kinematic information.

There are many major findings in this chapter. They are significant achievements that will contribute to the research done in human gait analysis:

- *The gait cycle can be separated into four distinct phases: push off, swing, heel strike and stance.* It is helpful to decompose the gait cycle into these sub-classifications, since the goal is to detect the start and end of each step and also to isolate the stance phase to apply ZUPTs.

- *ZUPTs occur more on the forefoot-mounted GPS/INS system than any other segment of the lower limb.* Since the forefoot experiences lower dynamics during the stance phase compared to the other segments of the lower limb, more ZUPTs are applied to the forefoot GPS/INS filter. The rearfoot sensor also experiences ZUPTs

but the shank, thigh and belt mounted sensors do not incur ZUPTs during normal walking gait.

- *The forefoot-mounted accelerometer provides better measurements for step detection.* Since the forefoot IMU provides an acceleration profile that demarcates each phase of the gait cycle with sharp transitions, the method outlined in the chapter for step detection is most successful with a foreoot-mounted IMU.

- *The walk ratio is a robust metric for excluding irregular steps from kinematic analysis.* Since the relationship between step length and step frequency is well established as a consistent metric for most individuals across a wide number of walking and running speeds, it is ideal to use for missed step detection.

- *A wide variety of comparisons between various movements are possible.* As expected, the large volume of continuous measurements allows for a variety of different movements to be compared. The comparisons made in this chapter were left vs. right leg, uphill vs. downhill as well as GPS available vs. GPS outage. The number of comparisons that are possible is virtually limitless.

- *GPS outages have marginal effects on the quality of kinematic information that is observed.* While the navigation solution degrades rapidly during a GPS outage, the kinematic information is relatively unperturbed. There was perfect correlation between the measurements and only a fraction of a millimetre difference (RMS) in the positional data, and a few hundredths of a degree rotational difference (RMS). GPS data is still required to provide a navigation solution so that the kinematic information can be related to the terrain on which the walker/runner is measured.

- *Kinematics performed with the proposed inertial system are supported by other studies found in the literature.* While there is no validation of the results in this chapter,

the movement profiles (both position and rotation) coincide with other published literature.

The initial kinematic information that was shown in this chapter is consistent with the literature and describes a promising technology. The remaining issue critical for the proposed technology is a measure of accuracy. In the following chapter, the inertial architecture will be compared to the traditional optoelectrical system, thus validating the results given by the current research.

Chapter 6

Validation of Inertial Kinematic Results

In order to install any new technology into a field of study such as motion capture and analysis it must first be compared and contrasted to existing methodologies and measured against the *status quo*. This chapter compares the proposed inertial kinematics and the traditional optoelectrical measurements.

Many challenges must be overcome in comparing the two technologies. Firstly, the two measurements are not inherently time synchronized. While GPS measurements are precise, the optoelectic measurements are timed by a far lower quality computer clock. Having the two measurements aligned in time within the measurement interval is important to ensure that the appropriate measurement epochs are being compared.

Secondly, both systems require the placement of sensors in similar places on the body. Reconciling this requirement and adjusting the respective methodologies to accommodate each other is an important consideration. A discussion of the adaptations implemented in this experiment is included along with the comprehensive description of the test set-up.

By having a side-by-side comparison of these two technologies the goal is to validate the measurements of the new against the reliability of the old and point out any differences that may exist between the two modalities.

6.1   Test Description

A series of tests were conducted in the Human Performance Lab (HPL) at the University of Calgary in July of 2008. The purpose of the tests was to collect kinematic data simultaneously using inertial sensors and optoelectrical motion capture equipment for a walker and runner.

A single subject was fitted with both sets of sensors and asked to perform a series of walking and running trajectories. Both datasets were then processed post-mission to yield kinematic results that could be compared and contrasted. The results were then analyzed for similarities and differences in order to validate the results of the inertial kinematics methodology.

6.1.1   Sensors and Equipment

The experimental setup for collecting the inertial measurements was the same as in the previous chapter (see Section 5.1.1). Nine IMUs, an Antcom antenna and a NovAtel OEM VI GPS receiver housed in the NavBox^{TM} data recorder were attached to the test subject in the same way as in Chapter 5 (see Figure 6.1).

The subject was asked to initialize the inertial system by walking outdoors for 10 minutes in open sky conditions before returning indoors to conduct the motion analysis experiment. The subject was asked to return outdoors between trials for another 10 minutes. Thirty to sixty seconds elapsed between when the subject returned indoors (away from satellite view) and when the kinematic experiment took place.

Concurrent to the inertial measurements, optoelectrical measurements were gathered. Eleven reflective optical markers were affixed to the right leg in order to perform the optoelectrical measurements. The thigh was represented by a marker placed on the anterior aspect of the quadriceps approximately half way up the thigh, another 10 cm distally still on the anterior aspect, and another on the lateral surface of the thigh. The shank was represented by a marker placed 4 cm distally from the knee on the anterior surface, as well as others on the lateral and medial maleolae. The rearfoot was represented by a marker affixed to the posterior aspect of the rearfoot IMU, and others on the lateral and medial segments overtop the calcaneus.

Eight *Motion Capture*^{TM} cameras synchronously captured single channel optical video at 240 Hz in order to track the optical markers in 3D space. The Motion Analysis system
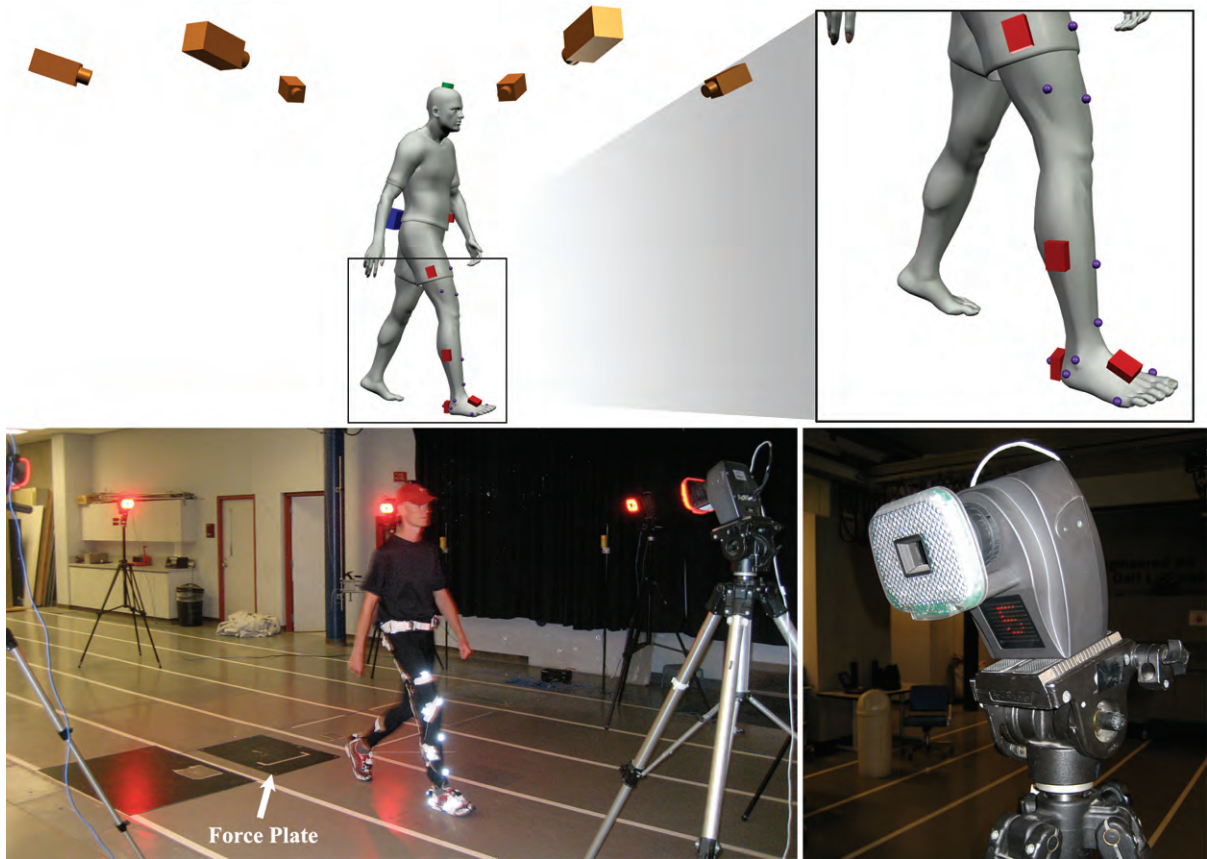
Figure 6.1: Validation of inertial kinematics with side-by-side comparison of optical motion analysis. (Top) representation of inertial sensors and optoelectrical setup. (Bottom) pictures of the experiment in the Human Performance Laboratory.

was calibrated before the experiment. The camera orientation parameters were adjusted until the positional residual of 0.5 mm could be attained. The calibration of the system involved moving a wand with known length (500.05 mm) through the measurement space and allowing the capture software to set the camera orientation parameters. If the software was unable to fix to a sufficiently low residual the calibration was repeated until the desired level of position accuracy was attained. The exact method that the Motion Capture software uses to set the orientation parameters was not defined in the operating manual.

The HPL is equipped with a Kistler force plate (Model: Z4852/c) which is positioned

in the middle of the field of view of the camera setup (see Figure 6.1). The force plate data is captured at 2400 Hz and is synchronized with the camera measurements. During each motion capture trial the subject was asked to step on the force plate as they passed through the camera measurement space. The force plate data was used to synchronize the optoelectrical and inertial measurements as will be discussed in the following section. The middle of the force plate also defined the origin of the lab coordinate frame. All positions and rotations derived from the optoelectric methods are referenced to this frame.

The subject was asked to perform six successful motion capture trials: 3 walking and 3 running. A trial consisted of passing through the measurement volume of the camera setup with a straight-line walking or running gait (approximately 5 m distance - see Figure 6.1). A successful capture involved having all optical markers visible by at least 3 cameras as well as contact with the centre of the force plate. When these conditions were not met, the trial was discarded and repeated. This procedure resulted in 9 walking and 6 running steps being recorded using both inertial and optoelectric modalities.

Positions of the segments and inter-segmental rotations measured by the optoelectric system were calculated using a proprietary software, Kintrack^{TM}, that implements the procedures outlined in Söderkvist & Wedin (1993). The software processes the positional measurements with a 5 Hz Butterworth Filter. The 5 Hz threshold is considered limit for organic movement above which is considered measurement noise (*ibid*).

6.2 Time Synchronization of Inertial and Optical Data

In order to compare the inertial and optoelectric measurements it is imperative that the two data sets are aligned in time. That is, the measurements of the two data sets must be measuring the same movement at the same time otherwise unnecessary errors are introduced. In order to avoid misaligning the measurement epochs, the resolution of the time alignment had to be within half of the inertial data rate ($0.5 \times 10 \ ms = 5 \ ms$). For

this reason, a special protocol was developed which would allow the sets to be aligned in post-mission.

At the start of each test, the subject stood in front of the force plate and stomped on it. This action has a twofold effect; first, the stomp could be observed in the accelerometer signal as a large spike, and second, could be measured very precisely by the force plate which is synchronized with the optoelectric data. Using the characteristic signals the inertial and optoelectric data sets were synchronized.

The left side of Figure 6.2a and Figure 6.2b show the accelerometer signal and the force plate data during the time interval when the stomp took place. In these figures, the two signals have been synchronized by aligning the moment of abrupt acceleration change in the accelerometer and the commencement of force being applied to the force plate. From Figure 6.2b the alignment of the data sets seems precisely aligned (within the required 5 ms) with very little ambiguity as the peaks of both the IMU acceleration and ground reactive force seem coincident.

As a further measure of precision between the two sets, Figure 6.2c shows the force plate data aligned with the 3D acceleration of the rearfoot IMU. Recall the discussion in Section 5.3.1 where the start of the heel strike phase was marked by a sharp peak and subsequent deceleration in the acceleration of the IMU, followed by the flat stance phase. In Figure 6.2c, this event coincides with the start of force being applied to the force plate. Furthermore, the acceleration of the IMU as the toe pushes off is precisely aligned with the moment at which the force applied to the force plate terminates.

The synchronization of the inertial and optoelectric data sets to within 5 ms by means of a stomp is an effective means of aligning the measurements in time. The same protocol was used for the validation of walking and running data sets. For the remainder of this chapter, data sets are synchronized using this method.
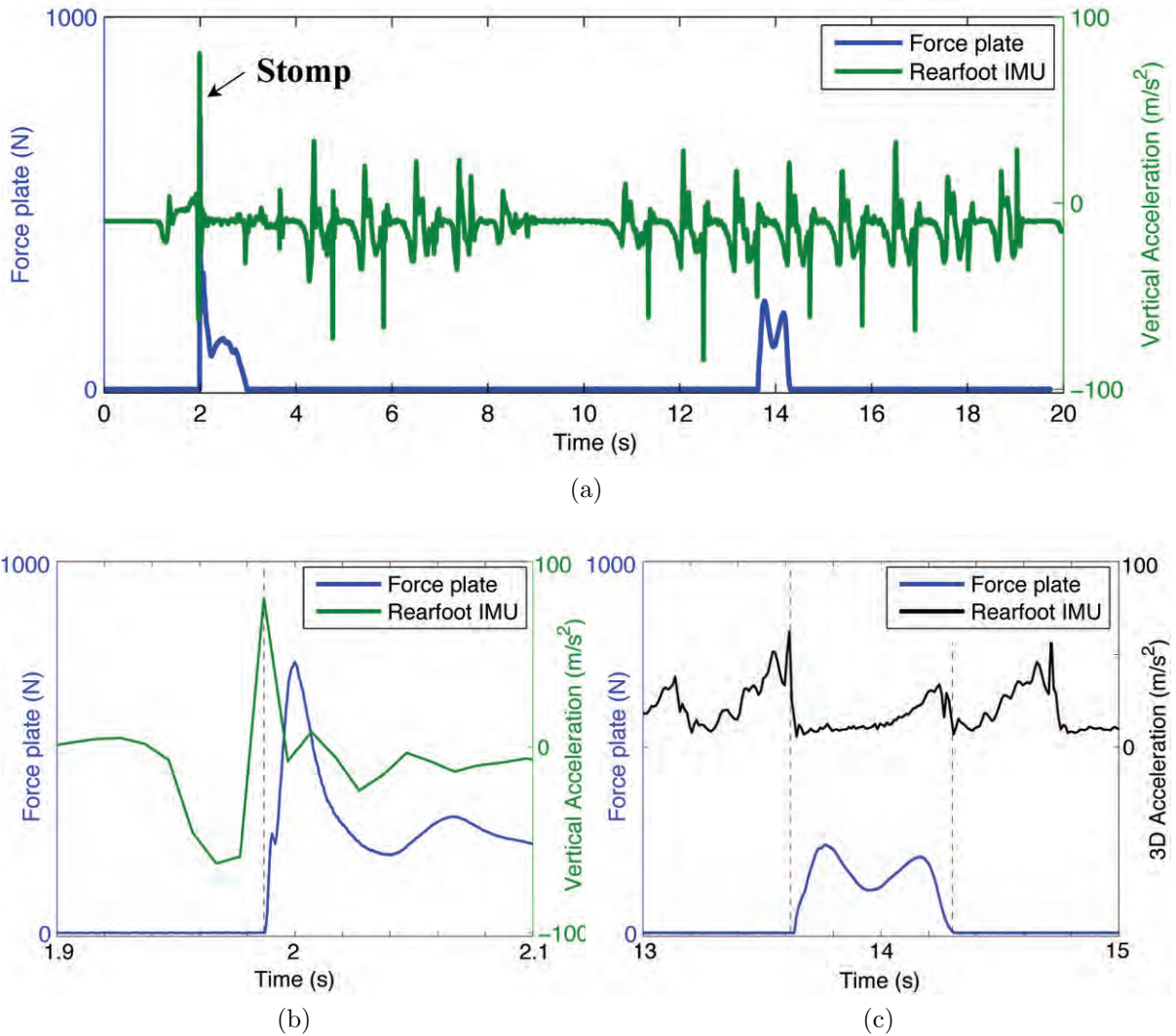
Figure 6.2: Time alignment of inertial and force plate data (a) The vertical acceleration and force plate datasets, (b) Zoomed in view of the alignment between acceleration and force plate data using stomp. (c) Zoomed in view of the alignment of force plate data with the accelerometer derived step phases.

6.3 Comparison of Optoelectric and Inertial Kinematics

Since optoelectric measurements are considered the *gold standard* in terms of measurement accuracy, it is reasonable to compare an up-and-coming technology side-by-side in order to validate the newer generation measurements. For the remainder of the chapter, the focus is on the validation of the proposed inertial system by means of comparison with optoelectrical measurements. First a comparison of the positional data output by the two systems is presented, and secondly, the rotational data.

6.3.1 Comparison of Step Kinematics

The comparison of positions measured by the inertial and optoelectric systems is a key determinant in validating the proposed inertial kinematic system. As a motion analysis modality, the inertial system must be able to provide reasonably good positional information. What is the definition of reasonably good? The answer is that it will depend on the application. The point is not to install this technology in any niche of motion capture, but to offer a quantification of the errors present in the proposed inertial system.

The comparison is made difficult because the two systems can not measure the same point in space at the same time (see Figure 6.3). While the optoelectric system measures the position at given marker's centroid, the inertial system is centred at the origin of the sensor triad. Whatsmore, the inertial system is referenced to an ECEF coordinate frame, while the optical markers are measured in a local coordinate frame that can not be reliably transformed to the inertial system. It is therefore expected that there will be some residual errors from the lever arm between the two points in space.

Figure 6.4 shows the results of the two experiments, walking and running. A single step from the experiment (as measured by optoelectric and inertial methods) is depicted in the figure. In order to account for the lever arm between the two systems the initial position of both sets were set to zero (i.e. a common point) and all other values in Figure
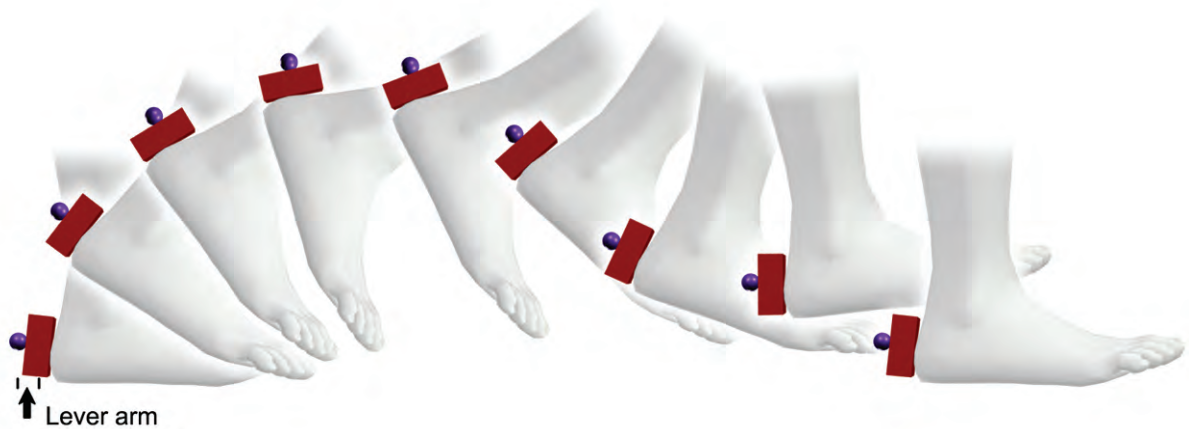
Figure 6.3: Optical markers (purple) and inertial sensor centre (red) are offset by a lever arm that is assumed to be 1 *cm*. This error was corrected in the values reported.

6.4 are depicted relative to this common reference. In order to minimize the error caused by the assumed lever arm, the marker that was placed closest to the origin of an inertial sensor was used. For this reason, the position of the rearfoot IMU was used as well as the marker that was adhered to the surface of the rearfoot IMU. The distance between these points in 3D space is no more that 1 centimetre.
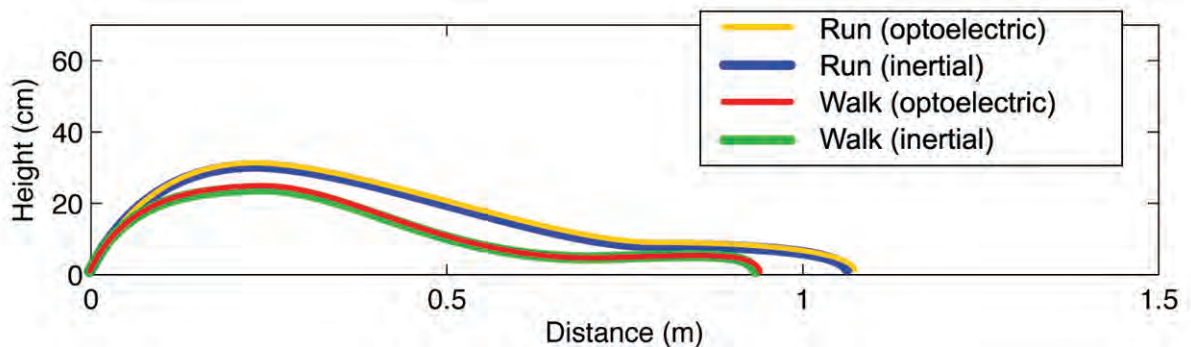
Figure 6.4: Positions of rearfoot measured by inertial and optoelectric sensors during walking (green/red) and running (blue/orange).

Figure 6.4 shows that the positional accuracy of the inertial system is very good for both for walking and running since the two signals (inertial and optoelectric appear to be very close together. In order to measure the exact departure of the inertial solution from the optoelectrical measurements, the RMS and correlation values are presented in Table

6.1. The correlation and RMS values in Table 6.1 reflect all of the points common to both inertial and optoelectric systems for the 9 walking steps (216 points) and 6 running steps (84 points).

Table 6.1: Comparison of step kinematics using inertial and optoelectrical measurements after tilt compensation

	Walking	Running
Correlation (R_{xy})	1.000 (n = 216)	1.000 (n = 84)
RMSE - 3D [m]	0.006 (n = 216)	0.012 (n = 84)
Max Error [m]	0.010	0.016
Actual step length - *optoelectric* [m]	0.832	1.165
Estimated step length - *inertial* [m]	0.828	1.156
SL RMS [m]	0.004 (n = 9)	0.009 (n = 6)
Percent Error SL [%]	0.50	0.75

The 3D RMS error of the positions of the rearfoot sensor are 6 mm for the walking gait and 12 mm for the running gait. The correlation values indicate that the inertial units are able to observe the changes in position extremely well. The step length estimation using the integrated INS velocities was very successful, resulting in less than a 1% error for both the walking and running gaits. This translates to a 4 mm error for the walking step length and a 9 mm for the running step length.

The increased error for the running gait is likely due to the higher dynamics of the foot. Despite the ZUPTs being applied with higher frequency to the running gait due to more frequent steps, the decreased number of ZUPTs result in less accurate velocity error determination than in the walking gait. Since the positional information is derived by integrating the velocity, the higher velocity errors result in higher positional RMSE as well.

Overall, the accuracy of the step kinematics is very good with an RMSE less than a centimetre for the walking gait, and only slightly larger for the running gait. If the true lever arm between the optical marker and the inertial sensor centre were known, up to a few millimetres might be removed from the error budget reported here. However, at

the time of the experiment only an estimate was made. Due to the resources and cost involved with the optoelectric equipment setup, the experiment was not be repeated, and in any event, the above results confirm the performance of the inertial approach for positional kinematics.

6.3.2 A Comparison of Rotation Kinematics

Positional accuracy is only one factor that can assess the accuracy of the proposed inertial system. The translations that an object experiences are coupled with its rotations to give a full description of its movement through space. Therefore, in order to establish any new measurement method as an alternative to an already established protocol, the proposed technology must prove both positional and rotational accuracy.

In the previous section, the position accuracy of the proposed inertial system was established to be approximately 1 *cm* based on the 9 walking steps and 6 running steps. The discussion now turns to the rotational measurements, and a comparison between the rotations computed using the traditional optoelectric and proposed inertial methodologies. Figure 6.5 shows the rotation measured by inertial and optoelectric sensors, for both walking and running gaits.

Figure 6.5 shows the difference between walking and running gaits and displays both inertial and optoelectric measurements. An encouraging result in Figure 6.5 is similarity between the inertial and optoelectric measurements for both walking and running gaits.

Chapter 5 described the differences between the walking and running gait cycles. Figure 6.5 confirms some of these differences. For instance, knee and ankle flexion (sagittal plane rotations in Figure 6.5) show a delayed dorsiflexion in the first half of the running gait that is indicative of a longer push-off phase compared to the walking gait. Similarly, coronal plane knee varus and ankle eversion show similar delays.

Figure 6.5 depicts remarkable differences between the rotations experienced while running verses walking. Knee and ankle sagittal plane rotations are particularly different
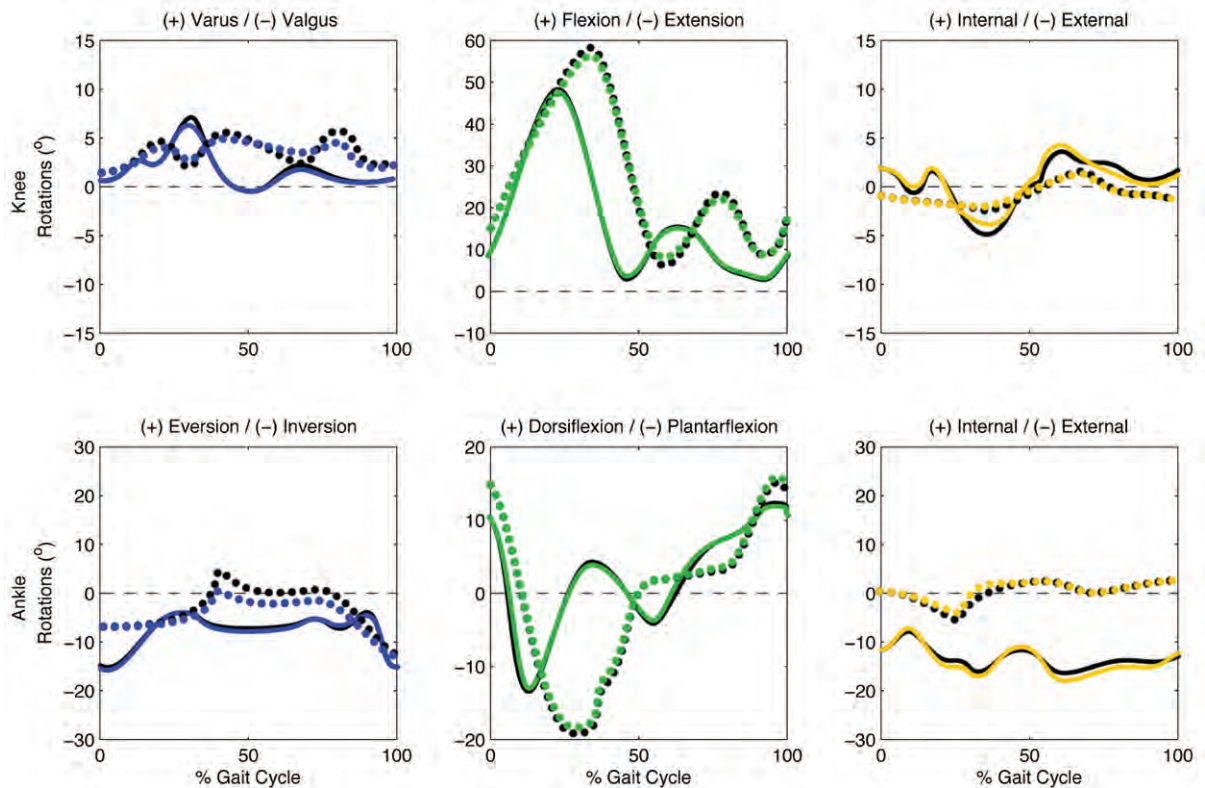
Figure 6.5: Knee and ankle rotations of walking (—) and running (●) gaits measured by inertial (colour) and optoelectric (black) methods. Rotations in the coronal (blue), sagittal (green) and transverse (yellow) planes shown.

and show very little correlation between the walking and running gaits.

The point of this chapter, however, was not to comment on the differences between walking and running gaits, but to validate the position and rotational measurement accuracy of the inertial measurement system. As such, the rotations in Figure 6.5 show that the inertial and optoelectrical measurements are in close agreement. Table 6.2 quantifies the errors in Figure 6.5 as well as the closeness in the rotational profiles.

As per the values in Table 6.2 the closeness of the rotational curves is excellent. The high correlation values show that the rotation changes are measured consistently with both methodologies. That is to say, when the optoelectrical system measures a change in direction, the inertial system measures that change equally well. This is particularly

the case for rotations in the coronal and sagittal planes (flexion and varus/eversion, respectively), since the correlation values approach 100% in almost all cases.

The slightly lower performance in the transverse plane may be explained by the lower observability of the heading angle errors in the Extended Kalman Filter, as explained in Section 4.4.1. While the correlation in the transverse plane is marginally lower than in the coronal and sagittal planes, the performance is still excellent.

The RMS rotation error in almost all rotations is confined to a few degrees, which is considered very good. Optoelectric measurements have 1° rotational measurement accuracy (Reinschmidt et al 1997), thus the performance of the proposed inertial system is very high quality. In most cases in Table 6.2 the difference between inertial and optoelectric measurements is very close to the error budget of the optoelectric method. This result is encouraging and places the proposed inertial measurements on par with the traditional methodology.

While the absolute magnitudes of the errors are not large, the percentage of the RMS error as a fraction of the full scale of the rotations being measured is interesting. Table 6.2 shows the ratio (in percent) of the error to the full measurement. This quantity reflects the amount of error relative to the magnitude of the rotation being measured, and is therefore indicative of the impact that the measurement error could have on a given rotation. Higher values reflect an increased proportion of error, and thus lower reliability in the measurement.

The rotations in the sagittal plane (i.e. flexion) have substantially higher reliability, based on their lower error/full scale percentages. This result is a direct consequence of the large magnitude of the rotations measured in the sagittal plane. This means that flexion angles are more reliable than the lower magnitude coronal and transverse rotation measurements. Similar findings comparing bone-mounted and skin-mounted optical markers led Reinschmidt et al (1997) to conclude that sagittal plane measurements

Table 6.2: Errors of joint rotation kinematics measured by inertial sensors shown in Figure 6.5

	Knee Rotations		
Walking			
	Coronal	*Sagittal*	*Transverse*
Correlation (R_{xy}) *	0.992	0.995	0.972
RMS [°] *	0.98	1.17	1.92
Error / Full Scale [%]	13.1	2.6	19.2
Max [°]	1.92	3.19	2.13
Running			
	Coronal	*Sagittal*	*Transverse*
Correlation (R_{xy}) **	0.987	0.992	0.991
RMS [°] **	1.28	1.57	0.53
Error / Full Scale [%]	32.0	3.0	19.2
Max [°]	2.02	3.19	0.94
	Ankle Rotations		
Walking			
	Coronal	*Sagittal*	*Transverse*
Correlation (R_{xy}) *	0.989	0.989	0.983
RMS [°]*	0.71	1.25	1.12
Error / Full Scale [%]	6.4	5.0	26.7
Max [°]	2.21	2.62	2.40
Running			
	Coronal	*Sagittal*	*Transverse*
Correlation (R_{xy})**	0.989	0.995	0.972
RMS [°]**	2.33	1.42	1.04
Error / Full Scale [%]	21.1	4.1	13.0
Max [°]	5.32	2.02	2.09

* n = 216

** n = 84

are the only reliable rotational information to come from studies based on skin-mounted sensors.

6.4   Results Summary

This chapter featured a validation of the proposed inertial kinematics system by comparison to traditional optoelectrical measurements. The outcomes of this experiment are very promising for the proposed inertial method for human motion analysis. The major findings of this experiment are summarized below:

- *The synchronization of the inertial and optoelectric data sets by means of a stomp proved to be an effective means of aligning the measurements in time.* It is estimated that the data sets are aligned within one half of the inertial data rate ($5\ ms$) using the stomp protocol.

- *Positional measurements of a step using the inertial method have very good accuracy for both the walking and running gaits.* The 3D RMSE of the measured steps was $0.6\ cm$ for the walking gait and $1.2\ cm$ for the running gait, with maximum errors of 1.0 and $1.6\ cm$, respectively.

- *Step length estimation using the inertial method is done at a high level of accuracy.* The distance travelled by the foot during one walking gait cycle is accurate to $4\ mm$ using the proposed inertial technology. For the running gait, the step length was accurate to $9\ mm$. The estimation of walking and running step lengths therefore have 0.50% and 0.75% error, respectively.

- *Rotational measurements within the duration of one step have very good accuracy for both the walking and running gaits.* The RMSE during a step was less than $2\ ^\circ$ in almost all cases. This makes the accuracy of the proposed inertial measurements only slightly less than the traditional optoelectric methodology.

- *Flexion angles are the most reliable angles measured with the proposed inertial system.* The percentage of the measurement error in terms of the magnitude of the rotations being measured was much lower in the sagittal plane owing to the large full scale of rotations measured in this direction.

Overall, the proposed inertial method for human lower limb kinematics has been shown to yield measurements that are in very good agreement with those of the traditional optoelectric method. The results of this experiment show that the proposed research could lead to an alternative approach to human motion capture usable for a wide variety of applications. These results are very encouraging for this line of research and show the viability of the technology.

Chapter 7

Pedestrian Navigation & Inertial Kinematics During a Marathon

The use of an inertial system for kinematic analysis opens up many new avenues of study. Since the measurement units are not limited to the laboratory, larger, more contiguous datasets are possible. Moreover, subjects can be monitored while they perform tasks in a variety of settings. In effect, kinematics can be done anywhere, and data can be collected for as long as there is storage to hold all of the information.

In this chapter, the results of a study performed on December 2, 2007 during the Las Vegas Marathon are discussed. Emphasis is placed on the combination of navigation and kinematic data. The author is not aware of any documented studies with such a complete assay of kinematic information taken throughout a marathon.

7.1   Test Description

The test was run in Las Vegas, Nevada, starting outside the Mandalay Bay Hotel and Casino, and proceeding through the streets of Las Vegas and returning within a few hundred metres of the starting point. The course was set out by the organizers of the Las Vegas Marathon and the distance of 42.2 km was measured and certified by United States of America Track & Field (USATF 2008). The participants of the race were timed using radio frequency identifiers (RFID) which were operated by SAI Timing (2008). In this case, the author ran the course starting at 6:15:49 am and finishing in 3 hours, 36 minutes and 42 seconds (3:36:42).

7.1.1 Sensors and Equipment

The experimental setup for collecting the inertial measurements was the same as in Chapter 5 (see Section 5.1.1). Nine IMUs, an Antcom antenna and a NovAtel OEM VI GPS receiver housed in the NavBox^{TM} data recorder were attached to the runner in the same way as in Chapter 5 (see Figure 7.1).

Unfortunately, during the course of the experiment, both forefoot IMU sensors were damaged and the data could not be recovered. The right-forefoot IMU was disconnected very early in the race, and the left-forefoot IMU suffered cable damage that prevented the data from being logged at all. The data collected during this experiment was processed using the pedestrian GPS/INS software outlines in Chapter 4. The step estimator was used on the rearfoot GPS/INS. The step detection was verified by visually inspecting the 3D rearfoot accelerometer signal for all of the results presented in this chapter.

A GPS reference station's observation and ephemeris data were downloaded from the Internet. The base station was part of the IGS Network. The baseline between the rover and reference station was 24-36 km for the entire trajectory (see Table 7.1). The downloaded files gave 1 Hz phase observations that could be used to calculate a double difference, float ambiguity reference trajectory.

Table 7.1: Position of the IGS-APEX3360 base station receiver

Latitude	36° 19' 08.82783"
Longitude	-114° 55' 54.43857"
Height	761.059 m

In order to provide reference trajectory with which to compare the navigation solution of the proposed GPS/INS system, a double difference, float ambiguity navigation solution was computed using FLYKIN+^{TM} software, developed by the PLAN Group at the University of Calgary.
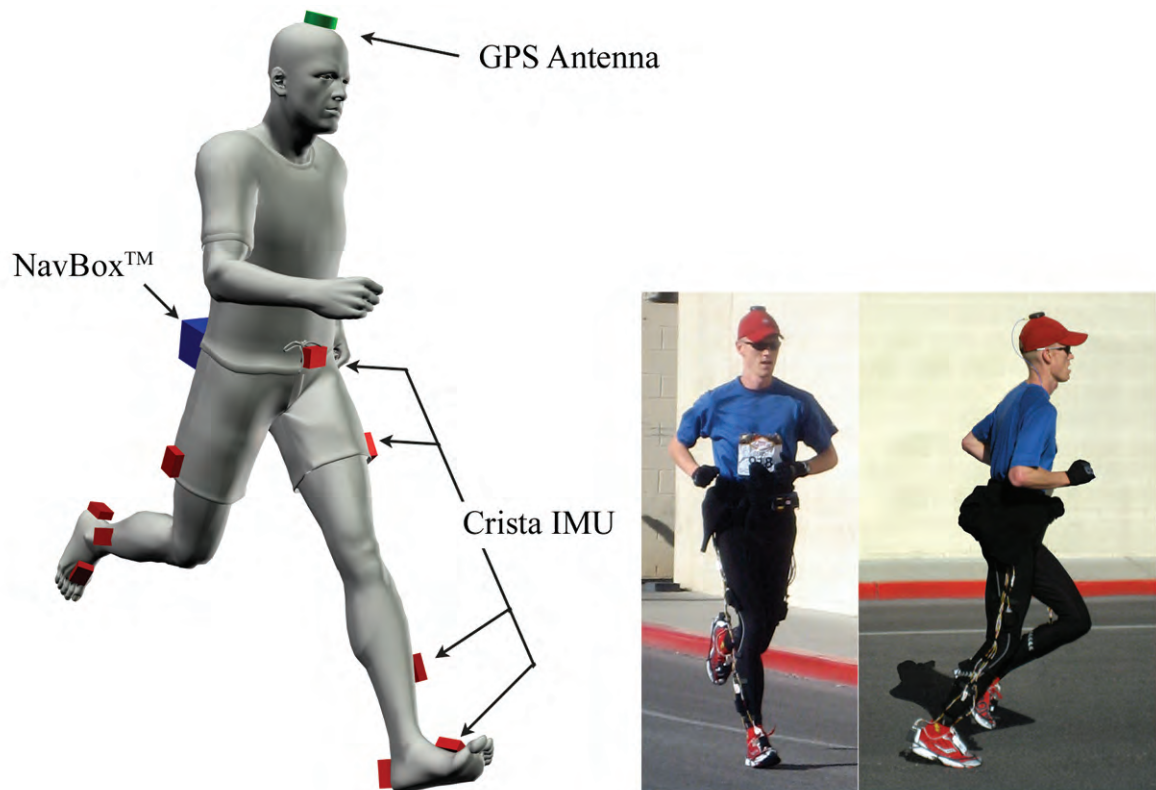
Figure 7.1: NavBox^{TM} with Antcom antenna and Crista IMUs. Placement of inertial sensors (Crista IMU^{TM} × 9), GPS antenna and NavBox^{TM} data recorder with NovAtel VI^{TM} GNSS receiver. (inset) Photos taken during the Las Vegas Marathon on December 2, 2007.

7.2 Reference Navigation Solution

Figure 7.2 shows the reference navigation solution. With a baseline of 24-36 km for all points shown, the estimated position accuracy of the float ambiguity phase solution is approximately 25-35 cm (1σ) based on the the values in Table 2.1.

In addition to the planimetric position (see Figure 7.2a) and the elevation profile (see Figure 7.2b), the horizontal velocity of the runner's antenna (computed from single point Doppler measurements) is represented by the colour bar to the right of Figure 7.2b. From the velocity information, the runner slowly increased his speed over the first 3 km and then slowed by approximately 1 m/s in the last 10 km of the race, but remained

(a)

(b)
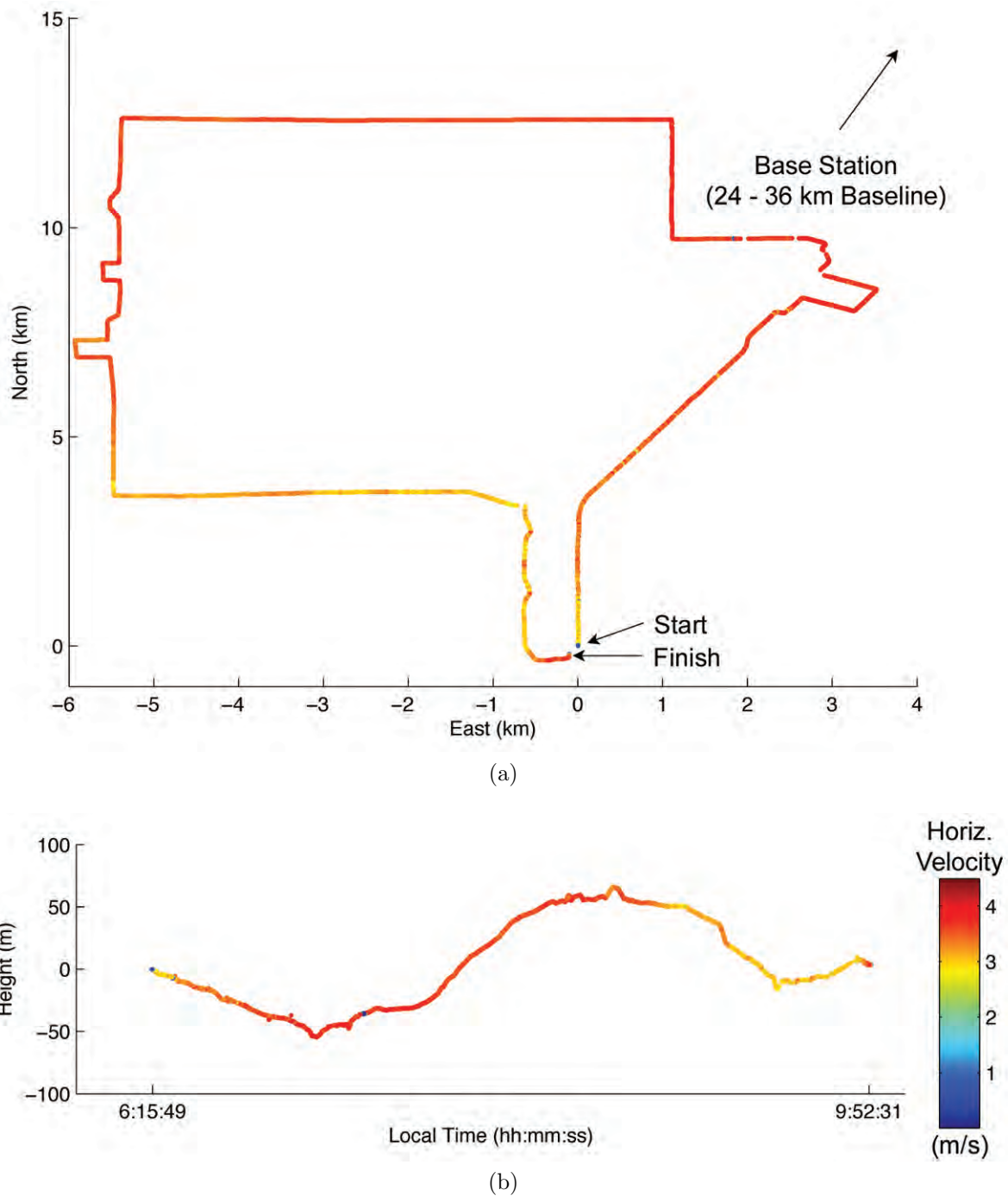
Figure 7.2: Double difference, float ambiguity reference navigation solution with single point Doppler-derived velocity information superimposed: (a) Horizontal trajectory. (b) Elevation trajectory.

otherwise consistent. The mean horizontal velocity was 3.125 m/s for the duration of the race. The accuracy of the velocity information is approximately 0.06 m/s (1σ) based on the computed positional 2D standard deviation.

The sudden stop by the test subject at 12.4 km reflects a 15 second period where the runner took a pause. Notice that the NovAtel OEM VI was able to keep tracking the five satellite signals while the subject was indoors despite the plastic roof overhead, although from Figure 7.3 the number of satellites tracked did decrease due to the shrouding of the plastic housing of the building. No kinematics were performed over this time interval.
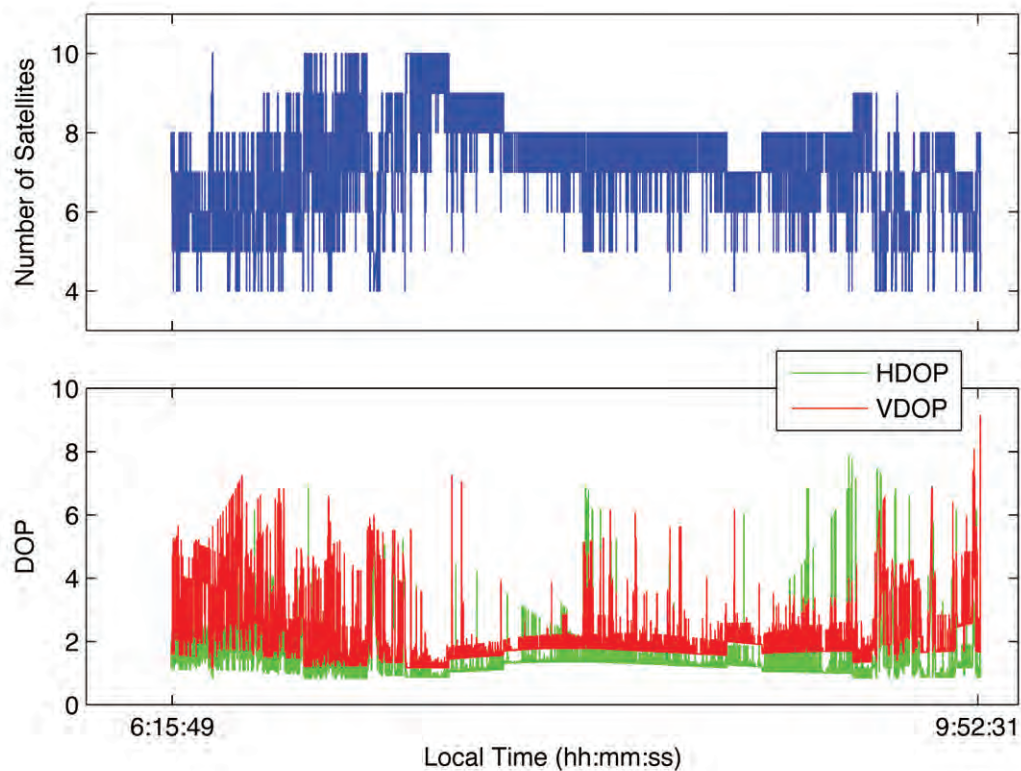
Figure 7.3: Number of satellites visible by the antenna (top) and horizontal dilution of precision (HDOP) and vertical dilution of precision (VDOP) (below) during the marathon

In addition to the number of satellites tracked over the course of the marathon, Figure 7.3 also shows the horizontal and vertical Dilutions of Precision (HDOP and VDOP, respectively). Solutions that resulted in a geometric Dilution of Precision (GDOP) greater than 10 were excluded. This condition was encountered rarely over the course of the

data, reflecting good satellite availability and geometry.

The large variability in the number of satellites, and thus the DOP figures, shows the high level of dynamics experienced by the antenna. While the antenna was placed on the top of the runner's head in order to maximize satellite visibility, it is also subjected to a certain level of pitch and roll which caused difficulty with continuous tracking of satellites. Still, for the vast majority of the course, satellite positions were available to aid the GPS/INS and reference solutions.

There were numerous places where enough satellites were occluded to prevent the determination of the runner's position by satellites alone. These intervals of satellite occlusion correspond with under-passes that existed along the marathon course.

7.3   Pedestrian GPS/INS Navigation Solution

In this experiment, the availability of a high accuracy reference solution makes it possible to compare the GPS/INS navigation solution and the reference to give an impression of the overall accuracy of the system. Figure 7.4 shows the relative trajectory of the GPS/INS navigation solution using the right rearfoot IMU, compared to the reference. Also included in Figure 7.4 is the trajectory given by single point, least-squares as provided by the PLAN Group's C3NavG^2 ^{TM} software.

From Figure 7.4 it is obvious that the GPS/INS solution follows the reference solution closely, but suffers from large deviations, particularly in elevation. Also apparent, is that these deviations are not consistent throughout the course. For instance, the deviations seem to occur much more often in the first 12 km of the race and less frequently between 17 km and the 25 km marks.

The most erroneous trajectories were the result of GPS outages. That is to say, the worst departures from the reference navigation solution occurred when satellites were obscured from the antenna and the satellite signals were lost. The outage results in

(a)

(b)
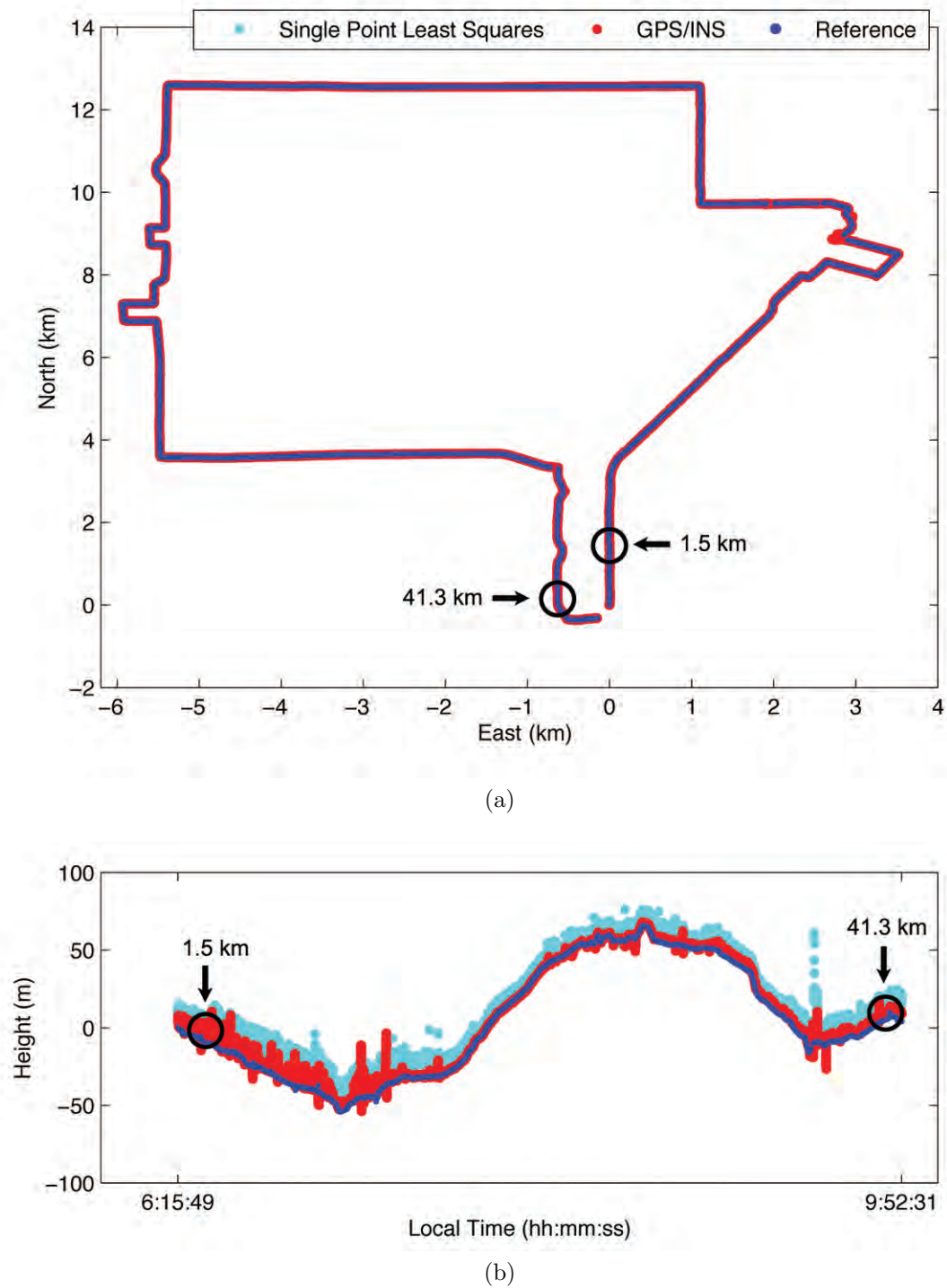
Figure 7.4: GPS/INS, reference and single point least-squares navigation solutions of a runner during the Las Vegas Marathon: (a) Horizontal trajectory. (b) Elevation trajectory.

no pseudorange measurements being used in the calculations, which causes the position solution to degrade rapidly (Godha et al 2006, Kwakkel et al 2008). In these cases, while the navigation solution is perturbed, the kinematics solutions are relatively unaltered (Kwakkel et al 2008).

At 11.2 km there was a 52 s GPS outage, when there were no GPS observations (the longest GPS outage of the race). This outage was caused by structures overhanging the race course. During this time, the filter depended exclusively on inertial measurements and Zero Velocity Updates (ZUPTs). As a result, the navigation solution accumulated the maximum position error of 55.15 m. During this interval, there were no single point, least-squares solutions. Thus, the GPS/INS approach shows a distinct advantage over the GPS only result: even though the GPS/INS navigation solution degraded, the runner still gathered navigation and kinematic information. As shown in Chapter 5, the absence of satellite observations has only marginal effects on the accuracy of the kinematic information.

Other deviations were likely the result of multipath. In the first 12 km of the race, the participants run along a road with many buildings and structures in close proximity to the race course. Reflections of the satellites' signals from these structures influence the perceived distances to the satellites and thus disrupt the navigation solution. The temporal and spatial variation as well as the magnitude of the disruption in the satellite solution are other indicators that the deviations are in fact the result of multipath as opposed to any other source.

The reference solution was less affected by multipath because it was calculated using phase measurements. Recall that the maximum error due to multipath in a phase-derived solution is proportional to the signal wavelength. In this case, since double-differenced measurements were used, the maximum error due to multipath is approximately 19 centimetres.

Table 7.2 characterizes the position errors from the GPS/INS and single point, least-squares navigation solutions as compared to the reference. The predicted errors reflect the mean of the filter-predicted standard deviations. The C3NavG^{2} ^{TM} software predicted errors accurately reflect 3D RMS values. However, this error is disproportionately distributed amongst the directional errors. While the vertical error was optimistically predicted by the C3NavG^{2} ^{TM} software, the errors in the north and east directions were pessimistic.

The GPS/INS filter was tuned to give similar predicted error values. By adjusting the gyroscope and accelerometer spectral densities (q_g and q_a) as well as the Gauss-Markov parameters that model the sensor biases and scale factors, the predicted errors can be adjusted to the true RMS error.

As expected, the navigation solution for the rearfoot GPS/INS is more accurate than the least-squares solution. This is particularly true in the vertical direction, (3.47 vs. 10.06 m RMS), and concordantly, the 3D RMS figure is also far better for the GPS/INS solution (3.90 vs. 10.26 m RMS). In fact, the GPS/INS solution RMS value is pessimistic since it includes the deviation from the reference solution after large GPS outages. The RMS value would be much lower without these intervals (see Figure 7.5).

Table 7.2: Position error of GPS/INS and single point, least-squares navigation solutions

	North	East	Vertical	2D	3D
Single Point, least-squares					
Predicted error* [m]	4.43	3.38	8.42	5.57	10.09
RMS [m]	1.69	1.04	10.06	1.99	10.26
Max [m]	11.37	7.15	34.96	13.43	37.45
Rearfoot Single Point, GPS/INS					
	North	East	Vertical	2D	3D
Predicted error* [m]	1.86	2.30	2.70	2.96	4.00
RMS [m]	1.51	0.93	3.47	1.77	3.90
Max [m]	19.17	9.26	50.86	21.29	55.15

* Mean of the solution-predicted standard deviations (1σ)

Two sections of the course are identified in Figure 7.4 and are enlarged in Figure 7.5:
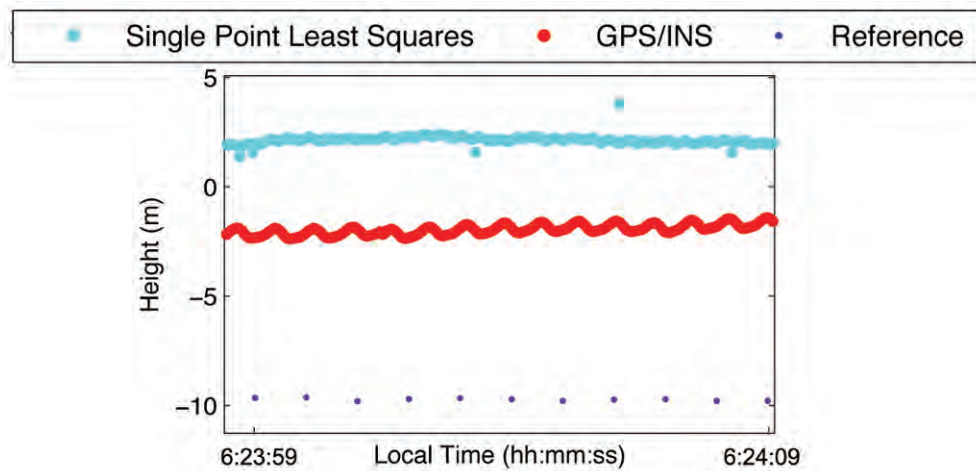
(a) 1.5 km
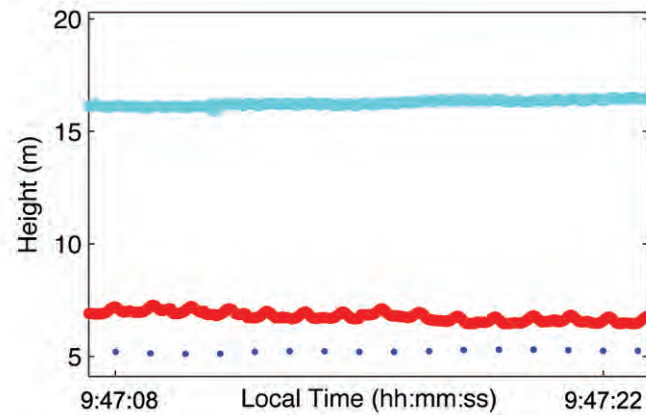
(b) 41.3 km

Figure 7.5: GPS/INS, reference and single point least-squares elevation trajectories at different sections of the Las Vegas Marathon: (a) 1.5 km. (b) 41.3 km.

namely, 1.5 km and 41.3 kilometres. From the enlarged sections of the course in Figure 7.5, the GPS/INS navigation solution clearly adheres to the reference moreso than the single point, least-squares positions.

The scalloping effect apparent in the GPS/INS solution, and to a lesser extent the single-point solution, reflect true organic movement. The GPS/INS solution reflects the vertical movement of the rearfoot, while the single point solution reflects the vertical displacement of the GPS antenna affixed to the head. The reference solution, having a lower output rate, does not have any scalloping.

The 1.5 and 41.3 km sections will represent portions at the beginning and end of the race, respectively. It is assumed that the runner was more fatigued during the latter portions of the race and so it is interesting to observe any gait changes between these two points along the race course. The 1.5 km section was chosen over early sections of the race because the crowd of participants in the first segment of the race caused the runners to run irregular patterns and perform no-typical running movements, such as shortened strides and side-steps. Similarly, the 41.3 km portion was chosen over later segments due to the presence of crowds at the end of the race that seem to have cause large multipath environment and lower satellite availability.

During the race there were periods where the GPS signal degraded either through multipath, geometry or other influences and adversely affected the navigation and kinematic solutions. It is difficult to detect these scenarios using the walk ratio since the step length is not sufficiently affected, however, inspecting the GDOP, or step elevation gain/loss in relation to the reference solution could be used to exclude these sections of data.

7.4   Inertial Kinematics

The kinematics of a runner over the course of a marathon have never been explored to the depth that is available here. While there have been studies that have investigated the effects of fatigue on the runner's stride, none have had a step-by-step glimpse at the movements of the runner as they pass through the race.

The performance of the step detection algorithm has been shown previously to reliably detect steps with approximately 5% error during running (see Section 5.3.3). The step lengths, step frequency and corresponding walk ratio are plotted in Figure 7.6. Again, as in Chapter 5, the walk ratio remains consistent for the entirety of the race despite there being a noticeable increase in step length and frequency during the first few kilometres
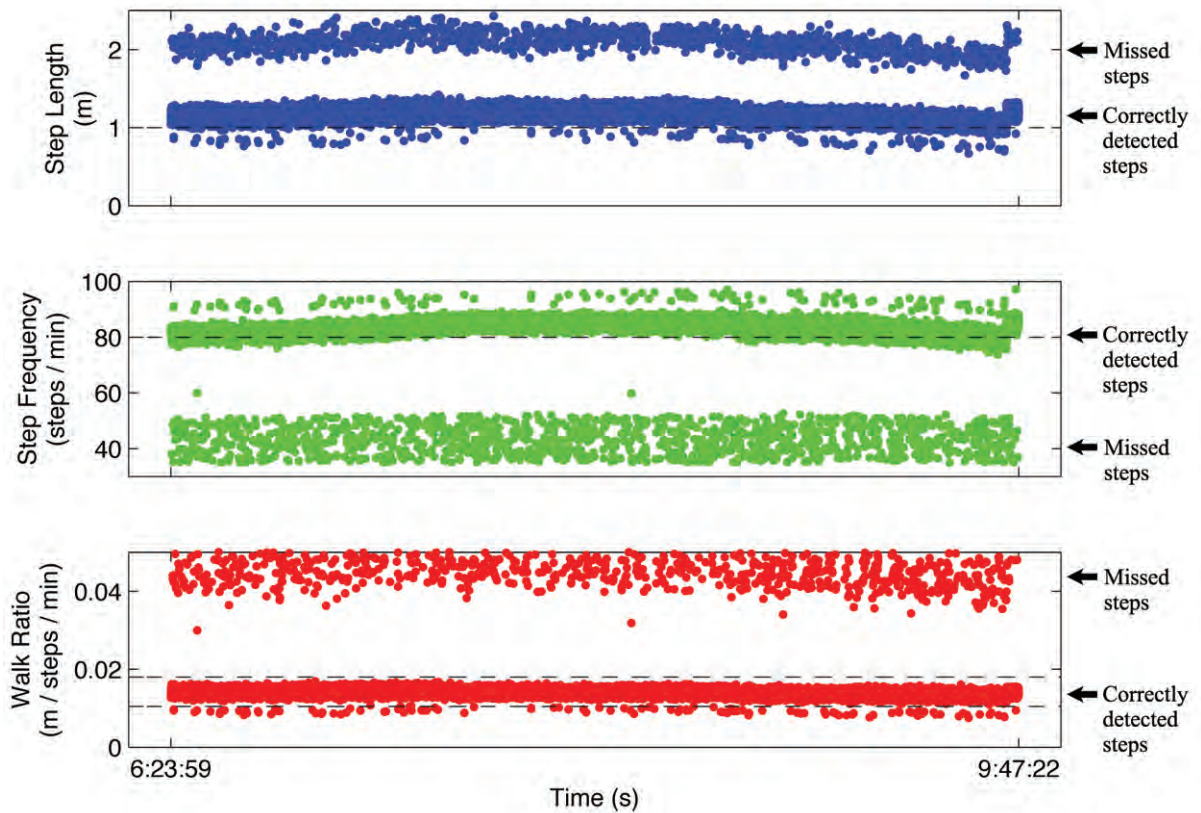
Figure 7.6: Step length, frequency and walk ratio throughout the 2007 Las Vegas Marathon

of the race, followed by a slow decline in step length and step frequency in the last third of the race. This pattern of step length and frequency correlates well with the velocity information shown in Figure 7.2.

The steps that result in a walk ratio between 0.010 and 0.018 $m/step/min$ shown in Figure 7.6 are used to perform the remainder of the kinematic analysis since they are considered properly detected steps. For instance, comparing steps during the first and last kilometres, a sampling of steps from each section of the race can be analyzed to give valuable information about the effects of fatigue on a runner's gait.

Figure 7.7 depicts the sagittal plane view of the position of the rearfoot IMU during a single step at the 1.5 km and the 41.3 km points during the race. This shows the

movement of the rearfoot in the early and late stages of the race. Presumably, the differences seen in the step positions are the result of fatigue. The step at 43.1 km clearly has a lower amplitude than the step earlier in the race.
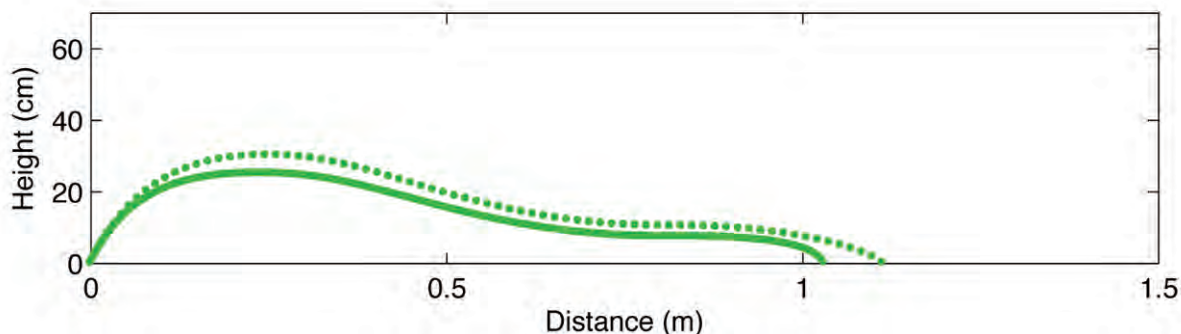
Figure 7.7: Sagittal plane view of steps at the 1.5 km ($\bullet$) and the 43.1 km (—) point of the 2007 Las Vegas Marathon

The decreased step length later in the race (see Figure 7.6) is confirmed in Figure 7.7. The mean step length over 30 steps in the first part of the race was 1.20 m (SD = 0.02), and it decreased to 1.02 m (SD = 0.04) by the later stages. While the steps depicted in Figure 7.7 are individual steps and were selected because they depict the mean step length and profile.

Figure 7.8 shows the ankle and knee flexion at the 1.5 km and the 41.3 km distances. The effects of having run the entire course of a marathon are visible in the flexion results. At the 41.3 km point, the runner's knee and ankle flexion are noticeably reduced. The knee and ankle flexion, after 41.3 km of running begins to resemble a walking gait with much less amplitude and peak flexion occurring much earlier in the the gait cycle.

Rotations in the coronal and transverse planes are much less interesting, and in light of the findings in Chapter 6 the reliability of these quantities is decreased, and have therefore been omitted here.

Overall, the kinematic information that is gathered here about the marathon runner is very interesting. There was an obvious effect of fatigue on the kinematics of the test subject presented here. While the results presented here are not exhaustive, the principle
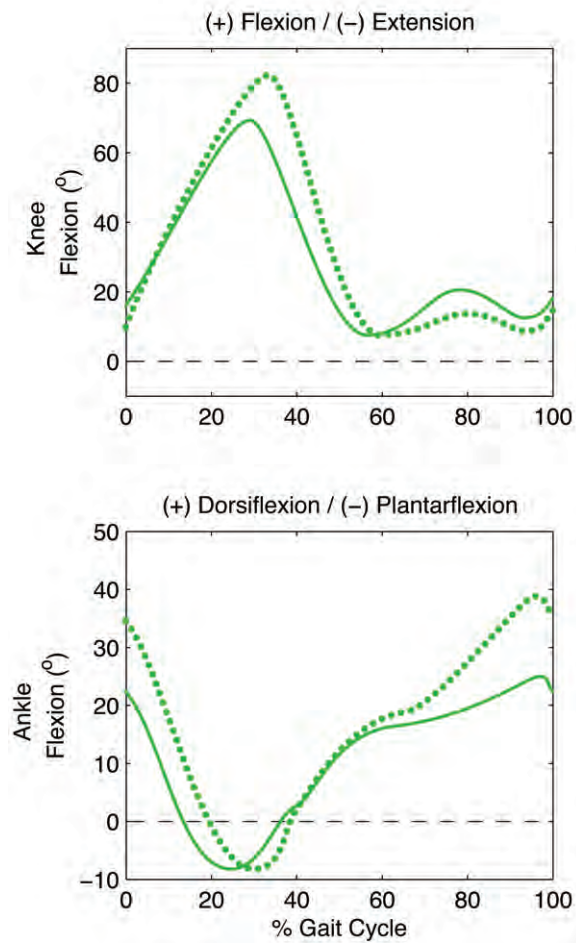
Figure 7.8: Knee and ankle flexion as measured at the 1.5 km ($\bullet$) and 41.3 km ($—$) distance of the 2007 Las Vegas Marathon

of using inertial kinematics alongside traditional GPS/INS navigation information has been shown here.

7.5   Results Summary

In this chapter, the combination of a number of different types of data were used to give a wide variety of information about the performance of runner during a marathon:

- *The position of the runner.* In the presence of a reference GPS receiver in close proximity to the race course, double-differenced GPS phase measurements gave an

excellent reference solution with which to determine the navigation error associated with the GPS/INS filter.

- *The speed of the runner.* The GPS Doppler measurements were used to calculate the velocity of the head-mounted antenna in order to determine the speed of the runner throughout the race course. By combining a variety of information such as position and velocity researchers and trainers as better able to assess their athlete's performance.

- *The steps of the runner.* Using a combination of step kinematics and *walk ratio* to validate steps, the position and translation of the foot could be traced through space. By detecting and eliminating a large portion of missed steps, the averaged step kinematics are more reliable. Visually observing the change in a runner's foot translation may lead to improved efficiency and targeted training exercises.

- *The runner's knee and ankle flexion.* Using a combination of the navigation solution and the kinematics solution, the runner's knee and ankle flexion was shown to change over the course of a marathon. Quantitatively showing these changes will help researchers and trainers assess the athletic performance of athletes and possibly lead to better race strategies.

This chapter represented the implementation of a variety of information that is available through GPS/INS. Using kinematic information in combination with positions, velocities and attitude adds a new dimension to the traditional kinematic analysis that has been done in the past. This was the first study to be conducted during the completion of a marathon. The breadth and accuracy of the measurements make this research very valuable for such scenarios. The added advantage of measuring individuals' movements while they perform various tasks will make this technology the favoured measurement modality for human motion analysis.

Chapter 8

Conclusions and Recommendations

The research presented in this thesis dealt with the assessment of a pedestrian GPS/INS system to perform kinematic measurements of walkers and runners. The measurement of the segments of the lower limb were targeted in order to exploit some newly developed advances in pedestrian navigation research. The application of ZUPTs to GPS/INS extended Kalman Filters has a two-fold benefit: first, the velocity errors are much more observable thus improving the velocity estimation of the system, and second, by virtue of the error state estimation, the attitude errors are also observable through ZUPTs. These are highly favourable improvements for kinematics applications.

The kinematics of a walking or running human are usually described within the context of a step. The human gait is highly repeatable and the step offers a discrete segmentation of a human's trajectory. Therefore, it was imperative to examine the robustness of recently established algorithms to detect and separate the steps that occur during walking and running. Once the steps could be reliably detected the rest of the kinematic work could begin.

The sensors used for this research were the Crista IMU from CloudCap Technologies and a NovAtel OEM VI L1-only receiver. The IMU's are considered MEMS-grade, which means that the error characteristics of the accelerometers and gyroscopes inside the unit are not well defined for any given usage and are highly susceptible to in-run changes. For this reason, the sensor errors were estimated as part of the GPS/INS filter and fed back to the IMU mechanization. This represents a vast improvement over typical inertial kinematics studies that have relied on scale-factor and bias figures determined though calibration, for the entirety of the experiment, thus neglecting the in-run changes in these

error characteristics.

In order to determine the system accuracy, the measurements attained from the proposed inertial methodology had to be validated against tried and tested optoelectric measurements; the current gold standard in motion analysis technology. To this end, the sensors were compared side-by-side and an analysis showed that the inertial system was highly accurate and quite robust under walking and running conditions.

Lastly, the inertial sensors were given a test of durability and longevity while the measurements of a runner's movements along the entirety of marathon were taken. In this case, a variety of GPS and inertial data were fused to give a variety of information about the runner along the race course. Double-differenced phase measurements, Doppler-derived velocity and the newly acquired kinematics measurements were combined to show the breadth of information that can be gathered about a human's performance in a marathon.

8.1   Conclusions

The following conclusions have been made from the research presented throughout this thesis:

1. Using the 3D acceleration signal, the gait cycle can be broken into four distinct phases: *Push-off* starting when the heel lifts off the ground until the to lift off the ground, *Swing* while the foot is suspended above the ground, *Heel Strike* from when the heel contacts the ground until the foot is stationary on the ground, and *Stance* which involves the foot being stationary on the ground. The 3D acceleration signal of a forefoot-mounted IMU is sufficient for distinguishing the four phases of the gait cycle. The gait phases in the forefoot acceleration profile are demarcated by abrupt changes in acceleration which occur in a reliable and repeatable fashion. Moreover, this signal can be used both in walking and running gaits.

2. The 3-sample variance analysis of the acceleration signal is an excellent method for stance phase detection during walking and running gaits. In this method, the variance of the acceleration signal is computed using three consecutive epochs. Below a threshold of 1 $(m/s^2)^2$, the stance phase is detected. Detection of the stance phase of the gait cycle allows for the application of *Zero Velocity Updates* (ZUPTs) during the stance phase of the gait cycle. The forefoot and rearfoot are the only segments of the lower limb to benefit from ZUPTs, since the other segments do not come to rest during a normal gait cycle.

3. Applying ZUPTs to the GPS/INS filter during the stance phase is an excellent method for controlling attitude errors. By controlling the velocity errors, the attitude errors are minimized by virtue of the transformation of the attitude into velocity in the error state matrix in the GPS/INS filter.

4. The 30-sample variance analysis of the forefoot acceleration signal is an excellent method for step detection during a walking gait. In this method, the magnitude of the 3D acceleration variance is computed using 30 consecutive epochs. When the variance surpasses a threshold of 1 $(m/s^2)^2$ after a period of no variance a step is detected. For a running gait, the 10-sample acceleration variance is used and the threshold is increased to 35 $(m/s^2)^2$ because of the higher dynamics inherent to the running gait.

5. Using the ratio of step length (SL) and step frequency (SF), also known as the *walk ratio* $(WR = SL/SF)$, provides a method to check if the step detection algorithm successfully detected a step. Since the walk ratio is consistent for an individual over a wide range of velocities, but not if a missed step occurs, it can be used to check if the walk ratio for a given step falls between two threshold values. These threshold values are unique to every person an must be determined before this method can be used.

6. A wide variety of kinematic comparisons are possible using the GPS/INS methodology because of the large, continuous data volume that is possible. Uphill vs. downhill steps, left leg vs. right leg, walking vs. running are only a couple of the comparisons made in this thesis. The opportunity to explore a wide variety of new scenarios given the proposed technology is limitless.

7. When compared to traditional optoelectric measurements, the positional accuracy of the proposed inertial kinematic measurements was of very high quality. During a walking gait, the mean 3D RMSE of the rearfoot IMU was 0.6 cm, and 1.2 cm while running. The maximum error computed was 1.0 and 1.6 cm, respectively.

8. The step length estimate using the integrated GPS/INS velocity is very accurate, measuring the walking step with 0.50% error and running step with 0.75% error. This translates in to step length misclosures of 4 mm for a walker and 9 mm for a runner.

9. When compared to traditional optoelectric measurements, the rotational accuracy of the proposed inertial kinematic measurements was very high quality. The RMSE for rotations in each of the three dimensional planes was less than 2 degrees.

10. Flexion angles were determined to be the most reliable since the percentage of error was less than 5 percent. Rotations in other angles were subject to high error percentages due to their low scale of measurement.

11. The navigation solution of the rearfoot GPS/INS navigation solution is very good compared to the single point, least squares navigation solution. The error in the trajectory given by the GPS/INS was 3.90 m (3D RMS) compared to 10.26 m RMSE for the single point, least squared solution.

12. Significant changes in a runners foot trajectory and joint flexion angles were noticeable between measurements taken in the first and last couple kilometres of the

Las Vegas Marathon. Owing partly to fatigue, the runner's feet remained lower during the step and the knee and ankle flexion was markedly reduced after 43.1 km of running.

13. The wide variety of information that is available given satellite and inertial measurements during a marathon is plentiful and interesting. Combining navigation and kinematic data offers a wide swath of analysis possibilities to the researcher or recreational runner.

8.2   Recommendations

In light of the research presented here and in the course of analyzing the wide variety of information that was available, the following recommendations for future work in this area can be made. The following is a list of such recommendations:

1. The challenge of determining the reliability of a given step was a constant challenge during this research. The walk ratio provided a robust and proven method for missed-step detection which led to the exclusion of a vast majority of aberrant steps. However, methods for detecting scenarios which cause gross deviations within a step (i.e. multipath) would help immensely.

2. While conducting the experiment for the validation of the inertial measurements (Chapter 6) it was apparent that the joint rotation angles typically calculated using optoelectrical measurements revolve about the joint axis which are determined using a defined calibration procedure to establish the joint coordinate frame. A method for establishing this frame using inertial sensors would be extremely beneficial for the adoption of this technology for human motion analysis.

3. While the measurements shown here describe the movements of the walkers and runners, it is still not possible to reconstruct the movements because of the lack

of any protocols for inverse kinematics using inertial sensors. The development of such protocols would be most helpful.

4. The GPS/INS extended Kalman Filter used in this work used exclusively single-point, code measurements. Therefore, the implementation of single difference and double-difference GPS/INS filter is warranted. Adaptive Kalman Filter technology would likely also be an interesting contribution.

5. The use of this system in a variety of scenarios is needed to verify the robustness of the algorithms. The marathon was one such scenario, however, similar tests could be conducted in a variety of applications.

6. Verifying the use of the inertial system for different individuals would help establish the robustness of the system. By using the system for more than one individual, the step detection and ZUPT algorithms could be generalized for use with people with different gait characteristics.

7. While the hardware developed for this research was unobtrusive, many modifications could be helpful. Specifically, wireless sensors could make the research less cumbersome. Also, integration of a wider variety of sensors such as heart rate sensors, magnetic compasses should be tested in future work.

Bibliography

ABI Research (2008) *Markets and Applications for GPS, Galileo and GLONASS*, Tech. rep., ABI Research

Aristotle (translated to English 2004) *De Motu Animalium (*On the Gait of Animals*)*, translated by A. S. Farquharson, University of Adelaide - eBooks@Adelaide, Adelaide

Bancroft, J., G. Lachapelle, M. E. Cannon & M. Petovello (2008) "Twin IMU-HSGPS Integration for Pedestrian Navigation," in *ION GNSS 2008*, Institute of Navigation, Savannah, Georgia

Bharatkumar, A., K. Daigle, M. Pandy, Q. Cai & J. Aggarwal (1994) "Lower limb kinematics of human walking with the medial axis transformation," *IEEE Workshop on Non-Rigid Motion*, pp. 70–76

Borelli, G. A. (1680) *De Motu Animalium (*On the Gait of Animals*)*, Unknown publisher

Breasted, J. H. (translated to English 1930) *The Edwin Smith Surgical Papyrus*, University of Chicago Press, Chicago

Breniere, Y. & G. Dietrich (1992) "Heel-off perturbation during gait initiation: biomechanical analysis using triaxial accelerometry and force plate," *J Biomech*, vol. 25, no. 2, pp. 121–127

Bussmann, J. B. J., H. J. van den Berg-Emons, S. M. Angulo, T. Stijnen & H. J. Stam (2004) "Sensitivity and reproducability of accelerometry and heart rate in physical strain assessment in prosthetic gait," *Eur J Appl Physiol*, vol. 91, pp. 71–78

Cannon, E. & G. Lachapelle (2005) *Satellite Navigation:* ENGO 465 Course Notes, University of Calgary, Department of Geomatics Engineering, Calgary, Canada

Carson, M. C., M. E. Harrington, N. Thompson, J. J. O'Connor & T. N. Theologis (2001) "Kinematic analysis of a multi-segment foot model for research and clinical applications: a repeatability analysis," *J Biomech*, vol. 34, no. 10, pp. 1299–307

Cloud Cap Technology Inc. (2007) *Crista interface/operation document*, Tech. rep., Cloud Cap Technology Inc.

da Vinci, L. (translated to English 2005) *Leonardo's Sketches*, Black Dog and Leventhal Publishing, New York

Danion, F., E. Varraine, M. Bonnard & J. Pailhous (2003) "Stride variability in human gait: the effet of stride frequency and stride length," *Gait and Posture*, vol. 18, pp. 69–77

Ducroquet, R., J. Ducroquet, P. Ducroquet & M. Saussez (1968) *La marche et les Boiteries (translated by William S. Hunter and Jep Hunter to Walking and limping - a study of normal and pathological walking)*, Lippincott, Philadelphia

El-Sheimy, N. (2007) *Inertial techniques and INS/DGPS Integration:* ENGO 699.63 Course Notes, University of Calgary, Department of Geomatics Engineering, Calgary, Canada

El Sheimy, N., H. Hou & X. Niu (2008) "Analysis and modelling of inertial sensors using Allan variance," *IEEE Trans Instr Meas*, vol. 57, no. 1, pp. 140–149

Farrell, J. & M. Barth (2001) *The global positioning system and inertial navigation*, McGraw Hills, New York

Fyfe, K. (1999) *Motion analysis system*, USPO - 6513381, United States

Gao, Y. (2006) *Data Analysis in Engineering:* ENGO 563 Course Notes, University of Calgary, Department of Geomatics Engineering, Calgary, Canada

Giansanti, D. (2006) "Does centripetal acceleration affect trunk flexion monitoring by means of accelerometers?" *Physiol Meas*, vol. 27, pp. 999–1008

Godha, S. (2006) *Performance Evaluation of Low Cost MEMS-Based IMU Integrated with GPS for Land Vehicle Navigation Application*, M.Sc. Thesis, University of Calgary

Godha, S., G. Lachapelle & C. Elizabeth (2006) "Integrated GPS/INS system for pedestrian navigation in a signal degraded environment," in *ION GNSS 2006*, Institute of Navigation, Fort Worth, Texas

Grewal, M. (2007) *Kalman Filtering:* ENGO 699.72 Course Notes, University of Calgary, Department of Geomatics Engineering, Calgary, Canada

Grewal, M., A. P. Andrews & L. R. Weill (2007) *Global Positioning Systems, Inertial Navigation, and Integration*, John Wiley and Sons, New Jersey

Grieve, D. W. & R. J. Gear (1966) "The relationships between length of stride, step frequency, time of swing and speed of walking for children and adults," *Ergonomics*, vol. 9, pp. 379–399

Habib, A. (2007) *Advanced Photogrammetry and Ranging Techniques:* ENGO 531 Course Notes, University of Calgary, Department of Geomatics Engineering, Calgary, Canada

Hippocrates (translated to English 2007) *On the Articulations*, translated by Francis Adams, University of Adelaide - eBooks@Adelaide, Adelaide

Holt, K. G., S. Jeng & R. Ratcliffe (1995) "Energetic cost and stability during human walking at the preferred stride frequency." *J Mot Behavior*, vol. 27, pp. 164–178

Hou, H. (2004) *Modelling inertial sensor errors using Allan variance*, Ph.D. thesis, University of Calgary

IEEE (2001) *Standard for inertial sensor terminology*, vol. IS 528, IEEE

Inman, V. T. (1966) "Human locomotion," *Canadian Medical Association Journal*, vol. 94, p. 1047

Inman, V. T., H. J. Ralston & F. Todd (1981) *Human Walking*, Williams and Wilkins, Baltimore/London

Jasiewicz, J. M., J. H. J. Allum, J. W. Middleton, A. Barriskill, P. Condie & P. B (2006) "Gait event detection using linear accelerometers or angular velocity tranducers in able-bodied and spinal cord injured individuals," *Gait Posture*, vol. 24, no. 4, pp. 502–509

Jekeli, C. (2001) *Inertial Navigation Systems with Geodetic Applications*, Walter de Gruyter, Berlin

Kaplan, E. D. & c. J. Hegarty (2006) *Understanding GPS - Principles and Applications*, Artech House, Boston, 2nd ed.

Kavanagh, J. J., S. Morrison, D. A. James & R. S. Barrett (2006) "Reliability of segmental accelerations measured using a wireless gait analysis system," *J Biomech*, vol. 39, pp. 2863–2872

Kay, S. M. (1998) *Fundamentals of Statistical Signal Processing: Detection Theory*, vol. 2, Prentice Hall, New York

Kepple, T. M., S. J. Stanhope, K. N. Lohmann & N. L. Roman (1990) "A video-based technique for measuring ankle-subtalar motion during stance," *J Biomed Eng*, vol. 12, no. 4, pp. 273–80

Kidder, S. M., J. Abuzzahab, F. S., G. F. Harris & J. E. Johnson (1996) "A system for the analysis of foot and ankle kinematics during gait," *IEEE Trans Rehabil Eng*, vol. 4, no. 1, pp. 25–32

Klette, R. & G. Tee (2007) *Understanding human motion: A historical review*, vol. 36, Springer

Kuusniemi, H. (2005) *User-level reliability and quality monitoring in satellite-based personal navigation*, Ph.D. thesis, Institute of Digital and Computer Systems, Tampere University of Technology, Finland

Kwakkel, S. (2007) *Foot and ankle kinematics during gait using foor mounted inertial sensors*, Research Project for BMEN500, University of Calgary

Kwakkel, S., S. Godha & G. Lachapelle (2007) "Foot and ankle kinematics during gait using foot mounted inertial system," in *ION NTM 2007*, Institute of Navigation, San Diego, California

Kwakkel, S., G. Lachapelle & M. E. Cannon (2008) "GNSS aided in situ human lower limb kinematics during running," in *ION GNSS 2008*, Institute of Navigation, Savannah, Georgia

Lachapelle, G. (2007) *Advanced GPS theory and applications:* ENGO 625 Course Notes, University of Calgary, Department of Geomatics Engineering, Calgary, Canada

Ladetto, Q. (2000) "On Foot Navigation: Continuous Step Calibration using Both Complimentary Recursive Prediction and Adaptive Kalman Filtering," in *ION GPS 2000*, Institute of Navigation, Salt Lake, Utah, pp. 1735–1740

Ladetto, Q., V. Gabaglio & B. Merminod (2001) "Two different approaches for augmented GPS pedestrian navigation," in *International Symposium on Location Based Services for Cellular Users*, Locellus

Lay, A. N., C. J. Hass & R. J. Gregor (2006) "The effects of sloped surfaces on locomotion: a kinematic and kinetic analysis," *J Biomech*, vol. 39, no. 9, pp. 1621–8

Leardini, A., M. G. Benedetti, F. Catani, L. Simoncini & S. Giannini (1999) "An anatomically based protocol for the description of foot segment kinematics during gait," *Clin Biomech (Bristol, Avon)*, vol. 14, no. 8, pp. 528–36

Lorimer, R. & E. Gakstatter (2008) *GNSS precise positioning marketing report*, Tech. rep., Position One Consulting Pty Ltd

Lyons, G. M., K. M. Culhane, D. Hilton, P. A. Grace & L. D (2005) "A description of an accelerometer-based mobility monitoring technique," *Med Eng Phys*, vol. 27, pp. 497–504

Mansfield, A. & G. M. Lyons (2003) "The use of accelerometry to detect heel contact events for use as a sensor in FES assisted walking," *Med Eng Phys*, vol. 25, pp. 879–885

Manson, A. J., P. Brown, J. D. O'sullivan, P. Asselman, D. Buckwell & A. J. Lees (2000) "An ambulatory dyskinesia monitor," *J Neurol Neurosurg Psychiatry*, vol. 68, pp. 196–201

Marey, J. (1878) *La Methode Graphique dans les Sciences Experimentales (*Graphical Methods in the Experimental Sciences*)*, translated by Karine Debbasch, Université René Descartes

Mayagoitia, R. E., A. V. Nene & P. H. Veltink (2002) "Accelerometer and rate gyroscope measurement of kinematics: an inexpensive alternative to optical motion analysis systems," *J Biomech*, vol. 35, no. 4, pp. 537–542

Menz, H. B., S. R. Lord & R. C. Fitzpatrick (2003) "Acceleration patterns of the head and pelvis when walking on level and irregular surfaces," *Gait Posture*, vol. 18, no. 1, pp. 35–46

Mezentsev, O. (2005) *Sensor Aiding of HSGPS Pedestrian Navigation*, Ph.D. thesis, University of Calgary

Misra, P. & P. Enge (2004) *Global positioning system: signals, measurements and performance*, Ganga-Jumuna Press, Lincoln, Massachusetts

Moe-Nilssen, R. (1998) "A new method for evaluating motor control in gait under real-life environmental conditions - Part I: The instrument," *Clin Biotech*, vol. 13, no. 4-5, pp. 320–327

Morris, S. J. & J. A. Paradiso (2002) "Shoe integrated sensor system for wireless gait analysis and real-time feedback," in *Second Joint EMBS/BMES*, IEEE, Houston, Texas, pp. 2468–2469

Murray, M. P., G. B. Spurr, S. B. Sepic, G. M. Gardner & L. A. Mollinger (1985) "Treadmill vs. floor walking: kinematics, electromyogram, and heart rate," *Journal of Applied Physiology*, vol. 59, pp. 87–91

Muybridge, E. (1955) *The Human Figure in Motion*, Dover Publications, New York

Muybridge, E. (1957) *Animals in Motion*, Dover Publications, New York

Nagasaki, H., H. Itoh, K. Hashizume, T. Furuna, H. Maruyama & T. Kinugasa (1996) "Walking patterns and finger rhythm of olderadults," *Percept Mot Skills*, vol. 82, pp. 435–447

Nassar, S. (2003) *Improving the inertial navigation system error model for INS and INS/DGPS applications*, Ph.D. thesis, University of Calgary

Nayak, R. A. (2000) *Reliable and continuous urban navigation using multiple GPS antennas and a low cost IMU*, M.Sc. Thesis, University of Calgary

Netter, F. H. (1997) "Bones of Foot," in A. F. Dalley, ed., *Atlas of Human Anatomy*, Icon Learning Systems, New Jersey

Nigg, B. M., R. W. de Boer & V. Fisher (1995) "A kinematic comparison of overground and treadmill running," *Medicine & Science in Sports & Exercise*, vol. 27, pp. 98–105

Park, M. & Y. Gao (2002) "Error analysis of low-cost MEMS-based accelerometers for land vehicle navigation applications," in *ION GPS*, Institute of Navigation, Portland, Oregon

Perrin, O., P. Terrier, Q. Ladetto, B. Merminod & Y. Schutz (2000) "Improvement of walking speed prediction by accelerometry and altimetry, validated by satellite positioning," *Med Biol Eng Comput*, vol. 38, pp. 164–168

Petovello, M. (2003) *Real-time integration of a tactical-grade IMU and GPS for high-accuracy positioning and navigation*, Ph.D. thesis, University of Calgary

Petrofsky, J. S., S. Lee, M. Macnider & E. Navarro (2005) "Automatic endothelial function and the analysis of gait in patients with type 1 and type 2 diabetes," *Acta Diabetol*, vol. 42, pp. 7–15

Pfau, T., T. Witte & A. Wilson (2005) "A method for deriving displacement data during cyclical movement using an inertial sensor," *Journal of Experimental Biology*, vol. 208, pp. 2503–2514

Prill, T. & J. Fahrenberg (2006) "Simultaneous assessment of posture and limb movements (e.g. periodic leg movements) with calibrated multiple accelerometry," *Physiol Meas*, vol. 27, pp. N47–53

Reinschmidt, C., A. J. van den Bogert, B. M. Nigg, A. Lundberg & N. Murphy (1997) "Effect of skin movement on the analysis of skeletal knee joint motion during running," *J Biomechanics*, vol. 30, no. 7, pp. 729–732

SAI Timing (2008) "SAI Timing and Location - http://www.sai-timing.com/,"

Saunders, J., V. Inman & H. Eberhart (1953) "The major determinants in normal and pathological gait," *Journal of Bone and Joint Surgery*, vol. 35A, pp. 543–558

Savage, P. G. (2000) *Strapdown Analytics*, vol. 1, Strapdown Associates Inc, New York

Schenk, T. (2000) *Digital Photogrammetry*, Terra Science, Laurelville, Ohio

Schutz, Y., S. Weinsier, P. Terrier & D. Durrer (2002) "A new accelerometric method to assess the daily walking practice," *Int J Obes*, vol. 26, pp. 111–118

Scott, S. H. & D. A. Winter (1991) "Talocrural and talocalcaneal joint kinematics and kinetics during the stance phase of walking," *J Biomech*, vol. 24, no. 8, pp. 743–52

Sekine, M., T. Tamura, T. Togawa & Y. Fukui (2000) "Classification of waist acceleration signals in a continuous walking record," *Med Eng Phys*, vol. 22, pp. 285–291

Selles, R. W., M. A. G. Formanoy, J. B. J. Bussmann, P. J. Janssens & H. J. Stam (2005) "Automated estimation of initial and terminal contact timing using accelerometers; development and validation in transtibial amputees and controls," *IEEE Trans Neural Syst Rehabil Eng*, vol. 13, no. 1, pp. 81–88

Shin, E. (2005) *Estimation techniques for low-cost inertial navigation*, Ph.D. thesis, University of Calgary

Siegel, K. L., T. M. Kepple, P. G. O'Connell, L. H. Gerber & S. J. Stanhope (1995) "A technique to evaluate foot function during the stance phase of gait," *Foot Ankle Int*, vol. 16, no. 12, pp. 764–70

Simcox, S., S. Parker, G. M. Davisa, R. W. Smith & J. W. Middleton (2005) "Performance of the orientation sensors for use with a functional electrical stimulation mobility system," *J Biomech*, vol. 38, pp. 1185–1190

Skaloud, J. (1999) *Optimizing georeferencing of airborne survey systems by INS/GPS*, Ph.D. thesis, University of Calgary

Söderkvist, I. & P.-A. Wedin (1993) "Determining the movements of the skeleton using well-configured markers," *J Biomechanics*, vol. 26, no. 12, pp. 1473–1477

Stirling, R., K. Fyfe & G. Lachapelle (2005) "Evaluation of a New Method of Heading Estimation for Pedestrian Dead Reckoning Using Shoe Mounted Sensors," *Journal of Navigation*, vol. 58, no. 1, pp. 31–45

Tanaka, S., K. Motoi, M. Nogawa & K. Yamakoshi (2004) "A new portable device for ambulatory monitoring of human posture and walking velocity using miniature accelerometers and gyroscopes," in *26th Annual International Conference of the IEEE EMBS*

Terrier, P., Q. Ladetto, B. Merminod & Y. Schutz (2000) "High-precision satellite positioning system as a new tool to study the biomechanics of human locomotion," *J Biomech*, vol. 33, no. 12, pp. 1717–22

Teunissen, P. J. G. & M. A. Salzmann (1989) "A recursive slippage test for use in state-space filtering," *Manuscripta Geodaetica*, vol. 14, pp. 383–390

Trendelenberg, F. (1895) "On the gait of people with congenital dislocation of the hip (Translated by Jean Lieberman and Larry Lamoreux)," *Deutsche Medicinische Wochenschrift*, vol. 22, no. 2

Udupa, J. K., B. E. Hirsch, H. J. Hillstrom, G. R. Bauer & J. B. Kneeland (1998) "Analysis of in vivo 3-D internal kinematics of the joints of the foot," *IEEE Trans Biomed Eng*, vol. 45, no. 11, pp. 1387–96

USATF, United States of America Track & Field. (2008) *Course Measurement and Certification Prodecure*, http://www.usatf.org/events/courses/certification/manual/

USCG, United States Coast Guard Navigation Center. (2008) "GPS constellation status for 13 May, 2008 - http://www.navcen.uscg.gov/navinfo/Gps/ActiveNanu.aspx,"

Weber, E., W. Weber & E. Weber (1836) *Die Mechanik Der Menschlichen Gerverzeuge* (The Mechanism of Human Walking), Unknown publisher

Willemsen, A. T. M. & F. Bloemhof (1990) "Automatic stnce-swing phase detection from accelerometer data for personal nerve stimulation," *IEEE Trans Biomed Eng*, vol. 37, no. 12

Willemsen, A. T. M., J. A. van Alste & H. B. K. Boom (1990) "real-time gait assessment utilizing a new way of accelerometry," *J Biotech*, vol. 23, no. 8, pp. 859–863

Zijlstra, W. (2004) "Assessment of spatio-temporal parameters during unconstrained walking," *Eur J Appl Physiol*, vol. 92, no. 1-2, pp. 39–44